

This is to certify that the
dissertation entitled

Growth of single crystal diamond

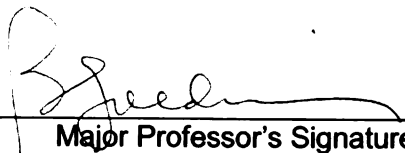
presented by

Murari Regmi

LIBRARY
Michigan State
University

has been accepted towards fulfillment
of the requirements for the

Doctoral degree in Physics and Astronomy



Major Professor's Signature

23 August 2007

Date

PLACE IN RETURN BOX to remove this checkout from your record.
TO AVOID FINES return on or before date due.
MAY BE RECALLED with earlier due date if requested.

DATE DUE	DATE DUE	DATE DUE

GROWTH OF SINGLE CRYSTAL DIAMOND

By

Murari Regmi

A DISSERTATION

Submitted to
Michigan State University
in partial fulfillment of the requirements
for the degree of

DOCTOR OF PHILOSOPHY

Department of Physics and Astronomy

2007

ABSTRACT

GROWTH OF SINGLE CRYSTAL DIAMOND

By

Murari Regmi

The subject of the research presented in this dissertation is the growth of single crystal diamond by microwave plasma chemical vapor deposition (CVD). Both heteroepitaxial and homoepitaxial growth methods have been examined, with emphasis on producing large diamond crystals of high structural and chemical perfection.

By heteroepitaxy, epitaxial growth on a foreign substrate, diamond was grown on (001) Ir thin-film epitaxial buffer layers deposited on (001) strontium titanate (SrTiO_3) by DC magnetron sputtering. To nucleate diamond on Ir, the Ir surface was bombarded with low energy ions extracted from the hydrocarbon plasma, a process known as DC biasing or bias-enhanced nucleation. Since this critical process is poorly understood, attention was paid to the spatial and temporal evolution of the Ir surface during the bias treatment. It was discovered that the biased Ir surface is etched on a surprisingly short time scale during which highly correlated nanopillars, 3-4 nm in height with mean separation 15 nm, emerge. The etching process is spatially non-uniform, propagating from substrate center to substrate edge in minutes. Diamond grew on Ir without an intervening phase. Lattice images revealed that interfacial strain from the 7% Ir-diamond lattice mismatch is largely relieved by misfit dislocations within 1 nm of the interface. It is suggested that the high nucleation density obtained with specific bias conditions is associated with the roughened Ir surface.

To grow heteroepitaxial diamond as thick films, a two-step growth method was explored. This process involved the transfer of a thin heteroepitaxial diamond film, still attached to a substrate, to a second reactor where high growth rate conditions were possible. Characterization of films grown by this approach showed that the resulting diamond had much lower levels of internal strain, suggesting that the process could be used to grow diamond crystals of structural quality similar to natural diamond.

In homoepitaxy, epitaxial growth on a substrate of the same material, diamond was deposited by CVD directly onto high-pressure, high-temperature Type Ib diamond substrates. Methods for removing substrate surface damage, as well as other imperfections, were devised by use of plasma etching. The characteristics and statistics of pits formed during etching were studied. Diamond growth methods were developed with the aim of minimizing the formation of various structural and chemical defects. To accomplish this, several growth parameters were varied, including substrate temperature, feed gas concentration, growth rate, substrate surface, microwave power, and reactor geometry. Regions of parameter space were found in which the diamond (001) surface remained smooth during growth, and complete suppression of instabilities that create hillocks or non-epitaxial crystallites was demonstrated. A great deal of information was obtained by interrupting growth, removing the crystal from the reactor for optical inspection, and then resuming the process with no apparent negative effects. Diamond crystals were grown on $3 \times 3 \text{ mm}^2$ substrates with thicknesses greater than 0.5 mm. The chemical purity of the crystals was such that it was impossible to observe signatures of substitutional nitrogen at the ppm level.

In loving memory of my grandmother Krishna Kumari Regmi

ACKNOWLEDGEMENTS

I would like to thank my advisor, Dr. Brage Golding, for the opportunity to work on this project, and his boundless optimism that I could complete it. He taught me how to think as a researcher. He was always there for suggestions and help when I had problems of any kind.

I acknowledge Dr. R. J. Anderson (Sandia) for the exciton luminescence characterization and Dr. D. L. Medlin (Sandia) for the HRTEM images.

I would also like to thank Dr. Mark Dykman, Dr. Stephen Zepf, Dr. Kirsten Tollefson and Dr. Chong-Yu Ruan for serving on my guidance committee.

I would also like to thank Drs. Baokang Bi, Reza Loloee and Katherine Severin for their help and technical suggestions.

Tom Palazzolo, Jim Muns, Tom Hudson, and the rest of the Physics and Astronomy machine shop staff patiently answered my questions and made the parts I needed in a timely manner. Their excellent work helped me to finish the project on time.

Ann Kirchmeier, Darla Conley Shawna Prater and Debbie Simmons helped with orders and administrative items I wanted in a timely manner.

I would like to thank my senior Connie Bednarski-Meinke for her previous work on the heteroepitaxial diamond growth. Her occasional visits and the suggestions gave me the boost I needed. I also like to thank Ryan Kruse and Mahdokht Behravan for their suggestions and encouragement.

Finally, I would like to thank my grandfather, my parents, my wife and kids, my brother, my sister-in-law and other relatives for their support and encouragement.

TABLE OF CONTENTS

LIST OF TABLES	IX
LIST OF FIGURES	X
1 CHAPTER 1 INTRODUCTION.....	1
2 CHAPTER 2 STRUCTURE AND PROPERTIES OF DIAMOND	4
2.1 CRYSTAL STRUCTURE	4
2.2 BAND STRUCTURE.....	5
2.3 HISTORICAL CLASSIFICATION OF DIAMOND TYPES: IMPURITIES.....	6
2.4 PHYSICAL PROPERTIES.....	7
2.4.1 Electronic Properties.....	7
2.4.2 Optical properties.....	10
2.4.3 Optical properties of impurity-related defects	12
3 CHAPTER 3 GROWTH OF DIAMOND BY CVD	15
3.1.1 Epitaxy and epitaxial growth	15
3.1.2 Nucleation	16
3.1.3 Crystal growth modes	17
3.1.4 Substrate criteria for diamond heteroepitaxy	18
3.1.5 Epitaxial diamond growth on different substrates	19
3.1.6 Heteroepitaxial diamond growth on iridium.....	21
3.2 BIAS-ENHANCED NUCLEATION (BEN)	23
3.2.1 BEN mechanisms.....	23
3.2.2 Biasing experiment with Ir.....	26
3.3 HOMOEPITAXY	28
3.3.1 Background	28
3.3.2 Growth of defects.....	31
3.3.3 Effect of growth parameters.....	34
3.3.4 Growth anisotropy: the alpha parameter.....	39
4 CHAPTER 4 MATERIALS CHARACTERIZATION METHODS	41
4.1 OPTICAL MICROSCOPY	41
4.2 ATOMIC FORCE MICROSCOPY	43

4.3	SCANNING ELECTRON MICROSCOPY	44
4.4	TRANSMISSION ELECTRON MICROSCOPY	46
4.5	RAMAN SCATTERING AND PHOTOLUMINESCENCE	48
4.6	X-RAY DIFFRACTION	50
4.6.1	ω - 2θ or θ - 2θ scan	54
4.6.2	θ or ω scan or rocking curve	54
5	CHAPTER 5 HETEROEPITAXIAL GROWTH OF DIAMOND	55
5.1	SUBSTRATES	55
5.1.1	Iridium.....	55
5.1.2	Strontium titanate (SrTiO ₃).....	56
5.1.3	Sapphire (Al ₂ O ₃).....	56
5.1.4	SrTiO ₃ preparation	57
5.2	DC MAGNETRON SPUTTERING OF IRIDIUM	58
5.2.1	Sputtering system.....	59
5.2.2	Sputtering procedure.....	62
5.2.3	Ir growth on SrTiO ₃	64
5.3	CVD REACTOR PROCESS	69
5.3.1	Substrate stage and bias set up.....	70
5.3.2	Substrate holder	72
5.4	DIAMOND NUCLEATION	73
5.4.1	The bias process.....	73
5.4.2	Discussion	91
5.4.3	Summary	95
5.5	DIAMOND THIN FILM GROWTH	95
5.6	DIAMOND THICK FILM GROWTH	99
5.6.1	Raman spectroscopy	103
5.6.2	Free exciton luminescence.....	105
5.7	SUMMARY.....	107
6	CHAPTER 6 HOMOEPITAXIAL GROWTH OF DIAMOND	108
6.1	EXPERIMENTAL METHODS.....	109
6.1.1	AsTeX diamond CVD reactor	109
6.1.2	Operational procedures	116
6.2	GROWTH PROCESS	117
6.2.1	Diamond substrate preparation	118
6.2.2	CVD homoepitaxial diamond growth process.....	127
6.2.3	Long-term growth procedures.....	133
6.2.4	Nitrogen in CVD diamond.....	138
6.3	HOMOEPITAXIAL DIAMOND CHARACTERIZATION.....	147
6.3.1	High resolution x-ray diffraction	147
6.3.2	Raman spectroscopy	149

6.3.3	Fourier transform infrared spectrophotometry (FTIR)	151
6.4	DISCUSSION	153
7	CHAPTER 7 DISCUSSION AND CONCLUSIONS	155
7.1	SUGGESTIONS FOR FUTURE WORK	156
8	APPENDIX A	159
8.1	SAMPLE INFORMATION.....	159
8.1.1	Heteroepitaxial sample information.....	159
8.1.2	Homoepitaxial sample information.....	159
9	APPENDIX B	160
9.1	PYROMETER CALIBRATION.....	160
10	APPENDIX C	165
10.1	IR GROWTH ON Al_2O_3	165
10.1.1	Al_2O_3 preparation.....	165
10.1.2	Ir growth on Al_2O_3	166
11	REFERENCES.....	170

LIST OF TABLES

TABLE 2.1. DIAMOND CLASSIFICATION ACCORDING TO THE AMOUNT OF IMPURITY	6
TABLE 2.2 ROOM TEMPERATURE CARRIER MOBILITIES OF DIAMOND	9
TABLE 3.1 TWO GROWTH REGIMES IN MICROWAVE PLASMA CVD DIAMOND GROWTH.....	31
TABLE 5.1 GROWTH CONDITIONS FOR 3.5 MM DIA DIAMOND FILM.....	96
TABLE 5.2 GROWTH CONDITIONS FOR 5 X 5 MM ² DIAMOND FILM.....	97
TABLE 5.3 GROWTH CONDITIONS FOR 8 MM DIA DIAMOND ON 10 X 10 MM ² Ir/STO	98
TABLE 5.4 HIGH GROWTH CONDITIONS OF HETEROEPITAXIAL DIAMOND FILM.....	100
TABLE 6.1 GROWTH CONDITIONS FOR 4 SAMPLES GROWN AT DIFFERENT TEMPERATURE	127
TABLE 6.2 GROWTH CONDITIONS FOR DIAMOND GROWN AT DIFFERENT R.	130
TABLE 6.3 GROWTH CONDITIONS FOR TWO DIAMOND SAMPLES.	130
TABLE 6.4 GROWTH CONDITIONS FOR SAMPLES A ₆ AND A ₇	132
TABLE 6.5 GROWTH CONDITIONS FOR A 515 μM THICK DIAMOND.....	135
TABLE 6.6 GROWTH CONDITIONS FOR SAMPLE A ₉	137
TABLE 6.7 PL INTENSITIES FROM (N-V) CENTERS IN CVD DIAMOND.	144

LIST OF FIGURES

FIGURE 2.1 CRYSTAL STRUCTURE OF DIAMOND.....	4
FIGURE 2.2 ELECTRONIC BAND STRUCTURE OF DIAMOND	5
FIGURE 2.3 ELECTRICAL CONDUCTIVITY VS. RECIPROCAL TEMPERATURE FOR DIAMOND	8
FIGURE 2.4 TEMPERATURE DEPENDENCE OF ELECTRON MOBILITY IN CVD DIAMOND	9
FIGURE 2.5 ABSORPTION SPECTRUM OF A HIGHLY PURE TYPE IIA NATURAL DIAMOND	11
FIGURE 2.6 INFRARED ABSORPTION SPECTRUM OF A HIGHLY PURE NATURAL DIAMOND ...	12
FIGURE 3.1 CRYSTAL GROWTH MODES AS A FUNCTION OF SURFACE COVERAGE.....	18
FIGURE 3.2 MAP OF SURFACE MORPHOLOGIES AS A FUNCTION OF MISCUT ANGLE	30
FIGURE 3.3 PYRAMIDAL HILLOCKS WITH NON-EPITAXIAL CRYSTALLITES.....	32
FIGURE 3.4 MECHANISM OF TWO DIMENSIONAL NUCLEATION ON A WIDE TERRACE.	32
FIGURE 3.5 SCHEMATIC VIEW OF STEP FLOW GROWTH.....	33
FIGURE 3.6 MACRO-STEP BUNCHING IN HOMOEPITAXIAL DIAMOND	34
FIGURE 3.7 DIAMOND GROWTH RATE AS A FUNCTION OF SUBSTRATE TEMPERATURE	35
FIGURE 3.8 GROWTH RATE AS A FUNCTION OF METHANE CONCENTRATION AT 850 °C	36
FIGURE 3.9 SHAPE OF DIAMOND CRYSTALS FOR DIFFERENT VALUES OF ALPHA..	40
FIGURE 4.1 SCHEMATIC OF A DIFFERENTIAL INTERFERENCE CONTRAST MICROSCOPE	41
FIGURE 4.2 THE OLYMPUS BX-60 DIC OPTICAL MICROSCOPE	42
FIGURE 4.3 SCHEMATIC OF ATOMIC FORCE MICROSCOPE	44
FIGURE 4.4 SCHEMATIC OF A SCANNING ELECTRON MICROSCOPE.....	45
FIGURE 4.5 SCHEMATIC OF A TRANSMISSION ELECTRON MICROSCOPE.....	47
FIGURE 4.6 SCHEMATIC OF A RAMAN SPECTROMETER	49

FIGURE 4.7 SCHEMATIC OF X-RAY DIFFRACTION FROM A CRYSTAL.....	50
FIGURE 4.8 SCHEMATIC SHOWING THE BRAGG'S LAW OF DIFFRACTION	51
FIGURE 4.9 EWALD SPHERE CONSTRUCTION	52
FIGURE 4.10 SCHEMATIC OF BRUKER AXS X-RAY DIFFRACTROMETER	53
FIGURE 5.1 AFM IMAGE SHOWING THE TOPOGRAPHY OF THE SrTiO_3 SUBSTRATE.....	58
FIGURE 5.2 SCHEMATIC OF THE THREE-GUN APX SPUTTERING SYSTEM	60
FIGURE 5.3 SCHEMATIC OF THE SAMPLE STAGE OF SPUTTERING SYSTEM.....	62
FIGURE 5.4 TOPOGRAPHY OF 500 NM THICK IR FILMS ON SrTiO_3	66
FIGURE 5.5 LINEWIDTH AND MEAN ROUGHNESS OF IR VS. TEMPERATURE	66
FIGURE 5.6 X-RAY SCAN OF A 600 NM THICK IR FILM.....	68
FIGURE 5.7 X-RAY (111) POLE FIGURE OF IR AND SrTiO_3	69
FIGURE 5.8.GENERAL SCHEMATIC OF THE MICROWAVE PLASMA CVD REACTOR.	70
FIGURE 5.9 SCHEMATIC OF THE SAMPLE STAGE AND BIAS SET UP FOR DIAMOND GROWTH. 71	
FIGURE 5.10 ELECTRICAL CIRCUIT USED FOR BIASING.	72
FIGURE 5.11 SCHEMATIC OF SAMPLE POST AND CAP WITH SAMPLE STAGE.....	73
FIGURE 5.12 TIME PLOT OF THE PROCESS SEQUENCE	74
FIGURE 5.13 AFM IMAGES OF THE IR SURFACE BIASED FOR DIFFERENT DURATIONS.	76
FIGURE 5.14 SEM IMAGES OF THE IR SURFACE BIASED FOR DIFFERENT DURATIONS.....	78
FIGURE 5.15 HRTEM IMAGES OF THE IR SURFACE AFTER BIASING.....	81
FIGURE 5.16 SEM IMAGES OF SAMPLES WITH DIFFERENT T_B FOLLOWED BY $T_G = 20$ MIN....	82
FIGURE 5.17 PLOT SHOWING % AREA COVERED BY EPITAXIAL DIAMOND.	84
FIGURE 5.18 SEM IMAGES OF 60 MIN BIASED SAMPLES FOLLOWED BY SHORT GROWTH....	86
FIGURE 5.19 HRTEM IMAGE OF IR SURFACE FOR A $T_B = 60$ MIN, $T_G = 0$ MIN SAMPLE.....	87

FIGURE 5.20 CROSS SECTION HRTEM IMAGES FOR A $T_B = 60$ MIN, $T_G = 90$ S SAMPLE	89
FIGURE 5.21 HRTEM IMAGE FOR A $T_B = 60$ MIN $T_G = 150$ S SAMPLE.....	90
FIGURE 5.22 HRTEM IMAGE OF A $T_B = 10$ MIN AND $T_G = 20$ MIN SAMPLE.	91
FIGURE 5.23 DIC MICROGRAPH AND SEM IMAGE OF 3.5 MM DIA DIAMOND FILM	96
FIGURE 5.24 DIC MICROGRAPH AND SEM IMAGE OF A 5×5 MM ² DIAMOND FILM.	98
FIGURE 5.25 DIC MICROGRAPH AND SEM IMAGE OF A 8 MM DIA DIAMOND FILM	99
FIGURE 5.26 HETEROEPITAXIAL DIAMOND FILM BEFORE AND AFTER PLASMA ETCHING... ..	100
FIGURE 5.27 DIC OPTICAL MICROGRAPH OF A DIAMOND FILM AFTER 3 H GROWTH	101
FIGURE 5.28 DIC MICROGRAPH OF A 65 μ M THICK HETEROEPITAXIAL DIAMOND ON IR... ..	101
FIGURE 5.29 RAMAN SPECTRUM OF HETEROEPITAXIAL DIAMOND	104
FIGURE 5.30 RAMAN SPECTRA OF TWO HETEROEPITAXIAL DIAMOND CRYSTALS.	105
FIGURE 5.31 COMPARISON OF FREE EXCITON LUMINESCENCE OF DIAMOND.	106
FIGURE 6.1 SCHEMATIC OF CVD REACTOR FOR HOMOEPITAXIAL DIAMOND GROWTH.....	111
FIGURE 6.2 SCHEMATIC OF COOLING STAGE AND SUBSTRATE HOLDER	114
FIGURE 6.3 RGA SPECTRUM TAKEN DURING DIAMOND GROWTH AT 150 TORR.	116
FIGURE 6.4 OPTICAL PHOTOGRAPH OF A HPHT TYPE Ib DIAMOND SUBSTRATE.	118
FIGURE 6.5 DIC MICROGRAPH OF A PLASMA-ETCHED DIAMOND SUBSTRATE.	119
FIGURE 6.6 POLISHING SCRATCHES ON THE SURFACE OF DIAMOND SUBSTRATE.....	120
FIGURE 6.7 DIAMOND SURFACE AFTER PLASMA ETCHING AT R = 2% P = 150 TORR	122
FIGURE 6.8 DIAMOND SURFACE AFTER PLASMA ETCHING AT R = 2 % P = 100 TORR	123
FIGURE 6.9 DIC IMAGES OF DIAMOND AFTER PLASMA ETCHING FOR DIFFERENT TIME.....	124
FIGURE 6.10 STATISTICS OF ETCH PITS.....	125
FIGURE 6.11 DIAMOND SURFACE AFTER PLASMA ETCHING SHOWING INCLUSIONS.....	126

FIGURE 6.12 DIC MICROGRAPHS OF DIAMOND SURFACES GROWN AT DIFFERENT T_G	128
FIGURE 6.13 EFFECT OF TEMPERATURE ON GROWTH RATE	129
FIGURE 6.14 DIC IMAGES OF A DIAMOND SAMPLE GROWTH AT DIFFERENT R	130
FIGURE 6.15 DIC MICROGRAPHS OF DIAMOND SURFACES GROWN AT DIFFERENT R	131
FIGURE 6.16 GROWTH RATE VS. METHANE-HYDROGEN RATIO R.	131
FIGURE 6.17 SEM IMAGE OF A 290 μm THICK DIAMOND CRYSTAL ON SUBSTRATE	132
FIGURE 6.18 OPTICAL PHOTOGRAPH OF A 290 μm THICK FILM ON ITS SUBSTRATE	133
FIGURE 6.19 DIC MICROGRAPHS OF CRYSTAL A_8 AFTER DIFFERENT GROWTH PERIODS ...	134
FIGURE 6.20 HEIGHT PROFILE OF DIAMOND CRYSTAL A_8 ALONG ITS SURFACE DIAGONAL	135
FIGURE 6.21 OPTICAL PHOTOGRAPHS OF A 515 μm THICK DIAMOND CRYSTAL.	136
FIGURE 6.22 OPTICAL PHOTOGRAPH OF A 550 μm THICK CRYSTAL	137
FIGURE 6.23 RAMAN SPECTRA OF TYPE IB DIAMOND SUBSTRATES	139
FIGURE 6.24 FTIR SPECTRA OF DIAMOND (A) NATURAL TYPE IIA (B) TYPE IB.	140
FIGURE 6.25 X-RAY (004) ROCKING CURVE LINEWIDTH OF A DIAMOND SUBSTRATE	141
FIGURE 6.26 RAMAN SPECTRUM TAKEN FROM CVD HOMOEPITAXIAL DIAMOND.....	142
FIGURE 6.27 RAMAN SPECTRA OF CVD DIAMOND CRYSTALS	143
FIGURE 6.28 GRAPH SHOWING THREE DIFFERENT REGIONS IN T_G -R SPACE.....	144
FIGURE 6.29 GROWTH RATE VS. NITROGEN CONCENTRATION (RELATIVE TO H_2).	145
FIGURE 6.30 ROOM TEMPERATURE RAMAN SPECTRA FOR DIAMOND GROWN WITH N_2	146
FIGURE 6.31.(N-V) PL PEAK HEIGHTS, AFTER BACKGROUND SUBTRACTION	147
FIGURE 6.32 X-RAY ROCKING CURVE FOR THE (004) REFLECTION OF DIAMOND.....	148
FIGURE 6.33 X-RAY (111) POLE FIGURE FROM HOMOEPITAXIAL CVD DIAMOND.....	149
FIGURE 6.34 RAMAN SPECTRUM OF CVD HOMOEPITAXIAL DIAMOND SAMPLE.....	150

FIGURE 6.35 RAMAN SPECTRA SHOWING RAMAN LINEWIDTH FOR DIAMOND.....	151
FIGURE 6.36 FTIR SPECTRA OF DIAMOND CRYSTALS.....	152
FIGURE 6.37 MAGNIFIED FTIR ABSORPTION SPECTRA OF DIAMOND CRYSTALS.....	153
FIGURE 9.1 PYROMETER TEMPERATURE VS R TYPE TC TEMPERATURE	161
FIGURE 9.2 PYROMETER AND TC TEMPERATURE WITH 2 KINDS OF QUARTZ PLATE.....	162
FIGURE 9.3 PYROMETER TEMPERATURE WITH AND WITHOUT QUARTZ PLATE.....	163
FIGURE 9.4 TWO-COLOR VS. SINGLE COLOR PYROMETER TEMPERATURE.....	164
FIGURE 10.1 TOPOGRAPHY OF VICINAL (1120) Al_2O_3 SURFACE AFTER ANNEALING.	166
FIGURE 10.2 TOPOGRAPHY OF 500 NM THICK (001) IR SURFACE GROWN ON A- Al_2O_3	167
FIGURE 10.3 PLOT OF (002) IR LINEWIDTH $I(111)/I(002)$ FOR DIFFERENT T.....	167
FIGURE 10.4 (002) IR LINE WIDTH AND $I(111)/I(002)$ VS. FILM THICKNESS.....	168
FIGURE 10.5 (002) IR LINEWIDTH AND $I(111)/I(002)$ VS. AR PRESSURE.	169

Images in this thesis are presented in color.

1 Chapter 1 Introduction

Diamond is a wide bandgap semiconductor with an unusual combination of extreme physical properties. Many are well-known, such as unequalled mechanical hardness, a thermal conductivity greater than copper at room temperature, negative electron affinity, and high transparency in the visible and near-ir spectral region. Others, such as high carrier mobilities, dielectric breakdown field, and resistance to radiation damage, make diamond attractive for applications as energetic particle detectors. In the future, detectors will be required for environments with orders of magnitude more radiation intensity [1], leading to severely reduced time before replacement of the silicon detectors presently in widespread use. Diamond can be a superior alternative, provided it can be produced as high-purity, large-area single crystals. Natural diamond cannot satisfy these needs as its quality is highly variable and suitable material is far too expensive. CVD polycrystalline diamond is generally unsuitable for high-performance detectors as intrinsic electronic properties are degraded by the presence of grain boundaries containing graphitic carbon, dislocation networks, and impurity complexes, all of which act as carrier traps [2]. A solution to these problems is provided by pure single crystalline diamond grown by epitaxial CVD. A recent report that CVD homoepitaxial diamond has electron and hole mobilities much higher than that of the best natural diamond [3] has indicated that high-purity diamond offers improved performance over natural diamond, as well as Si. However, it remains unclear whether diamond can be grown by homoepitaxy over sufficiently large areas to satisfy needs in many detector applications.

Heteroepitaxy may provide the means for producing diamond on the wafer scale. The first efforts in CVD heteroepitaxial diamond growth began with the use of Si as a

substrate. However, the large lattice mismatch did not allow true epitaxy, only highly-oriented polycrystalline growth was possible on Si [4,5]. With discovery of thin-film Ir as a suitable buffer layer, grown on MgO, diamond heteroepitaxy became more practical [6-8]. With SrTiO₃ as a substrate for Ir, it was shown that the mosaic spread of heteroepitaxial diamond could be reduced to less than 0.2 deg [9,10]. Discovery of a-plane sapphire (Al₂O₃) as a substrate for (001) Ir led to predictions of wafer-scale size diamond, as sapphire is available as highly perfect crystals up to 25 cm in diameter [11].

In a parallel development, a major advance occurred with the discovery of a region of CVD parameter space in which homoepitaxial diamond could be grown at very high rates [12,13]. Although, the process required the addition of nitrogen, a major electronic impurity in diamond, it increased the possibilities for thick free-standing diamond crystals. Subsequently, growth in the absence of nitrogen led to higher-purity free-standing diamond crystals, albeit at lower rates. Thus, there are prospects that homoepitaxy may yet lead to sufficiently large, detector grade diamond materials [3,14,15].

This dissertation describes a broad investigation of heteroepitaxial and homoepitaxial diamond growth methods. A great deal of attention has been paid to the role of substrates, their growth, characterization, and preparation prior to diamond CVD, including a sputtering process for (001) Ir epitaxy on SrTiO₃ and Al₂O₃. The nucleation of diamond on Ir, intimately connected to the DC bias process, has been examined, with investigation of its temporal and spatial evolution. The early growth and coalescence of diamond crystallites on Ir were also studied. By modification of the plasma-sample environment, growth processes were developed that have led to 8 mm dia heteroepitaxial

diamond films. With a two-step process, such films were grown to thick films with quality approaching that of natural diamond.

In homoepitaxial diamond growth, the role of several process parameters on structural and chemical quality, and growth rate, was investigated. A process was developed that led to $4 \times 4 \times 0.5 \text{ mm}^3$ free-standing homoepitaxial diamond crystals with low defect levels.

The dissertation contains seven chapters. Following this Introduction, Chapter 2 covers the basic properties of diamond, its historical classification schemes, and the role of impurities. Chapter 3 provides a review and background for heteroepitaxial and homoepitaxial diamond growth. The role of DC bias in enhancing diamond nucleation, and associated physical models of the process, are presented. Homoepitaxial growth and the influence of plasma CVD parameters are then discussed. Chapter 4 describes several analytical tools used to measure the physical properties of CVD diamond. Chapter 5 presents the details of the present CVD heteroepitaxy research: Ir epitaxy, DC biasing, and the two-step process. Chapter 6 describes homoepitaxial diamond growth: substrate preparation, growth parameters, the role of nitrogen and subsequent nitrogen-related electronic centers. Chapter 7 summarizes the major results and makes suggestions for further work.

2 Chapter 2 Structure and properties of diamond

2.1 Crystal structure

Diamond has the face centered cubic (FCC) structure with two lattice points in the primitive unit cell, one at (000) and the other at $(\frac{1}{4} \frac{1}{4} \frac{1}{4})$. It can be viewed as the superposition of two FCC lattices, one displaced relative to the other along the body diagonal by one quarter of the lattice parameter from the origin. Its cubic lattice parameter at room temperature is 0.357 nm. Every carbon atom in the lattice is bonded with four other carbon atoms to form a tetrahedral structure. Four valence electrons in each carbon atom form strong covalent bonds by sp^3 hybridization with nearest-neighbor bond length 0.154 nm. Figure 2.1 shows the unit cell of diamond. It is associated with $(Fd\bar{3}m)$ or O_h^7 space group, which has a total of 48 symmetry operations.

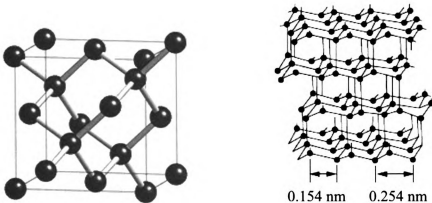


Figure 2.1 Crystal structure of diamond

There are eight carbon atoms in the cubic unit cell with an effective packing fraction of about 34 %. Diamond has the shortest bond length of any three-dimensional

crystal and a binding energy of 347 KJ/mol [16], which makes it the hardest material known.

2.2 Band structure

Diamond and Si have quite similar electronic band structures. The energy difference between an electron in the lowest level of the conduction band and the highest level of the valence band, the electronic bandgap, is 5.5eV for diamond, almost five times that of Si (1.12eV) [16]. The band structure of diamond, calculated using the linearized augmented plane wave method (LAPW) [17], is shown in Figure 2.2.

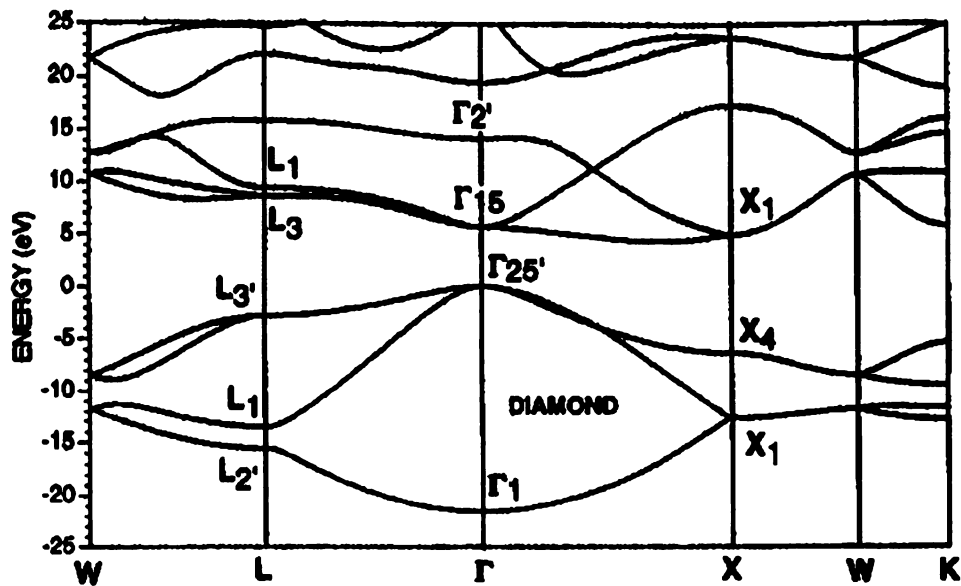


Figure 2.2 Electronic band structure of diamond [17]

Conduction band minima occur along $\langle 100 \rangle$ direction at nearly 0.7 of the distance to the edge of the Brillouin zone at X. The valence band maximum occurs at the center of the Brillouin zone, Γ . Thus, the minimum bandgap in diamond is indirect.

2.3 *Historical classification of diamond types: impurities*

Natural diamond has been classified historically by the nature and concentration of impurities. Almost all diamond, natural or synthetic, always contains as impurities small atoms such as nitrogen or boron. There are several classes of impurities: (1) substitutional impurities in which a foreign atom replaces a carbon atom with minimal distortion of the lattice, (2) interstitial impurities, (3) impurities associated with lattice vacancies and (4) inclusions, in which aggregates of elements such as Al, Ni, and Mg are non-crystallographically inside crystals. Table 2.1 shows historical classification of diamond types, based primarily on included impurities. For example, Type Ib diamond is defined on the basis of its substitutional N concentrations, which imparts a yellow color to natural stones. Diamond grown by the high-pressure, high-temperature (HPHT) method, not only contains N from its growth in air, but also may contain Al, Ni or Fe impurities, since they are used as catalysts in the growth process. However, the very short C-C bond in diamond does not allow many elements to be incorporated substitutionally. The major impurity centers involve N, B, P, S, Si and Ni.

Table 2.1. Diamond classification according to the amount of lattice impurity [18]

Diamond Type	Nitrogen (ppm)	Boron (ppm)	Color
Ia	2000	-	Clear to yellow
Ib	$10^2 - 10^3$	-	Green, brown, yellow
Ib	1-100	-	Yellow
IIa	~1	-	Colorless clear
IIb	~1	~100	Blue

2.4 Physical Properties

2.4.1 Electronic Properties

Because of the large bandgap, pure diamond is highly resistive at room temperature but its resistivity decreases at higher temperatures. Common dopants are B, N and P. B-doped diamond has p-type conductivity with an acceptor level that lies 0.36 eV above the valence band [19]. Heavily B-doped diamond was recently found to exhibit type-II superconductivity below 4 K [20]. N and P-doped diamond have n-type conductivity with donor levels that lie 1.7 and 0.6 eV below the conduction band minimum, respectively. Although some studies have shown that S provides n-type conductivity with an activation energy of 0.37 eV [21], more recent work has suggested that these results are spurious and result from other dopants [22]. Recent conductivity measurements on heteroepitaxially-grown single crystal diamond have shown that the conductivity and carrier activation energy are comparable to natural Type IIa diamond [23]. These data are shown in Figure 2.3.

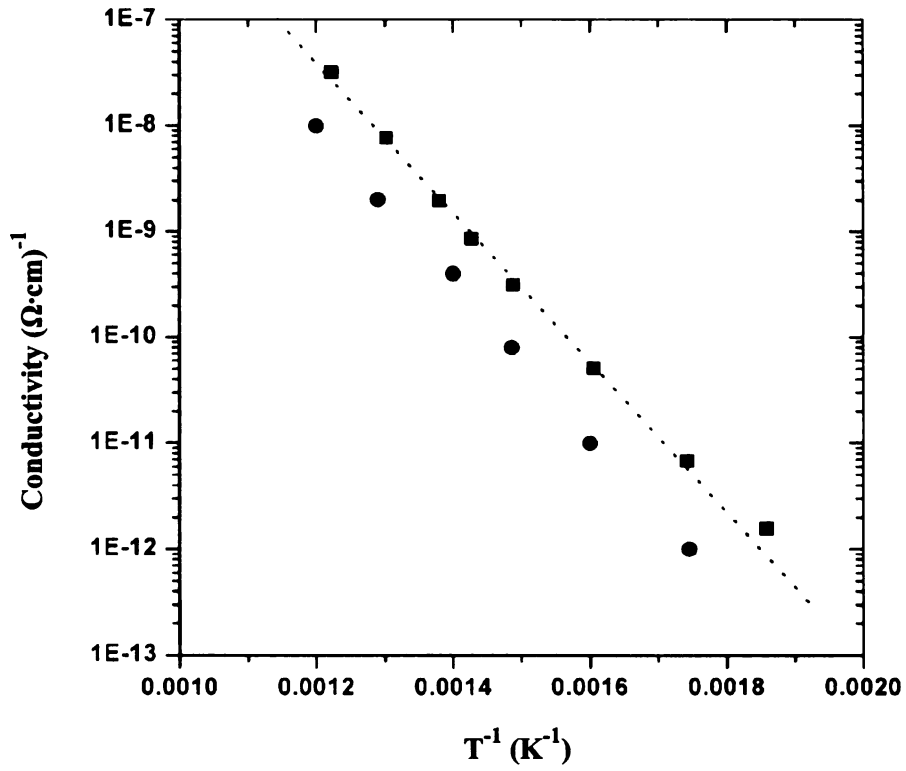


Figure 2.3 Electrical conductivity vs. reciprocal temperature for heteroepitaxial diamond (■), natural Type IIa diamond (●) [23].

Chemical vapor deposition (CVD) diamond is grown in the presence of hydrogen so that its surface is naturally hydrogen-terminated. Such diamond exhibits p-type surface conductivity. It can be destroyed by oxygen-termination, which can be accomplished by immersing the diamond in a strong acid or by short exposure to an oxygen plasma.

Electrons and holes in diamond have high mobilities with respect to other semiconductors. Table 2.2 [16] compares several electronic properties of common semiconductors with diamond.

Table 2.2 Room temperature carrier mobilities of diamond and other semiconductors [3]

Semiconductor	Electron mobility ($\text{cm}^2/\text{V}\cdot\text{s}$)	Hole mobility ($\text{cm}^2/\text{V}\cdot\text{s}$)	Breakdown electric field (V/cm)	Bandgap (eV)
Natural diamond IIa	2000-2800	1800-2100	10^7	5.5
Homoepitaxial diamond	4500	3800	10^7	5.5
Silicon carbide	700		3×10^6	3.26
Gallium nitride	2000		2.0×10^6	3.0
Gallium arsenide	8500		4.0×10^5	1.42
Silicon	1500	450	3.7×10^5	1.12
Germanium	3900	1900	2.0×10^5	0.66

Note that the room temperature mobilities for homoepitaxial CVD diamond [3] are surpassed only by values for GaAs. At high temperatures, semiconductor carrier mobility decreases because of increased phonon scattering. Figure 2.4 shows the temperature dependence of the electron mobility in un-doped CVD diamond. The behavior in the higher temperature region has been attributed to scattering by optical phonons whereas at lower temperatures acoustic phonon scattering is implicated [3].

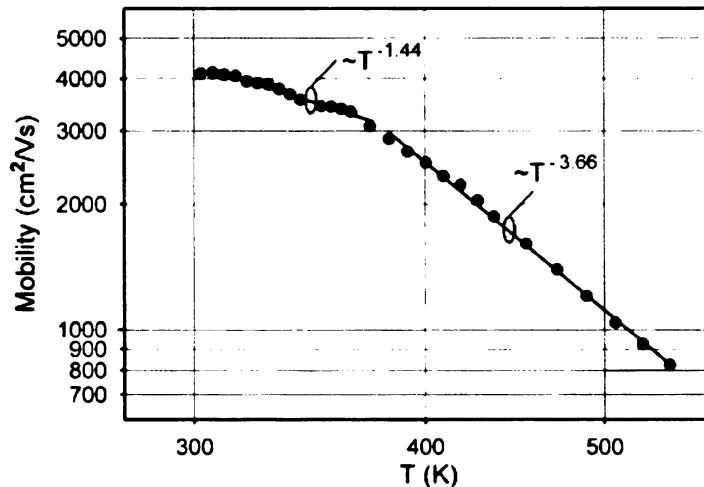


Figure 2.4: Temperature dependence of electron mobility in homoepitaxial CVD diamond [3]

Other important room temperature electronic properties of diamond are its high dielectric breakdown field ($10^7 \text{ V}\cdot\text{cm}^{-1}$), high carrier saturation velocity ($10^7 \text{ cm}\cdot\text{s}^{-1}$), and high thermal conductivity ($20 \text{ W}\cdot\text{cm}^{-1}\cdot\text{K}^{-1}$), almost five times greater than for Cu. Many of these electronic properties position diamond as a favorable material for applications in high power, high temperature electronics.

2.4.2 Optical properties

To the eye, pure diamond is clear and colorless. Type IIa diamond, with its low impurity content, is highly transparent in the spectral region from 225 to 2500 nm [24]. Impurities give rise to absorption bands and the coloration given in Table 2.1. Figure 2.5 shows the intrinsic absorption spectrum of very pure diamond in the visible and uv region. The rapid increase in absorption in the ultraviolet region just below 225 nm, represents the onset of inter-band transitions just above 5.5 eV. Because of the indirect bandgap, band-to-band luminescence is largely quenched since high-energy phonons must participate to conserve momentum.

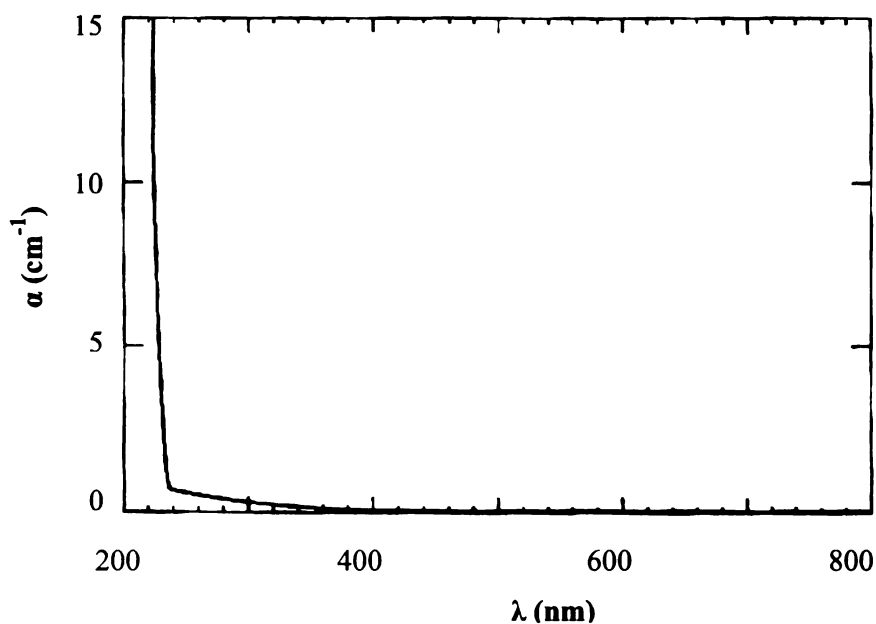


Figure 2.5 Absorption spectrum of a highly pure Type IIa natural diamond [24]

Pure diamond exhibits considerable absorption in the infrared region between 0.2 and 0.5 eV as shown in Figure 2.6. This absorption arises from one, two and three-phonon processes. The lowest ir-active optical vibrational frequency corresponds to 0.165 eV so this sets a cut-off for single-phonon absorption. The absorption at the highest energies in figure 2.6 is due to the involvement of three phonons with a cut-off around 0.495 eV [24].

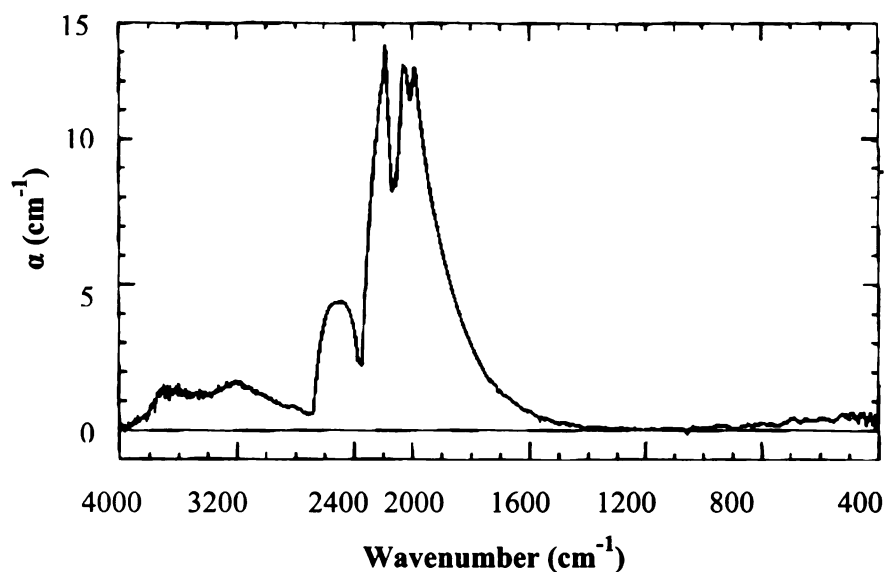


Figure 2.6 Infrared absorption spectrum of a highly pure Type IIa natural diamond [24].

2.4.3 Optical properties of impurity-related defects

Nitrogen is the most common impurity in natural, HPHT and CVD diamond. It appears in many different configurations. Nitrogen in pair-wise aggregated form, sometimes called an A center appear, when two nitrogen atoms replace adjacent carbon atoms. It is found in Type Ia(A) diamond. Its infrared absorption signature consists of a major peak at 1282 cm^{-1} and another at 1212 cm^{-1} . In the uv region, a sharp absorption peak appears at 320 nm (4 eV) [25]. When four nitrogen atoms replace four carbon atoms from the lattice sites surrounding a vacancy, then a B optical center is formed. This is found in Type Ia(B) diamond. It gives rise to broad absorption in the ir centered at 1185 cm^{-1} [26]. Three substitutional nitrogen atoms and a vacancy give rise to the N_3 optical center, with a sharp absorption band at 415 nm in the near-uv [24]. N-based platelets have been identified in Type Ia(B) diamonds, consisting of the interstitials ejected from B

type aggregates, with absorption at 1365 cm^{-1} in the ir [27]. Nitrogen in interstitial form, sometimes referred as Type Ia(H) diamond, shows a peak in the ir at 1450 cm^{-1} [28].

Nitrogen-vacancy complexes are another class of impurity centers found in natural as well as CVD diamond. When a substitutional nitrogen atom is adjacent to a vacancy, it forms a nitrogen-vacancy center, or $(\text{N-V})^0$, in its neutral charge state. It gives rise to a 2.156 eV (575 nm) zero phonon line (ZPL) luminescence. It can trap an electron to form a $(\text{N-V})^-$ center, with a ZPL at 1.945 eV (637 nm) [29].

Impurity-related defect populations are not independent of one another. For example, if Type Ia(A) diamond is irradiated and annealed above $650\text{ }^\circ\text{C}$, an A aggregate captures a vacancy to form an H_3 optical center with a ZPL at 2.463 eV. B aggregates irradiated and annealed under the same conditions may capture a vacancy to form the H_4 optical center with a ZPL at 2.498 eV [26].

Type Ib diamond, by definition, contains predominantly dispersed, singly substitutional nitrogen. This simple impurity is sometimes referred to as a C center. It acts as a deep donor with activation energy 1.7 eV and gives rise to ir absorption at 1130 cm^{-1} and 1344 cm^{-1} . It also contributes to a rapid rise in absorption just below 2 eV (600nm). An ionized nitrogen donor N^+ gives rise to an ir absorption line at 1332 cm^{-1} [26].

Boron in Type IIb diamond acts as an acceptor, with a series of hydrogenic levels starting at 2460 cm^{-1} (0.304 eV) with other lines at 0.347, 0.349, and 0.362 eV [30].

Transitions to the valence band extend into the red, giving rise to a characteristic blue color.

Silicon- and hydrogen-related defects have also been identified in CVD diamond, with Si originating from glass window contamination and H from the feed gas. A Si-vacancy ZPL is observed at 1.681 eV (738 nm) [26]. C-H vibrational modes in the region from 2750 to 3100 cm^{-1} have been seen in polycrystalline CVD material [31] and attributed to H-termination at surfaces or hydrogen bound at grain boundaries.

3 Chapter 3 Growth of Diamond by CVD

In this chapter we review the basic principles of nucleation and growth which apply to the deposition of diamond by the chemical vapor deposition (CVD) process. CVD is a generic method whereby chemical reactions are induced at relatively low pressures by energy supplied to reactive gases by heating, often by the creation of a plasma discharge. The products of the reaction are collected on a substrate located in close proximity to the focus of the chemical reactions. The process is continuous in that, as reagents are depleted, they are exhausted and replenished by allowing for continuous output and input flows. After chemical constituents are deposited, the formation of solid structures can be further manipulated by diffusion rate control via substrate temperature. Diamond growth by low-pressure CVD is particularly significant as it represents a method for the formation of a metastable crystallographic phase. Since graphitic carbon represents the ground state of carbon under typical terrestrial temperatures and pressures, formation of diamond by CVD relies on the presence of molecular hydrogen, which alters chemical kinetics to favor diamond (sp^3 bonded carbon) formation rather than that of graphite (sp^2 bonded carbon).

Before reviewing previous research on diamond growth by heteroepitaxy and homoepitaxy, we first discuss general aspects of epitaxy and nucleation and growth.

3.1.1 Epitaxy and epitaxial growth

The ordered growth of a crystalline material on another crystalline substrate is called epitaxial growth if at least one crystal plane of the deposited crystal and one of the

substrate are parallel. For example, growth of (001) diamond on (001) Ir such that a $\langle 110 \rangle$ direction of both crystals are parallel to each other would satisfy this definition.

In heteroepitaxy, given similar crystallographic structures, the lattice parameter of the deposited crystal, a_d , and that of the substrate crystal, a_s , differ. We define the lattice mismatch f by $f = (a_s - a_d)/a_d$. If the deposited and the substrate crystal have different crystal structures, then the mismatch in atomic spacing on the contacting substrate plane and the deposited crystal plane is more relevant than the lattice parameter mismatch. For epitaxial growth, small f is generally desirable so that better atom-to-atom registration occurs. Systems with large f will have large strains induced at the interface (provided that f is not an integer or a small rational fraction). Interfacial strain can be accommodated by the formation of defects, in particular, by the formation of dislocations. The density of such misfit dislocations is generally proportional to the degree of mismatch.

3.1.2 Nucleation

Nucleation is the process by which a substance undergoes a phase transition by first creating small domains of the new phase within the parent phase. A first order phase transition occurs when thermodynamic fluctuations initiate the continuous growth of the new phase within a small temperature or pressure range. It is believed that fluctuations of a thermodynamic order parameter must exceed a critical value before the phase transition occurs. For example, the spatial region over which the new phase forms must exceed a certain value, the size of the critical nucleus. Once the fluctuation exceeds this value, energy considerations will favor growth of the new phase from the nucleus, and the volume of the new phase grows. However, additional kinetic considerations may

influence the growth rate of the new phase. Nonetheless, nucleation is the essential beginning process that precedes crystal growth.

3.1.3 Crystal growth modes

It is generally accepted that there are three major modes possible in epitaxial growth, when there is no interdiffusion between the substrate and the deposited phase [32,33]. In three-dimensional island growth, or Volmer-Weber growth, small three-dimensional clusters form directly on top of the bare substrate and then grow into islands. This is most likely when the atoms of the deposited crystal are more strongly bound to each other than to the substrate atoms, i.e., the surface energy of the deposited crystal is much larger than that of the substrate crystal, $\gamma_d + \gamma_i > \gamma_s$, where γ_d , γ_i and γ_s are, respectively, the surface energy of the deposited crystal, the interfacial energy, and the substrate surface energy [32].

A second possible mode is two-dimensional layer-by-layer or Frank-van der Merwe growth. Here, the deposited crystal wets the substrate surface, which means that the deposited crystal atoms bind more strongly to the substrate atoms than to themselves. At first, atoms that condense on the substrate form a complete monolayer then, the next successive layers cover the preceding ones. In this case one has the relation, $\gamma_d + \gamma_i < \gamma_s$.

The third common mode, layer plus island growth, or Stranski-Krastanov growth, is a combination of the preceding two modes. Here, the growth of the first few monolayers proceeds layer-by-layer, but eventually this mode becomes energetically unfavorable and the mode changes to island growth. Although there may be several reasons for this to occur, the most probable reason arises from an increase of the

interfacial energy as the thickness of the deposited crystal increases. The condition for layered growth to take place is $\gamma_d + \gamma_i < \gamma_s$, but if γ_i increases with the thickness of the deposited layer, at a critical thickness this relation is no longer satisfied and the mode switches to island growth. Figure 3.1 shows a schematic representation of the three types of growth modes.

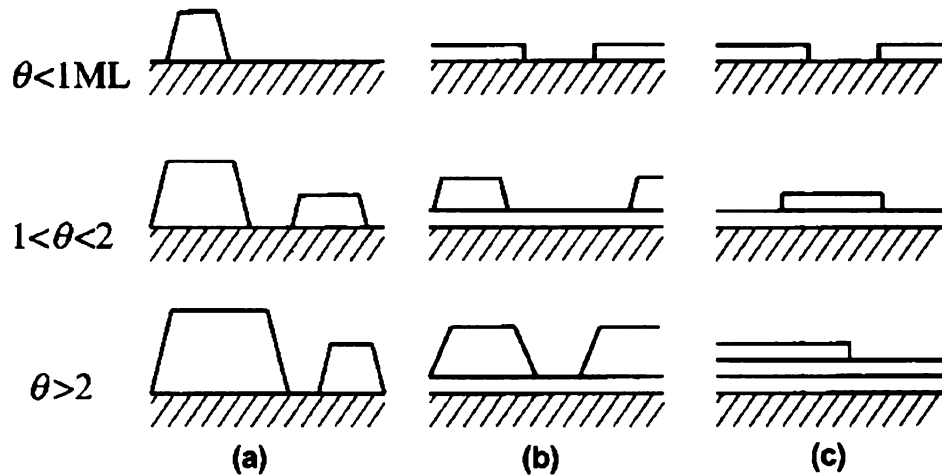


Figure 3.1 Crystal growth modes as a function of surface coverage θ in terms of monolayers (ML) (a) island or Volmer-Weber mode (b) layer plus island, or Stranski-Krastanov mode (c) layer-by-layer or Frank-van der Merwe mode [32].

3.1.4 Substrate criteria for diamond heteroepitaxy

For heteroepitaxial growth of diamond the following substrate criteria are desirable.

1. Crystal structure: diamond has a cubic structure so that substrates with cubic structures are often advantageous, but not absolutely necessary.
2. Lattice parameter: a lattice parameter that is a close match to that of diamond, 0.357 nm, is helpful.

3. Surface energy: an equivalence of surface energy density between substrate and diamond is advantageous. Otherwise 3D island growth will occur, which ultimately requires coalescence of islands into a continuous film. This opens up opportunities for defects to form at the coalescing surfaces. Surface energies of diamond are quite large, e.g., for (111) and (100) planes they are 5.3 and 9.2 J/m², respectively [34].
4. Coefficient of thermal expansion: for growth at high temperatures, unequal thermal expansion coefficients match lead to high interfacial stress after cooling to room temperature. Large thermally-induced strains may lead to fracture of substrate or epilayer.
5. Physical and chemical properties: substrate melting point should be much higher than the growth temperature. Substrate should have structural phase stability between room temperature and growth temperature. Chemical stability at the growth temperature is important: reactions that form carbides must be avoided. For example, although Ni has only a 1.3% mismatch to diamond, it forms carbides at diamond growth temperatures leading to an interface unsuitable for epitaxy.

3.1.5 Epitaxial diamond growth on different substrates

As a working definition of diamond heteroepitaxy, we adopt the following criteria.

1. Growth over areas of 1 mm² or larger.
2. Structural confirmation by diffraction of epitaxial crystallographic registration. A measure of mosaic spread, or average angular misalignment of grains, from

diffraction linewidths, preferably much less than 1 deg. For example, highly oriented diamond (HOD), grown on Si substrates, shows some degree of epitaxial alignment but presents an x-ray linewidth of several deg.

At present, many substrates have been evaluated for purposes of diamond epitaxy. Silicon has been more extensively tested than any other material as it would allow integration with much semiconductor technology [4,35-38]. Si has a lattice parameter 0.543 nm, 52% larger than that of diamond, but with an identical structure. Despite a large mismatch, (001) HOD has been grown on Si. A 16 μm thick diamond film grown with microwave plasma CVD yielded a (004) x-ray linewidth of 2.1 deg [39].

Cubic boron nitride (c-BN), with the zincblend structure and a 0.361 nm lattice parameter, 1.3% greater than diamond, was explored several years ago as a substrate for diamond epitaxial growth [40,41]. A 0.2 μm thick continuous film was grown over a region of 200 μm [40]. An epitaxial relationship was confirmed by reflection high energy electron diffraction (RHEED), although no linewidth were reported. However, the growth of c-BN is difficult and is limited to small sizes [42].

Silicon carbide (β -SiC), with the zincblend structure and a 0.436 nm lattice parameter, 22 % larger than diamond, has been grown on Si as a film and used as a substrate for subsequent HOD growth [43,44]. A diamond film with area greater than 1mm^2 has been grown [44]. The epitaxial relation was established by x-ray diffraction and an (004) linewidth of 0.6 deg measured.

(111)-oriented HOD was grown on (111) Pt, in bulk and thin film form [45-48]. Pt is FCC with lattice parameter 0.392 nm, almost 10 % larger than that of diamond. A

1.5 μm thick film was grown on a $10 \times 10 \text{ mm}^2$ area with a (111) linewidth of 1.1 deg [49]. An epitaxial relationship was established by x-ray diffraction.

(111) and (001)-oriented diamond were grown on Ni substrates[50-52]. Ni is FCC with lattice parameter 0.352 nm, just 1.3 % smaller than that of diamond. A 30 μm diamond film was grown on Ni with (100) and (111)-oriented grains. Ni has been reported to form nickel hydrocarbide [50] or a nickel carbide [52,53] at a growth temperature, of 900-950 $^{\circ}\text{C}$.

(111)-oriented diamond films were grown on $10 \times 10 \text{ mm}^2$ Re buffer layers on c-plane Al_2O_3 [54]. The (111) tilt and twist were reported to be 4.8 and 3 deg, respectively, much larger than for diamond grown on $\beta\text{-SiC}$.

3.1.6 Heteroepitaxial diamond growth on iridium

Ir has the FCC structure with a lattice parameter 7.5% larger than that of diamond and was first used as a substrate for diamond growth in 1996 [6]. It is the Pt-group element with lowest carbon solubility [55] and shows no phase transition between room temperature and its melting point of 2450 $^{\circ}\text{C}$. Epitaxial Ir can be grown on oxide substrates and used as a buffer layer for diamond growth. Several groups have already demonstrated diamond epitaxy on Ir [6,8,56-58].

Ohtsuka et al. [6,7,59] grew (001) diamond on 500 nm RF sputtered Ir on cleaved (001) MgO using DC plasma CVD. A 8 μm thick freestanding film of about 2 mm^2 area exhibited a Raman linewidth of 18 cm^{-1} , an order of magnitude greater than the intrinsic

diamond linewidth at room temperature. No x-ray linewidth was reported for this crystal [60].

The use of SrTiO₃ as a underlying substrate for a (001)Ir buffer layer [9] led to an epitaxial diamond film[10,56]. The 34 μm freestanding diamond film had a (004) x-ray linewidth of 0.17 deg and (311) linewidth of 0.38 deg [10], and led to the establishment of a cube-on-cube epitaxial registration.

A freestanding 25 μm single crystal diamond film was grown on electron-beam evaporated Ir on SrTiO₃ [58]. Improvements in nucleation density were shown to yield coalescence of diamond grains after a shorter growth period. Epitaxial (001) diamond was also grown on Ir evaporated on a-plane Al₂O₃, which has a complex hexagonal crystal structure [61]. Al₂O₃ has a coefficient of thermal expansion closer to diamond than SrTiO₃ leading to less thermal stress in the diamond film at room temperature.

Epitaxial (100) CaF₂ and Ir were sequentially grown on (100) Si by e-beam evaporation after which (100) diamond was grown on Ir. After 2 h growth, no diamond coalescence was observed by SEM. No thickness and linewidth information was reported for this film [62].

Recently, epitaxial diamond was grown on Ir, which was grown on thin-film SrTiO₃ grown by molecular beam epitaxy on Si. Growth of Ir on yttria-stabilized zirconia (YSZ) was also demonstrated [63,64].

3.2 Bias-enhanced nucleation (BEN)

BEN commonly refers to a process in which diamond nucleation density is increased significantly by applying a negative bias (voltage) to the substrate at the beginning of the CVD process. The terms bias treatment, bias process, ion-enhancement or ion-irradiation are also used. With negative bias, positive ions from the plasma bombard the substrate surface. The process was first used by Yugo et al. to grow diamond on Si [65]. They reported a nucleation density 10^{10} cm^{-2} at -70 V bias. The nucleation density without BEN was not reported in this study, but has subsequently been reported to be 10^4 cm^{-2} [66]. It was proposed that, during BEN, positive ions accelerated toward the substrate increased active hydrocarbon species at the sample surface due to collisions between ions and substrate, which consequently led to increased nucleation density [65,67]. When the DC bias is applied, an additional discharge appears, referred to as the secondary plasma. This forms over the substrate above the dark space.

3.2.1 BEN mechanisms

Five different mechanisms that have been proposed to explain the increased diamond nucleation due to BEN on Si are: (1) ion subplantation, (2) non-diamond carbon layer deposition, (3) increased surface diffusion, (4) formation of a SiC buffer layer and (5) electron emission.

Ion subplantation is the deposition of hyperthermal ($1-10^3 \text{ eV}$) species by shallow sub-surface implantation [68]. Robertson et al. [66,69] found the ion subplantation in Si to be most efficient around 80-100eV ion energy [66]. They measured ion energies in BEN at -250 V bias using a retarding field probe (inserted through a hole in the sample)

that had a distribution peaked at 80 eV. They proposed that subplantation creates nanocrystalline graphitic carbon and that diamond nucleates where the graphitic planes are locally oriented perpendicular to the surface. The graphitic carbon is able to accommodate the 2:3 lattice mismatch between diamond and silicon. Molecular dynamics (MD) simulations calculated an ion energy spread of 40-70 eV [70] and ion-beam mass spectrometry measurements indicated average energies between [71,72] 50-70 eV for -200 V bias. These results suggested ion subplantation to be the dominant effect during BEN on Si.

Combining the results of MD simulations and experiments, Lifshitz et al. [68,73] proposed a model of diamond nucleation on Si due to ion subplantation during BEN. Here, a dense amorphous hydrogenated carbon (a-C:H) phase about 1-2 nm thick is formed by subplanted ions. Spontaneous precipitation of a pure sp^3 carbon cluster, containing tens of atoms of the a-C:H phase, is induced by a thermal spike created by the impinging energetic species. A few of the clusters are diamond (1 out of 10^4 to 10^6) and they grow at the expense of the sp^3 carbon in its vicinity.

Other studies have suggested that ion subplantation is not able to nucleate diamond [74,75]. The average energy of impinging ions was estimated to be only 15 eV for -200 V bias. A threshold bias voltage, -100 V, was necessary for this process to be effective [76]. Below the critical voltage, impinging ions are not energetic enough to overcome the nucleation barrier.

Electron energy loss spectroscopy and TEM showed a 4nm thick amorphous carbon layer after BEN at -200 V [74]. The ion energy was estimated as 20 eV, at most.

The negative bias led to the formation of a thin amorphous carbon layer with nucleation sites formed as the amorphous carbon layer was deposited.

Another study, using optical emission spectroscopy (OES) at -150 V bias, [77] showed an increased amount of atomic hydrogen at the sample surface during the BEN. The atomic hydrogen preferentially etched the sp^2 carbon, stabilizing the sp^3 carbon clusters. The thin layer of sp^3 carbon provided the nucleation sites for diamond.

In other experiments, the formation of a nm thick SiC layer on top of the Si surface was demonstrated [78-81]. The SiC layer is usually believed to be oriented but in one case it has been claimed to be amorphous [82]. Subplantation of carbon into the SiC layer causes carbon supersaturation, resulting in the subcutaneous formation of epitaxially oriented nucleation centers in the SiC layer [80].

In other studies, BEN has been found to simply increase the atomic diffusion of C on the Si surface [83,84]. Jiang et al. used -150 V bias to induce nucleation on silicon, with 3D non-faceted diamond islands initially formed. The size of the islands increased as biasing progressed. They claimed formation of a depletion zone between the islands, attributed to the enhanced diffusion of carbon by ion bombardment during the biasing.

In addition to the nucleation enhanced by the ion bombardment, in some experiments electron emission from diamond has been suggested to lead to nucleation enhancement. Biasing experiments done under identical conditions with a bare Mo holder, a diamond-coated Mo holder, and an uncoated sapphire holder yielded different results. Much higher nucleation densities were obtained with the diamond-coated holder and bias current increased almost five-fold. Experiments with the other holders showed no increased nucleation [85].

Enhanced nucleation was also achieved when a tungsten ring inserted between the substrate and a hot filament was negatively biased at -300 V relative to the hot filament [86,87]. It was claimed that this result was due to electron emission from the diamond-coated tungsten ring.

3.2.2 Biasing experiment with Ir

In comparison to Si, relatively few studies have examined the role of biasing on Ir substrates. In some studies, it was reported that the Ir surface is roughened during BEN [6,88]. X-ray photoelectron spectroscopy (XPS) and RHEED of an Ir sample ion-irradiated at -260 V in a DC plasma CVD system showed that the Ir surface is roughened during ion irradiation. XPS did not show any compound formation between Ir and C or H, but did indicate the presence of a thin layer of amorphous carbon [6].

Ir roughness was reported at the diamond-Ir interface by cross sectional HRTEM after ion irradiation at -260 V for 10 min followed by 30 min of growth in a DC plasma CVD [89]. No interlayer formation such as IrC or complex hydrocarbon compounds of Ir, was found. The top surfaces of the Ir were proposed as diamond nucleation sites.

Diamond crystallites nucleated along [110] ridges of an Ir surface after biasing at -120 V for 15 min in an antenna-edge type CVD system. Nucleation was viewed as more likely on areas of Ir that protruded into the plasma. After growth for 2 min diamond crystallites smaller than 10 nm in size were etched away by a hydrogen plasma. It was concluded that a critical size for diamond crystallites exists [90].

X-ray photoelectron spectroscopy (XPS) and x-ray photoelectron diffraction (XPD) studies on Ir surface after a bias treatment showed no layers that could be

associated with compounds of Ir, C and H, but almost 20 monolayers of amorphous carbon on the Ir surface was detected. XPD measurements also detected nm-sized diamond crystallites after BEN with no growth; however, they were not seen in low energy electron diffraction (LEED) [91,92].

The structural effects of biasing were studied with SEM, AFM and TEM. Two different types of furrows and ridges along $\langle 100 \rangle$ and $\langle 110 \rangle$ were reported after 45 min of bias at -250 V. Shape, dimensions and the crystallographic alignment of the furrows and ridges changed with different methane concentrations [93-96]. In addition, 5-10 nm structures were found with a typical distances of 100-300 nm. 30 min of growth resulted in similar densities of diamond crystallites [93]. In another study after 45 min bias at -250 V, a smooth Ir surface with less than 1 nm average surface roughness was observed. After 30 min of growth, diamond crystallites grew on the flat Ir surface as observed in TEM. No evidence for any intermediate layer of amorphous C was detected [97].

In a HRTEM study, 5-10 nm nanoparticles were found to lie on top of diamond grown on Ir. HRTEM revealed the lattice parameter of the nanoparticles to be that of Ir. The particle density was close to 10^{11} cm^{-2} , 3 orders of magnitude higher than that of diamond nuclei [94].

Domains, several μm in size, were observed by SEM to form after bias with negligible topographic features. After the growth step, only the domains developed into islands of epitaxial diamond. Outside these domains, either the nucleation density was orders of magnitude lower or the diamond grains were misoriented [98]. In a combined AFM and SEM study, in addition to 2-3 nm roughening of domains, the domains were found to be 1 nm lower than the surrounding layer. It was suggested that domain

formation is a continuous process during the bias procedure, which starts from a local nucleation event and subsequently grows [99].

More recently, in a HRTEM study a 0.75 nm carbon layer was seen on the Ir surface after biasing for 50 minutes at -250 to -280 V. After 2 min of growth, diamond crystallites up to 8 nm in height were observed. Amorphous carbon deposited during the BEN was etched by the plasma during this short growth step [95]. It was suggested that the surface roughening of the Ir that occurs in most cases is not essential for diamond nucleation. During biasing, the initially deposited amorphous carbon layer is densified by ion bombardment and diamond nucleates in a large fluctuation caused by a preferential displacement process induced by an impinging ion.

In summary, how biasing leads to nucleation or to enhanced nucleation density on Ir is still imperfectly understood. Most studies agree that the Ir surface is roughened during biasing and that a thin layer of amorphous carbon is deposited; yet, one study claimed that the Ir surface can remain smooth during biasing under the same conditions and diamond can be grown on this surface. Thus, two basic questions that need resolution are: how does roughening of the Ir surface evolve with biasing and is roughening responsible for enhanced nucleation?

3.3 *Homoepitaxy*

3.3.1 Background

The first homoepitaxial diamond growth by the microwave plasma CVD method was first reported by Kamo et al. in 1988 by growing on a polycrystalline diamond substrate [112]. After this demonstration, homoepitaxial growth was investigated on

natural or HPHT Type Ib substrates. Growth rates were typically lower than 1 $\mu\text{m/h}$ [100-107]. Also, methane concentrations, usually defined as the ratio of methane to hydrogen flow rates, had to be maintained at 0.025% to suppress growth of defects. Three kinds of macroscopic defects are commonly observed in homoepitaxial diamond: nonepitaxial crystallites (NC or UC), pyramidal hillocks (PH), and macro-step bunching (B) [108]. The first two defects are serious as they cannot be reversed, whereas the third type is less problematic. Takeuchi et al. [108] grew homoepitaxial diamond films on substrates with different misorientation angles from the (001). They produced a map of diamond surface morphologies as a function of misorientation angle and methane concentration as shown in Figure 3.2.

Atomically Flat

20 μm

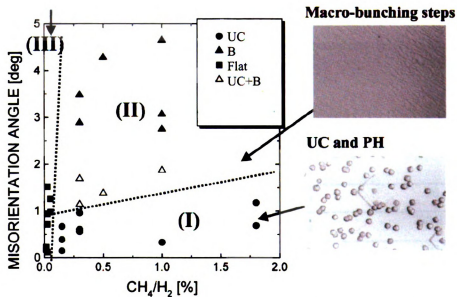


Figure 3.2 Map of surface morphologies as a function of misorientation angle from the $\langle 001 \rangle$ and methane/hydrogen ratio. Three types of morphologies appear. Atomically flat diamond is preferred, which only grows in region III [108].

However, more recent work has shown that a different region of parameter space can be effective in growing diamond at much higher rates. Yan et al. grew diamond at rates approaching to 40 $\mu\text{m}/\text{h}$ in the presence of nitrogen [12] with growth temperature 1500 $^{\circ}\text{C}$, pressure 150-200 Torr and methane concentrations from 1 to 6%. Later, growth rates were increased to 150 $\mu\text{m}/\text{h}$ by introducing 1-5 % N_2 relative to methane flow, and methane flow up to 12 % of hydrogen flow [13].

More recently, by lowering the growth temperatures to 700-800 $^{\circ}\text{C}$ and by increasing microwave power density at the substrate, fairly high growth rates were achieved in the absence of nitrogen [14,15,109-111]. In addition, whereas gas pressures

previously used ranged from 20-50 Torr [112], for high rate growth pressures were increased to 100-200 Torr. Former microwave power densities were around 5 W/cm³ but for high rates they were increased to 30-100 W/cm³ [112]. To accommodate high microwave power densities without changing growth temperatures, heat must be extracted from the substrate by a cooled stage. Table 3.1 summarizes differences between low and high growth rate regimes.

Table 3.1 Low and high growth rate regimes in microwave plasma CVD diamond growth

Parameter	Low growth rate	High growth rate
Power density(W/cm ³)	5	30-100
Substrate temperature (°C)	600-900	700-1200
Gas pressure (Torr)	20-50	100-200
Growth rate (µm/h)	<1	100 µm/h with N ₂ 20µm/h without N ₂

3.3.2 Growth of defects

3.3.2.1 Pyramidal hillocks (PH) and non-epitaxial crystallites (NC)

On the (001) diamond surface, the most commonly occurring defect is the pyramidal hillock, either with a flat top surface or with a sharp truncated top containing a non-epitaxial crystallite [113,114]. The sides of this hillock are aligned with [110]. Under favorable conditions, this hillock grows very rapidly compared to its surroundings. Hillock growth is favored at high temperatures and high methane concentrations [14]. Figure 3.3 shows a homoepitaxial diamond surface covered with these defects [115].

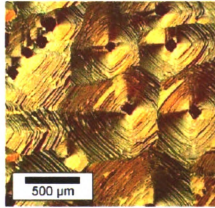


Figure 3.3 Pyramidal hillocks with non-epitaxial crystallites at the top (dark particles) [115].

According to Lee et al. [116-118], the type of growth strongly depends on the diffusion of the growth species on the surface, the rate at which growth species are deposited on the surface from the vapor phase, and the width of the terraces on the growth surface. If the terrace width is long compared to the diffusion length, then the growth species tend to deposit on the middle of the terraces, instead of diffusing to the steps. This results in two-dimensional nucleation, as shown in Figure 3.4. Then, the two-dimensional nuclei provide shorter steps for further growth along the sides of the hillock. Non-epitaxial crystallites are believed to grow on surface defects by enhanced secondary nucleation [113,116]. At higher temperature these non-epitaxial crystallites grow very fast and provide step edges for further growth.

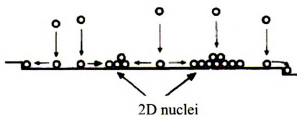


Figure 3.4 Mechanism of two dimensional nucleation on a wide terrace. Beginning of hillock growth [116].

3.3.2.2 Step bunching

If the diffusion length of the growth species is larger than the terrace width, the growth species diffuse toward the steps [116] because of the lower potential there. In this growth mode, the steps appear to flow across the growth surface. A schematic view of the step flow growth mechanism is shown in Figure 3.5. Step flow growth in diamond is favored at higher temperatures, low methane concentrations and high misorientation angles of the substrate surface. Several reports have appeared on single crystal diamond growth in step flow mode using vicinal substrate surfaces [115,119,120].

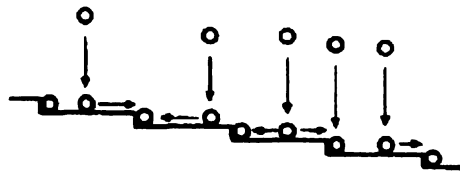


Figure 3.5 Schematic view of step flow growth showing the diffusion of growth species to steps and subsequent flow of steps to the right [116].

During growth, impurities or defects may block the transport of growth species or adsorbates to a particular step [121,122] so that flow ceases, but other steps will flow to that position and become pinned. If this process continues, many steps will become bunched at that position leading to a macroscopically high step. This is referred to as macro-step bunching. Figure 3.6 shows macro-step bunching in homoepitaxial diamond [123].

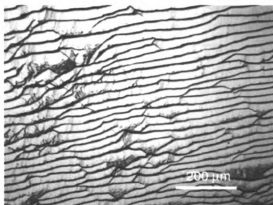


Figure 3.6 Macro-step bunching in homoepitaxial diamond [123]

3.3.3 Effect of growth parameters

3.3.3.1 Substrate temperature

Substrate temperature during diamond growth plays a most important role. It significantly affects growth rate and the crystalline quality of the diamond. The growth rate R_g of homoepitaxial diamond was found to obey an Arrhenius relationship between 800-1000 °C [112,124] with $R_g = A \exp(-E_a/k_B T)$, where E_a is an activation energy and T is the growth temperature. Diamond growth in this temperature region is controlled by chemical reaction kinetics rather than by surface diffusion. Above 1000 °C, the growth rate no longer obeys the above relation, but saturates. Here, growth changes to a diffusion-controlled mode, with a weaker temperature dependence. Values of E_a for temperatures between 735-970 °C were reported as 8 ± 3 , 18 ± 2 and 12 ± 4 kcal mol⁻¹, respectively, for (100) and (110) and (111) diamond surfaces [125]. Different growth conditions and reactor geometries will change E_a , so that the use of these parameters may be sensitive to local conditions. Figure 3.7 shows a plot of growth rate vs. substrate temperature.

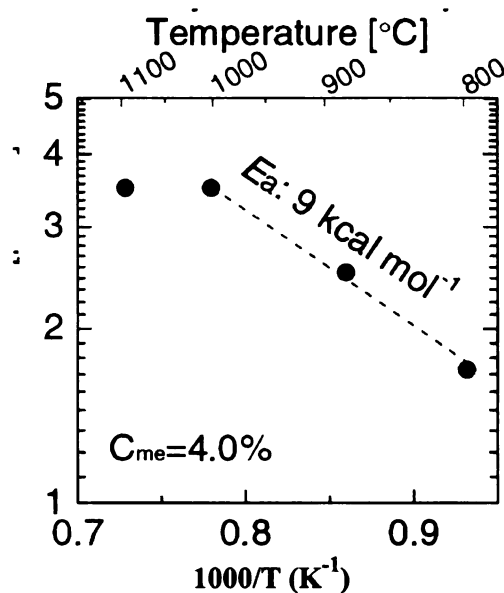


Figure 3.7 Diamond growth rate as a function of substrate temperature for 4% methane concentration [112].

At temperatures above 1200 °C, graphite starts to form [112]. At temperatures lower than 700 °C, diamond growth rate is very low and the substrate becomes highly pitted [126]. On the other hand, the growth of smooth, almost atomically flat, diamond also has been reported at 700 °C [15]. This apparent contradiction may not exist if growth depends also on other parameters such as methane and nitrogen concentrations, and reactor geometries. Usually there is a small temperature window in which defect-free diamond can be grown with other conditions fixed.

3.3.3.2 Methane concentration

Methane concentration in the gas phase significantly affects the diamond growth rate and the morphology of diamond. The growth rate is generally found to be linearly proportional to methane concentration. Figure 3.8 shows a plot of growth rate vs. methane concentration at 850 °C without nitrogen from Achard et al. [126].

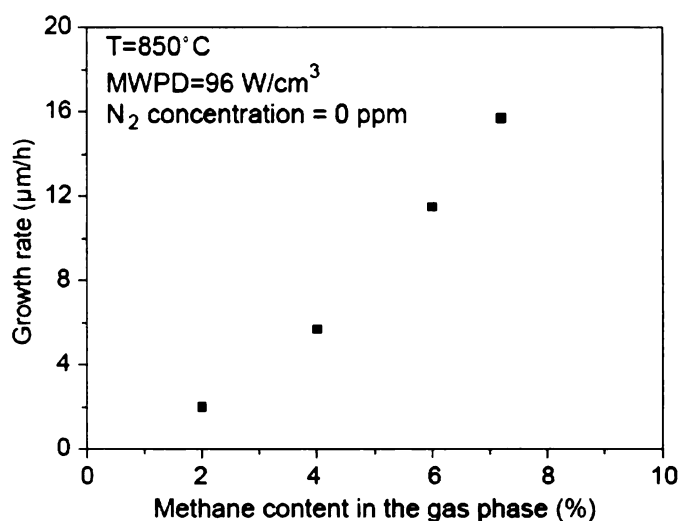


Figure 3.8 Growth rate as a function of methane concentration at 850 °C without nitrogen [126].

The above data indicate a slightly supra-linear relation between methane concentration and growth rate. In contrast, Bogdan et al. [127] reported an sub-linear result. Teraji et al. [112] reported a supra-linear relationship from 1 to 5% methane but then a linear dependence up to 32 % methane at 890 °C. Whereas, the growth rate always increases as methane concentration increases, the proportionality coefficient can be sensitive to other growth parameters.

Bogdan et al. [127] reported a smooth diamond surface grown at 15% methane concentration at 700 °C. In contrast, Achard et al. [126] reported macro-step bunching on the diamond surface when they increased the methane concentration from 4 to 6%. At 2 % methane concentration, they found the diamond surface to be highly pitted. Teraji et al. [112] observed the formation of large hillocks, different from pyramidal hillocks, at 16% methane concentration and small faceted structures at 1% methane concentration. They

attributed it to different growth modes occurring at widely different methane concentrations [112].

3.3.3.3 Process gas pressure

The total process gas pressure has an influence on the size and energetics of the microwave plasma. As pressure increases, the size of the plasma ball becomes smaller, since the mean free path of the ions becomes shorter. This influences the substrate temperature, since the power density may become greater in the vicinity of the substrate. In a microwave plasma CVD system, the electrons in the plasma are accelerated by the high frequency electric field, but the ions cannot follow the microwave field, leading to a low ion temperature. The ion temperature can be increased by enhancing collisions with hot electrons, brought about by a higher gas density. When the total gas pressure is low, the ionization rate in the plasma is also low with only a relatively small number of electrons available for creating atomic hydrogen and hydrocarbon radicals. At higher pressures and power densities, the ionization rate is higher and the frequency of collisions between the ions and electrons become larger, which increases the ion temperature. This ultimately leads to an increase in the density of hydrocarbon growth species and atomic hydrogen. Mokuno et al. [128] found the growth rate increasing almost linearly with pressure in their microwave plasma CVD reactor in the presence of nitrogen. Yan et al. [12] reported a five-fold increase in growth rate, when the pressure was changed from 60 to 200 Torr.

3.3.3.4 Microwave power density

Microwave power density is found to strongly affect the growth rate. Tallaire et al. [129] observed a three-fold increase, from 3 to 8.5 $\mu\text{m}/\text{h}$ in growth rate, with a change of power density from 65 to 125 W/cm^3 . They also used a pulsed microwave source to increase the peak power density and while maintaining a constant average power density. They observed an increased growth rate of 40%, with the conclusion that peak power density, not average power density, is responsible for the enhanced growth rate. Teraji et al. [112] saw little difference in growth rate when the power density changed from 40 to 50 W/cm^3 .

3.3.3.5 Nitrogen

Nitrogen is the most common impurity in natural, HPHT, and CVD diamond. As discussed earlier, nitrogen forms several defect centers in diamond, in conjunction with other nitrogen atoms or with vacancies. In CVD diamond the most common nitrogen center is singly substituted nitrogen. Substitutional nitrogen reduces the optical transparency in the region above 1.7 eV and in the one-phonon region in the ir beyond 9 μm . In addition, during CVD growth, nitrogen has beneficial effects on the surface morphology, growth rate and the promotion of (001) growth. Addition of nitrogen to the gas phase during diamond growth on Si, changes the growth habit from (111) to (001) and increased the growth rate by a factor of two on the (001) surface at low nitrogen to carbon ratios [130]. In homoepitaxial diamond growth, adding controlled amount of nitrogen increased the growth rate to more than 100 $\mu\text{m}/\text{h}$ [13,131]. So far, the mechanism by which nitrogen influences the (001) diamond growth is not well

understood. Mechanisms such as surface poisoning or the generation of additional growth steps have been considered [132]. According to a theory based on defect-induced stabilization of diamond growth [133], diamond growth is only thermodynamically possible by the creation of vacancies, since a diamond vacancy can be created with lower energy than a graphite vacancy. If nitrogen is doped into diamond, the Fermi level at the growth surface is shifted towards the conduction band, which reduces the energy of vacancy formation in diamond, but not in graphite, so that diamond growth is favored over graphite.

3.3.4 Growth anisotropy: the alpha parameter

The diamond growth parameter α is defined as the ratio of the growth rate normal to (001) with the growth rate perpendicular to a (111) surface, usually written as,

$$\alpha = \sqrt{3} V_{(001)}/V_{(111)}$$

where $V_{(001)}$ and $V_{(111)}$ are the diamond growth rates on the (001) and the (111) diamond surfaces, respectively [134]. The equilibrium shape of a diamond crystal depends upon the growth rate anisotropy, thus on α . Shapes of diamond crystal for different values of α are shown in Figure 3.9 [135]. If $\alpha = 1$, then the fastest growth direction is normal to (111) so that no (111) facets appear. For α larger than 1, (111) faces of diamond appear because the fastest growth direction is no longer normal to (111) surface. For $\alpha = 3$ the fastest growth direction is normal to (001) and the crystal shape is an octahedron.

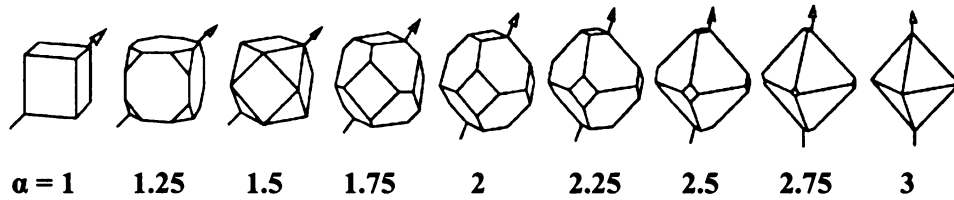


Figure 3.9 shape of diamond crystals for different value of α . The arrow shows the fastest growth direction for that α [135].

Although the value of the parameter depends upon the overall growth conditions, it is found to be larger for higher methane concentrations and lower temperatures in general. In actual experiments, growth occurs on many crystal planes, not only on (001) or (111), but also on (110) and higher index planes, so it is difficult to accurately predict the overall crystal shapes from a single parameter [136].

4 Chapter 4 Materials Characterization Methods

4.1 Optical Microscopy

Optical inspection and photography are valuable tools for the examination of surface features of crystalline materials. With optically transparent crystals, several methods exist for providing optical contrast. The differential interference contrast (DIC) microscope converts the gradients in the specimen optical path length into amplitude that can be visualized as enhanced contrast of the resulting image [137]. A general schematic of such a microscope is shown in Figure 4.1

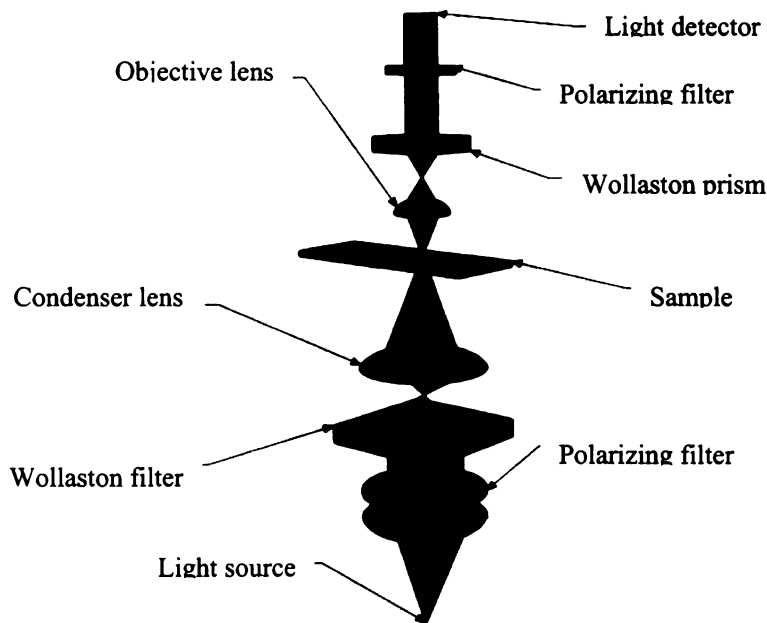


Figure 4.1 Schematic of a differential interference contrast (DIC) optical microscope

Unpolarized light from the source passes through a linear polarizer to be polarized at 45 degrees, and then passes through the Nomarski-modified Wollaston prism which splits it into two beams with 90 deg polarization differences. The two beams pass through

the condenser lens to be focused on two adjacent points on the sample surface. The beams traverse two slightly different optical paths due to slight topographical variations across the sample thickness. This creates a slight difference in their relative phases. The rays then exit the sample, are focused by the objective, and pass through a second Wollaston prism that combines them into a single beam. Their interference leads to a brightening or darkening of the image at that point, dependent on their optical path difference.

The DIC optical microscope used for this work is the Olympus BX-60, coupled to a digital Spot camera. Digital images were acquired and processed on a computer.

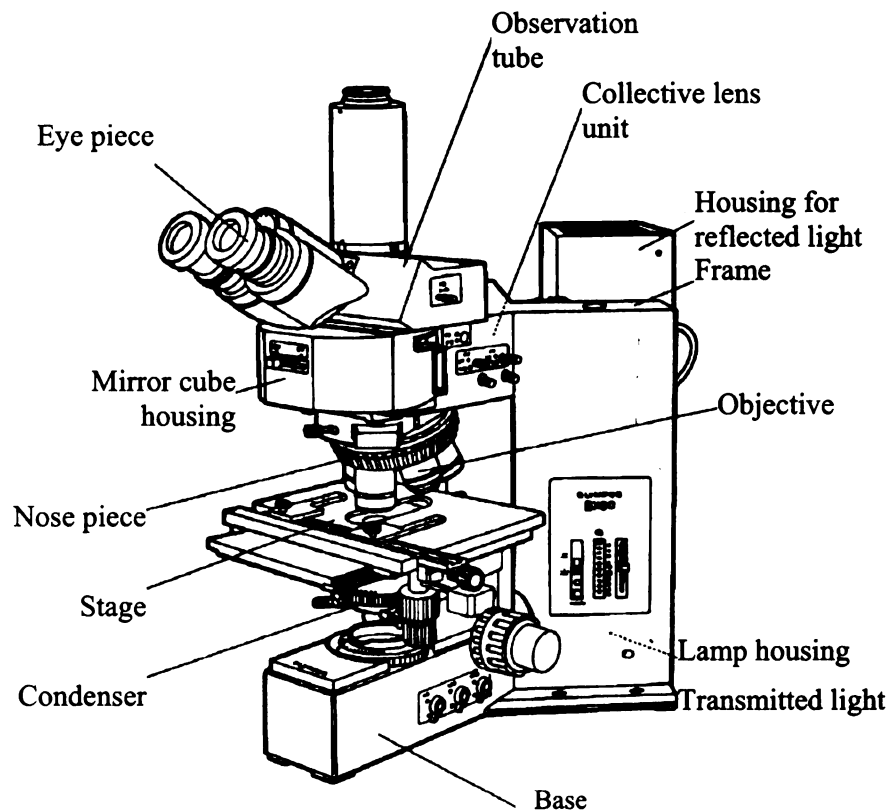


Figure 4.2 The Olympus BX-60 DIC optical microscope

4.2 Atomic Force Microscopy

The atomic force microscope (AFM) is a high-resolution scanning probe microscope. It relies on a sharp tip, with typical radius 10 nm, to map the topography of a surface on a scale of a few nm to 100 μm , while the vertical sensitivity can be 0.1 nm or less. The tip is attached to the end of a cantilever with force constant of order 1 N/m. When the tip is brought to close to a sample surface, the force between the tip and the sample surface deflects the cantilever. The nature of the force depends on their material properties. It can be a magnetic force, electrostatic force or van der Waals force. Deflection of the tip is tracked by a photodiode which detects a laser beam reflected from the back of the cantilever. The AFM in this work was a Digital Instruments DI 3100 scanning probe microscope used in tapping mode. In this mode, a Si tip near the sample surface is driven at its resonant frequency by a piezoelectric tube [138]. As the vibrating tip is rastered across the surface, variations in topography change the external forces acting on the tip. The force changes lead to damping of the tip's vibrational amplitude, which is maintained at a constant level by application of a feedback loop. The system controller interprets the changes in the feedback amplitude as a variation of the surface topography. A schematic of an AFM is shown in Figure 4.3.

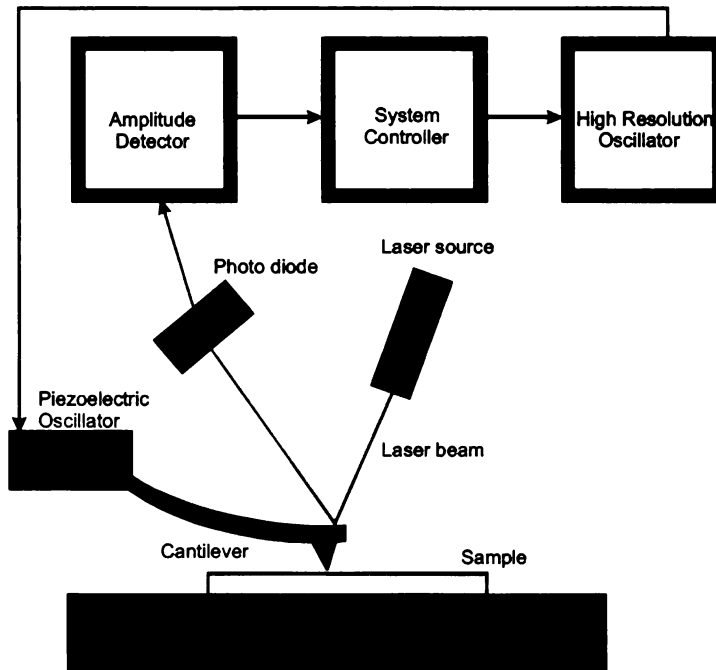


Figure 4.3 Schematic of atomic force microscope

4.3 Scanning Electron Microscopy

The scanning electron microscope (SEM) uses an electron beam to form an image of a sample surface. The electron beam is focused to a nm spot using one or more electromagnetic condenser lenses. The beam then passes through pairs of scan coils in the objective lens assembly which raster the beam in x and y directions across the sample surface. When the primary electron (PE) beam, with energies in the range of 10-30 keV, impinges on the sample, it produces large numbers of radiated electrons and photons. These include secondary electrons (SE), backscattered electrons (BSE), Auger electrons (AE) and x-rays, characteristic of the elemental material [139]. Secondary electrons are the low-energy electrons produced by the inelastic scattering of weakly-bound electrons due to the primary beam. Secondary electrons have energies below 50 eV, with a distribution peaked at 3-5 eV. These electrons are produced within a few nm below the

surface. The number of SE's produced depends on the topographical features of the surface. Steep surfaces and edges produce more SE's than a flat surface. The SE's are detected by an Everhart-Thornley (E-T) scintillator-photomultiplier to form a two-dimensional intensity distribution. The image of the surface is stored by a computer built into the SEM for subsequent processing.

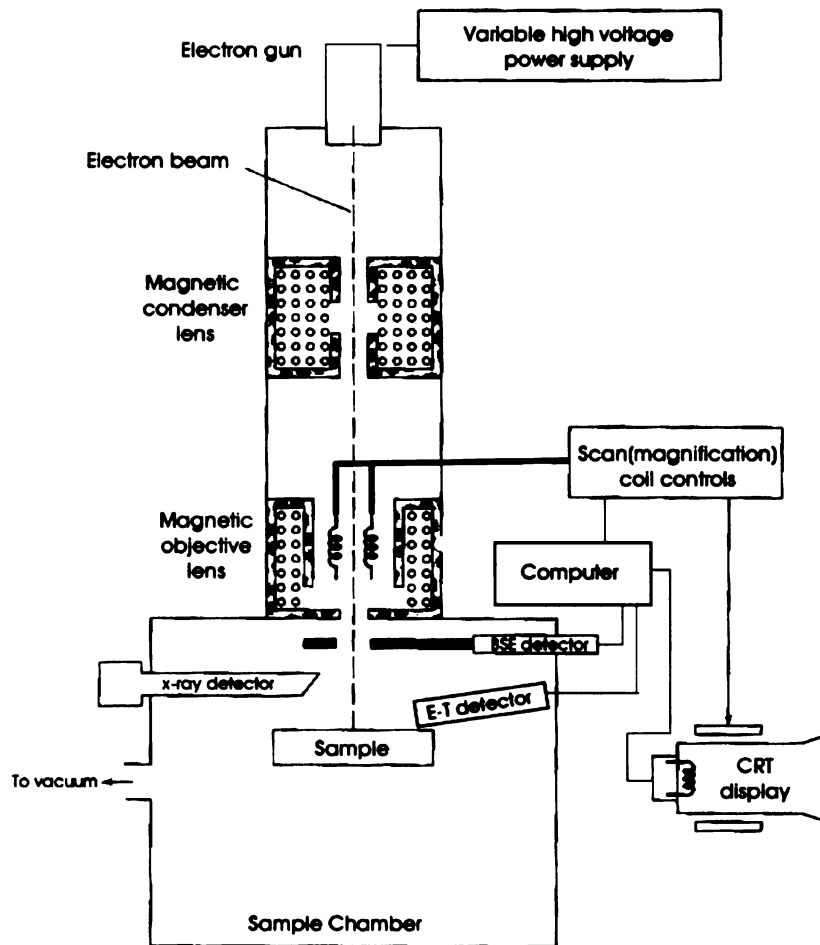


Figure 4.4 Schematic of a scanning electron microscope [140]

Backscattered electrons are also produced in the SEM. The BSE's have a wide energy spectrum, varying from 50 eV to a maximum limited by the applied potential. They also produce SE's and Auger electrons as they propagate through the sample.

BSE's tend to move in linear trajectories. A separate semiconductor detector is used to detect BSE's that gives a signal proportional to the BSE energy. The BSE image carries the information about the atomic number (Z) of the sample, since a larger number of BSE's are produced at larger Z values. BSE images are especially useful for identifying areas with different chemical composition. BSE images have lower resolution than SE images, a result of their larger interaction volume. Finally, x-ray fluorescence is used in energy dispersive spectroscopy (EDS) to identify elements present in a sample.

The SEM used in this research is the Hitachi 4700 field emission SEM (FESEM). This FESEM has a sharp tungsten cathode, with radius of curvature less than 100 nm, as a field emission electron source. The tip of the cathode is biased at a high potential so that the electric field at the tip is of order 10^7 V cm^{-1} . In this field, emission occurs when electrons tunnel through the potential barrier into vacuum. The crossover beam diameter in the FESEM is almost 1000 times smaller than for thermionic emission guns used in conventional SEMs. A FESEM thus requires fewer magnetic lenses to focus the electron beam to a small spot size at sample surface, yielding better resolution than thermionic emission SEMs. The Hitachi 4700 II FESEM contains three sets of electromagnetic objective lenses, two electron detectors and one x-ray detector.

4.4 *Transmission Electron Microscopy*

In a transmission electron microscope a high-energy electron beam interacts with a thinned sample, much less than a μm , with some electrons being transmitted through it to form an image. A simple schematic of a TEM is shown in Figure 4.5.

The nearly monochromatic electron beam emitted from an electron source, a thermionic or field emission gun is focused by a pair of condenser lenses to a narrow

coherent beam. A condenser aperture is used to block electrons emitted at a high angle to the optic axis. The beam of electrons transmitted through the sample passes through an objective lens and then through the objective aperture, which again blocks electrons scattered at high angles. A first image is formed at the image plane of the objective lens before it passes through the intermediate lens. The diffraction information from the sample appears at the back focal plane of the objective. By adjusting the position of the intermediate lens, and with use of different apertures, a highly magnified bright field image, a dark field image, or a diffraction pattern of the sample can be projected on the final fluorescence screen, a photographic plate, or a CCD camera

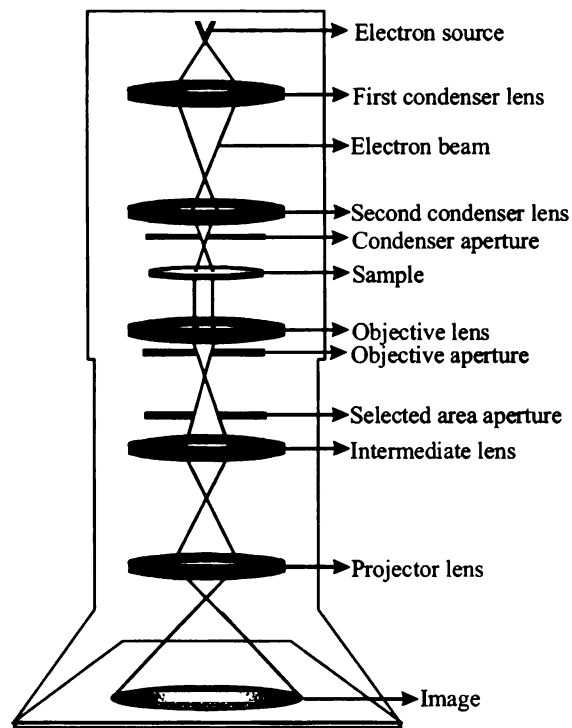


Figure 4.5 Schematic of a transmission electron microscope.

A crystalline material interacts with the electron beam mostly by diffraction so that a characteristic diffraction pattern is generated. A high contrast bright field image is

formed by blocking all the diffracted beams except the central transmitted beam. On the other hand, a dark field image is formed when one of the diffracted beams is used to obtain the final image. The bright field technique can be used to image extended defects such as dislocations or stacking faults.

High Resolution Transmission Electron Microscopy (HRTEM) allows the visualization of atomic-scale crystallographic structures. HRTEM, in contrast to the conventional TEM, uses a phase-contrast imaging technique instead of amplitude-contrast imaging. For phase-contrast imaging, the sample must be sufficiently thin so that amplitude variations do not contribute to image contrast. Because of its very high resolution, ~ 0.1 nm, lattice points and point defects can be resolved.

4.5 Raman scattering and photoluminescence

When monochromatic light interacts weakly with molecules or condensed matter, the scattered light has an inelastic component due to internal vibrational modes. This phenomenon is called the Raman effect [141], shown experimentally by C.V. Raman in 1928. During the scattering, phonon creation is referred to as Stokes scattering, whereas phonon absorption is anti-Stokes scattering. The change in wavelength of the scattered light from the incident light is called the Raman shift, usually expressed in terms of wave numbers cm^{-1} .

In a Raman spectrometer, the laser light scattered by a sample is collected by a lens, often the objective lens in a microscope, then sent through notch filter to remove the elastically scattered light. The light then is dispersed by a holographic grating onto a detector, usually a CCD camera.

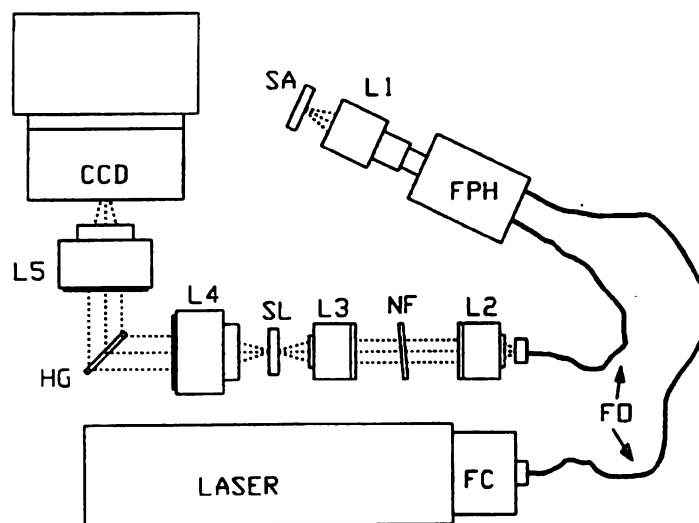


Figure 4.6 Schematic of a Raman spectrometer set up.

FC: fiber optic coupler, FO: fiber optic cable, FPH: fiber optic probe head, L₁: focusing and collection lens, SA: sample, L₂: pre filter collimating lens, NF: holographic notch filters, L₃: post filter focusing lens, SL: spectrograph entrance slit L₄: spectrograph collimating lens, HG: holoplex grating, L₅: spectrograph focusing lens, CCD: detecting CCD camera.

For nominally unstrained diamond, there is only one Raman-active mode, which appears at 1332 cm^{-1} with a linewidth of 1.6 cm^{-1} at room temperature [142]. The actual linewidth will depend on temperature [143], the resolution of the spectrometer, and the structural quality of the diamond. The Raman phonon is three-fold degenerate, but the degeneracy can be lifted by internal strain. For small strain, this may appear as a line broadening. For the Raman measurements described here, a Kaiser Optical Systems Holoprobe Raman spectrometer coupled to an Olympus BX-60 optical microscope was used, with 532 nm laser excitation. A 100x objective was used to focus the laser beam to a diffraction-limited spot, and to collect the backscattered light. This system has available two gratings: a low-resolution grating with a $0\text{ to }4000\text{ cm}^{-1}$ spectral range and a high-

resolution grating with a 1000 to 1600 cm^{-1} range. The best spectral resolution is about 1 cm^{-1} . A schematic of the Raman spectrometer is shown in Figure 4.6.

4.6 X-ray diffraction

X-ray diffraction probes the microscopic atomic arrangement of condensed matter. It is the basic method to analyze the structural organization of a solid's constituent atoms or molecules. For single crystals, the linewidths of diffraction peaks (Bragg reflections) can be used as measures of the internal strain of the crystal. A sample is placed in the path of a monochromatic x-ray beam at an angle ω to the sample surface; the detector is rotated in the scattering plane to observe the diffracted intensity as a function of angle, as shown in Figure 4.7.

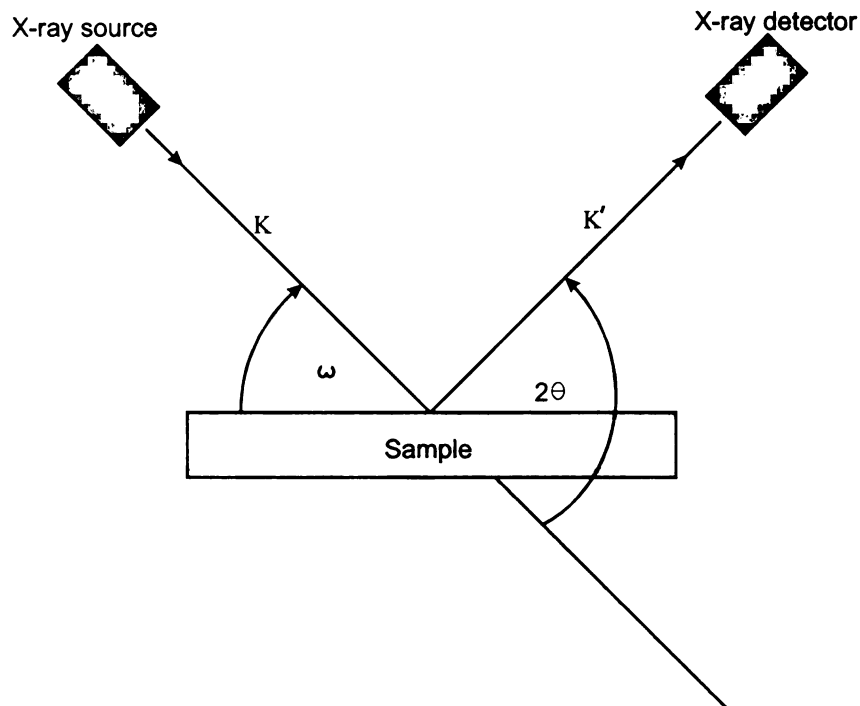


Figure 4.7 Schematic of x-ray diffraction from a crystal.

Diffraction intensity is observed only when the Bragg condition, $2d_{hkl} \sin\theta = n\lambda$, is satisfied [144], where λ is the wavelength of the incident x-ray, d_{hkl} is the lattice spacing between (hkl) planes of the crystal and n is an integer corresponding to the order of the diffraction, as illustrated in Figure 4.8.

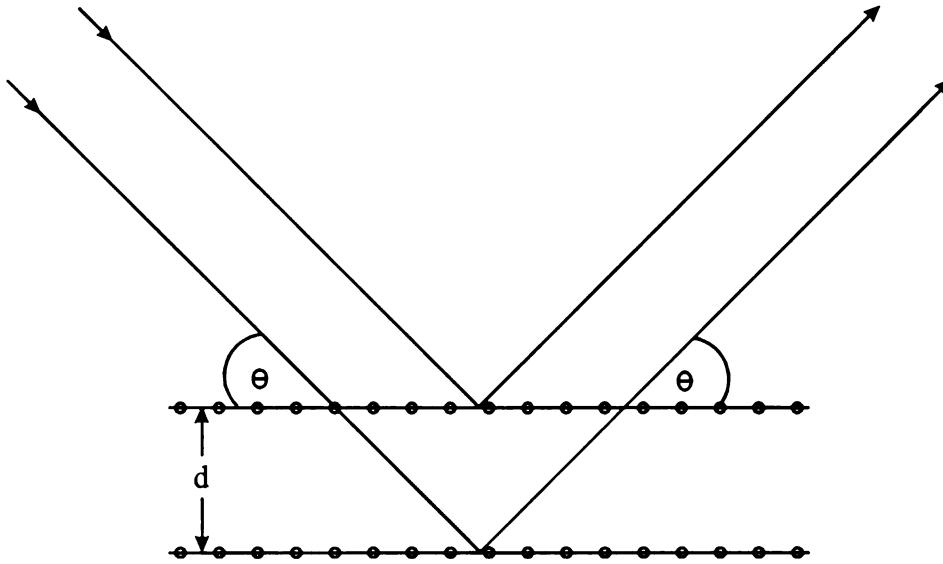


Figure 4.8 Schematic showing the Bragg's law of diffraction

With incoming radiation of wavevector \mathbf{K} , there will be an outgoing wavevector \mathbf{K}' if and only if the relation $\mathbf{K}' - \mathbf{K} = \mathbf{Q} = \mathbf{G}_{hkl}$ is satisfied, where \mathbf{G}_{hkl} is a reciprocal lattice vector with magnitude $2\pi/d_{hkl}$. This is an alternative statement of Bragg's law, which can be visualized by the Ewald construction. An Ewald sphere is drawn with a radius equal to the magnitude of \mathbf{K} in reciprocal space, Fig. 4.9.

$$K - K' = \frac{2\pi}{d_{hkl}} = 2K \sin \theta$$

$$2 \cdot \frac{2\pi}{\lambda} \sin \theta = \frac{2\pi}{d_{hkl}}$$

$$2d_{hkl} \sin \theta = \lambda$$

This is the Bragg equation for the first order diffraction maximum.

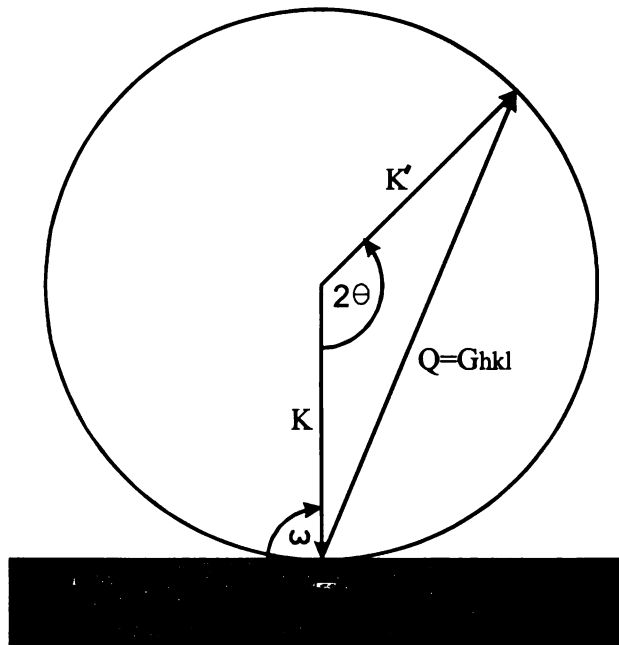


Figure 4.9 Ewald sphere construction

The x-ray diffractometer used for this work is a Bruker AXS D8 instrument, with a 4-circle Eulerian cradle. A vacuum chuck is used to hold a sample on a stage, which can be rotated around three mutually perpendicular axes for ω , χ and Φ circles. To align the sample at the center of the rotation circles, motion in the X, Y, and Z directions is possible. A schematic drawing of this diffractometer is shown in Figure 4.10.

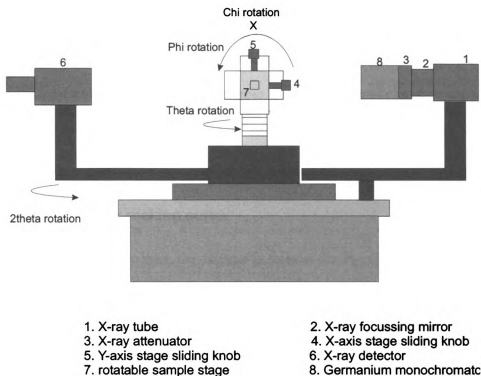


Figure 4.10 Schematic of Bruker AXS x-ray diffractometer

The χ circle is perpendicular to the X-Y plane, the Φ circle lies in the XY plane and the ω , θ or 2θ circles are perpendicular to both χ and Φ . In the schematic, the χ circle is denoted by an "x", which is perpendicular to the plane of the paper or sample. To align the sample, initial conditions are set to $\chi = \omega = 2\theta = 0$ and $\Phi = 90$, the incident x-ray beam, the plane of the sample and the line joining the sample plane and detector all lie in the XY plane and the χ axis becomes parallel to the incident beam. X-rays emitted from a Cu target are focused by a curved multilayer mirror, and then (optionally) pass through a Gee monochromator before they are incident on the sample. All rotations and translations are controlled by a computer which also acquires the intensity data.

4.6.1 ω - 2θ or θ - 2θ scan

For a θ - 2θ scan, the sample and detector both are rotated such that the angular speed of the detector is twice that of the sample. Diffracted intensity is observed when the Bragg conditions are satisfied at particular value of 2θ ; records of intensity vs. 2θ are recorded.

4.6.2 θ or ω scan or rocking curve

For a rocking curve scan, the detector is fixed at the 2θ value that satisfies a Bragg condition, then, the crystal is rotated so that the lineshape of the diffracted intensity can be analyzed. This method is most useful for obtaining the mosaic spread of a crystal from its linewidth.

5 Chapter 5 Heteroepitaxial Growth of Diamond

This chapter describes the processes developed for heteroepitaxial diamond growth. A double epitaxial process has been used, in which an Ir buffer layer is first grown as a thin single crystal film, 300-600 nm thick on an oxide substrate, either strontium titanate (SrTiO_3) or sapphire (Al_2O_3). We first discuss the oxide substrates and their suitability for epitaxy. The Ir growth process on the oxide substrate is then described, as well as methods used to characterize the thin films, particularly AFM and x-ray diffraction. The CVD reactor, sample geometry and the role of the initial DC biasing step to induce nucleation are explained in detail. The resultant products of diamond nucleation and growth are analyzed by SEM, AFM, and HRTEM. The results are used to reach a better understanding of the mechanisms that underline nucleation, growth, and coalescence into thin films of diamond. Experiments to grow diamond with large lateral size are described.

5.1 Substrates

This section describes the properties and structures of Ir, SrTiO_3 and Al_2O_3 , used as substrates for diamond growth. Previous, as well as current work of epitaxial Ir growth on different substrates is first presented, followed by a discussion of the oxides.

5.1.1 Iridium

Ir is a metal with melting point 2454 °C, low vapor pressure (1.47 Pa at 2443 °C) and high (001) surface energy (3.81 J/m^2) surface[145]. It has a FCC unit cell with cubic lattice parameter 0.386 nm. Thin films of Ir have been previously deposited by metal

organic chemical vapor deposition [146,147] pulsed laser deposition [148,149], electron beam evaporation on SrTiO₃ [56] [58,140], and radio frequency magnetron sputtering on cleaved MgO [6,150]. In general, oxide substrates have been used as Ir substrates, including MgO, SrTiO₃, α -Al₂O₃[11], and yttrium stabilized zirconia (YSZ) [151]. Processing of the oxide surfaces is necessary to insure good epitaxy as described below.

5.1.2 Strontium titanate (SrTiO₃)

SrTiO₃ is a cubic perovskite structure with lattice parameter 0.391 nm, 1.7% larger than Ir. Its melting point is 2080 °C. The (001) SrTiO₃ and the (001) Ir surfaces have sufficiently similar lattice parameters that epitaxial growth is easily accomplished.

5.1.3 Sapphire (Al₂O₃)

Sapphire has a hexagonal crystal structure with space group $R\bar{3}C$. Its lattice parameters are $a = b = 0.476$ nm and $c = 1.299$ nm and its melting point is 2040 °C. Epitaxial growth of (001) Ir has been demonstrated on the α -Al₂O₃ (11 $\bar{2}$ 0), or a-plane surface[11] In the a-plane, two orthogonal directions lie along $\langle 0001 \rangle$ and $\langle 1\bar{1}00 \rangle$, the c-axis and m-axis, respectively. The distance between nearest-neighbor oxygen atoms is 0.433 nm along $\langle 0001 \rangle$ and 0.275 nm along $\langle 1\bar{1}00 \rangle$. If the (001) Ir plane is superimposed on this surface with $[110]$ Ir \parallel $[1\bar{1}00]$ Al₂O₃, there is only a 1.2% mismatch. α -Al₂O₃ has two advantages over SrTiO₃: the coefficient of thermal expansion of Al₂O₃ is smaller than that of SrTiO₃, so that thermal stresses in epilayers are smaller

and large wafers of Al_2O_3 are available so that there is no practical limit on the size of diamond films that can be grown on sapphire.

5.1.4 SrTiO_3 preparation

Epitaxial grade SrTiO_3 substrates with (001) surfaces, polished on one side, with dimensions $10 \times 10 \times 0.5 \text{ mm}^3$ were purchased from Mateck. In this investigation two standard sizes were used: 10×10 and $5 \times 5 \text{ mm}^2$ with 0.5 mm thickness. To prepare $5 \times 5 \text{ mm}^2$ substrates, $10 \times 10 \text{ mm}^2$ substrates were coated with photoresist and cut into 4 equal square pieces using a diamond-coated wire saw. Each substrate was ultrasonicated sequentially in acetone, iso-propanol and DI (deionized) water to remove the photoresist. If necessary, they were degreased in Alconox solution in DI water to remove surface particulates. To create an atomically flat TiO_2 -terminated surface, water-cleaned substrates were placed in buffered oxide etch (10 molar NH_4F : HF : H_2O = 12: 1: 20, with pH 5.5) for 10 to 30 seconds. It is believed that water, accelerated by the etch, dissolves the SrO termination and leaves a TiO_2 -terminated surface [152]. This procedure was followed by 3 h annealing in a tube furnace at $925 \text{ }^\circ\text{C}$ in air to allow reconstruction of the surface [152,153]. After annealing, any remaining particulates on the surface were removed by solvent processing.

Figure 5.1 shows AFM images of a (001) SrTiO_3 surface after annealing and cleaning. Figure 5.1(a) shows a terraced surface with terraces separated by steps of 1 unit cell height (0.391 nm). Terraces appear because this crystal surface is miscut by 0.2 deg

from the (001). Figure 5.1(b) shows a perspective view of region (a). Figure 5.1(c) shows a linear scan along the line shown in (a) showing the regular atomic-height steps.

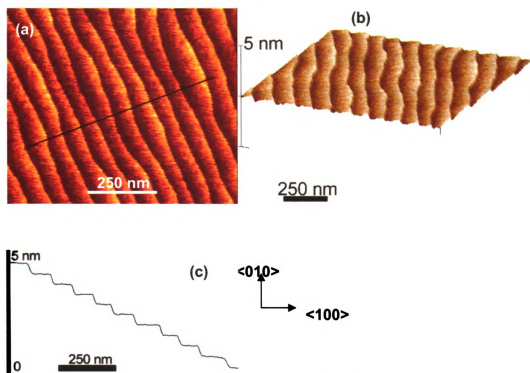


Figure 5.1 (a) AFM image showing the topography of the SrTiO₃ surface after annealing and reconstruction; (b) perspective view of the first image; (c) scan along the line shown in (a) showing the regular steps of atomic height corresponding to the lattice parameter of SrTiO₃.

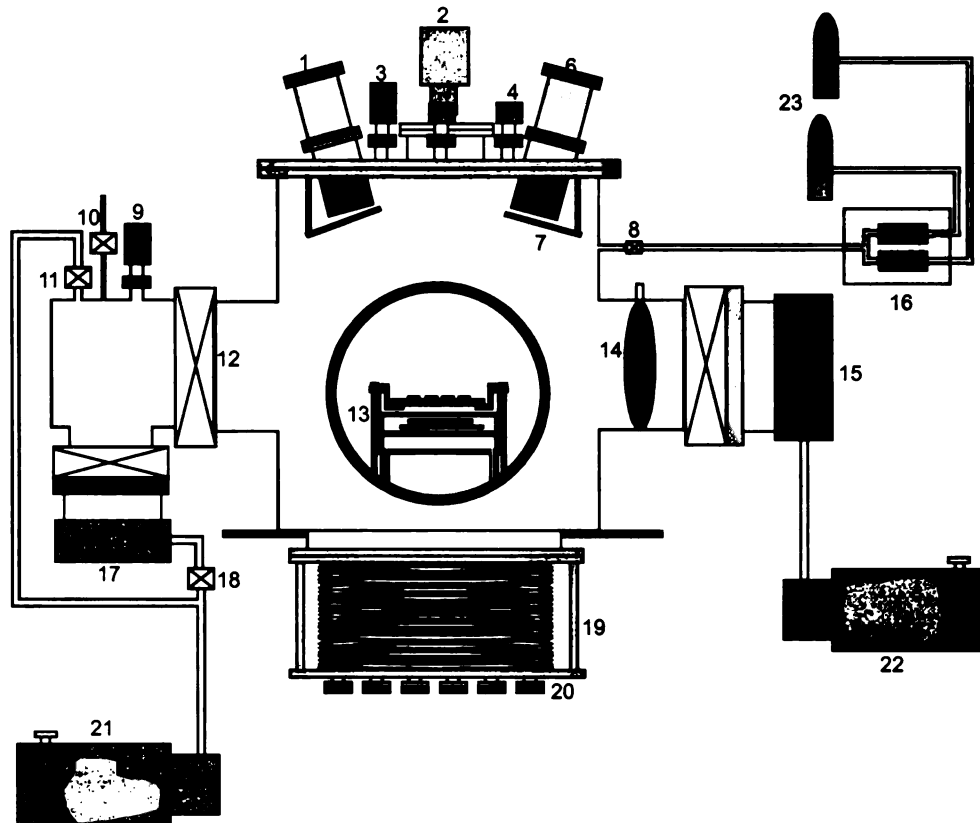
5.2 DC magnetron sputtering of iridium

Sputtering is a process in which positive ions extracted from a plasma impinge on a target, eroding small fragments of the target material which then deposit on an adjacent substrate. If the sputtered material has sufficient mobility on the substrate, it can form a polycrystalline or single crystalline film. To produce epitaxial (001) Ir, it is necessary to sputter onto a heated substrate to suppress the formation of (111) Ir.

5.2.1 Sputtering system

5.2.1.1 Instrument design

Ir films were prepared with a three-gun magnetron sputtering system (APX Instruments) that can be configured for DC or RF sputtering. Power supplies provide a maximum of 1000W for DC and 500W for RF (13.56 MHz) sputtering. The three guns are arranged in confocal geometry, i.e., they are focused onto a central sample stage. This alignment is advantageous for co-sputtering, or for sequential sputtering using multiple targets. The sample holder stage can be rotated to improve homogeneity of the deposit while sputtering. A contact-less SiC heater allows the substrate to be heated to temperatures as high as 1000 °C. A separate load-lock is used for the insertion of samples without the necessity of venting the main chamber to the atmosphere. The system is operated and controlled by a LabView-based interface, developed for this research. A schematic drawing of the system is shown in Figure 5.2.



- | | | |
|----------------------|----------------------|-------------------------|
| 1. DC magnetron gun | 9. Ion gauge | 17. Turbo-pump |
| 2. Pyrometer | 10. Vent valve | 18. Turbo-backing valve |
| 3. Ion gauge | 11. Roughing valve | 19. Movable bellow |
| 4. Capacitance gauge | 12. Gate valve | 20. Feed through flange |
| 5. RGA | 13. Stage | 21. Roughing pump |
| 6. RF magnetron gun | 14. Butterfly valve | 22. Roughing pump |
| 7. Target shutter | 15. Turbo-pump | 23. Gas tanks |
| 8. Gas valve | 16. Flow controllers | |

Figure 5.2 Schematic of the three-gun APX sputtering system

5.2.1.2 Vacuum and gas handling

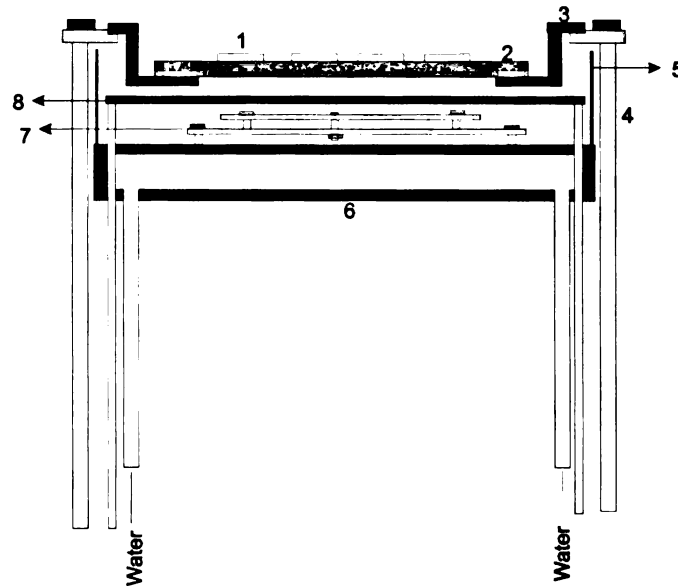
The vacuum system consists of two turbo-molecular pumps (Pfeiffer) and mechanical backing pumps (Alcatel) attached as pairs to load-lock and main chamber. A large gate valve separates the load-lock from the main chamber. The minimum base pressure in the main chamber is 5×10^{-9} Torr after baking for 24 h. A residual gas analyzer (RGA, Ferran) measures the individual partial pressures of residual gases and

also serves as a leak detector. The gas manifold has three mass flow controllers (MKS 1249), which allow the introduction of gases for sputtering. Only pure Ar is used for Ir sputtering. The gas lines are kept pressurized to avoid leaks from outside. A butterfly valve before the turbo pump is used to modulate the amount of gas exhausted through the turbo-pump. The system pressure during the sputtering process is controlled by regulating the Ar flow via a flow controller.

5.2.1.3 Sample stage, sample heating and temperature measurements

A schematic of the sample stage and heater assembly is shown in Figure 5.3. The sample holder assembly is designed so that a carrier, consisting of sample holder base plate and the holder, can be transferred from the load lock to the main chamber using a transfer arm. This requires that the stage height be varied to accommodate the fixed transfer arm. This is accomplished by a motorized stage with ± 7.5 cm travel. A 12.5 cm dia, 2 Ω , SiC heater is used to heat a 7.5 cm dia stainless steel sample holder. Heating is by radiation and the maximum temperature attainable is 1000 °C. The heater does not contact the stage, since it must be free to rotate. Because the heater may draw as much as 15 A, water-cooled leads are required. Two radiation shields were built for thermal radiation trapping to improve heating efficiency. A double-layer circumferential stainless steel shield surrounds the heater assembly while a double-layer Mo shield sits below the heater on the water-cooled stainless steel reflector plate. A K type (Alumel-Chromel) thermocouple tip is attached to the inner side of the stainless steel radiation shield for temperature measurement. Since the thermocouple does not contact the sample holder it is not expected to represent accurately the sample temperature. Instead, sample temperature is measured with a single-color pyrometer (Ircan) mounted outside the

vacuum chamber above the sample holder. The sample is viewed through the top quartz window.



- | | |
|----------------------------------|--|
| 1. Substrates | 5. Stainless steel radiation shield (1 of 2) |
| 2. Stainless steel sample holder | 6. Water-cooled stainless steel reflector |
| 3. Hastalloy disc holder | 7. Molybdenum radiation shields |
| 4. Stage supporting rods | 8. Silicon carbide heater |

Figure 5.3 Schematic of the sample stage of sputtering system. Supporting rod can rotate along with the sample holder. The heater and the cooling lines are fixed.

5.2.2 Sputtering procedure

An abbreviated procedure for sputtering Ir is given here. During sputtering, the deposition rate, sputtering current, sputtering voltage and the thermocouple temperature are monitored by a LabView program. The sputtering power, shutter and valve positions, gas flow, and heater power, are also controlled and monitored by the software.

5.2.2.1 Substrate loading

A 7.5 cm dia stainless steel substrate holder, that can accommodate $25.5 \times 5 \text{ mm}^2$ or $16.10 \times 10 \text{ mm}^2$ substrates, was designed. Substrates are placed in shallow depressions

recessed by 0.5 mm to prevent them from moving. A Si reference substrate, partially covered by a stainless clip, is attached at an empty slot. It is used to record film thickness, which can be measured by AFM or surface profiler.

While in the cleanroom, freshly cleaned substrates are loaded into the stainless steel holder. The substrate holder is then wrapped in aluminum foil to avoid contamination, taken to the sputtering system, and placed onto the load lock transfer arm. When the load lock pressure falls below 2×10^{-7} Torr, the gate valve to the main chamber opens, and the transfer arm inserted until the substrate holder assembly is positioned just above the stage. The stage is then slowly raised using the stage motor. If the alignment is correct, the stage pushes up the assembly and releases the transfer arm. The transfer arm is then removed from the main chamber, the gate valve closed, and the main chamber is further evacuated. The stage is then lowered to its sputtering position, where the target-substrate holder distance is about 24 cm.

5.2.2.2 Sputtering process

For Ir sputtering, the substrate holder is heated to 850 °C, as measured near the middle of the substrate holder. This is accomplished by increasing the heater power to about 60% of its maximum power over a period of 1 h. Once this temperature is reached, the shut-off valve is opened, the butterfly valve is set to its minimum aperture position, and Ar gas introduced at a flow rate of 6-7 standard cubic centimeters per minute (sccm). When the pressure is 12-14 mTorr, the DC power supply is set to 100 W and turned on. At this point, plasma should appear on the target. The flow rate is adjusted to maintain the pressure setpoint. Once sputtering current and process pressure become stable, the

target shutter may be opened, beginning the deposition. The film thickness is monitored by a calibrated quartz thickness monitor inside the main chamber. When the required thickness is reached, the shutter is closed, sputtering power is turned off, the gas shut-off valve is closed, Ar gas flow turned off, butterfly valve is set to maximum aperture position, and the heater is slowly ramped down. After about 2-3 hours when the samples have cooled to room temperature, the substrates are removed through the load lock and stored in the cleanroom.

If the main chamber has been vented to atmosphere, it needs to be baked for 24 h at 50 °C until the base pressure reaches 2×10^{-8} Torr, before sputtering is attempted. If the system must be brought to atmospheric pressure, it is vented with nitrogen to minimize the introduction of water vapor.

5.2.3 Ir growth on SrTiO₃

The main goal of Ir growth is the deposition of an epitaxial (001) Ir film. Departure from epitaxy is assessed by examining the ratio of Ir (002) to (111) x-ray intensities. In addition, a small value of the (002) x-ray linewidth is beneficial for good single crystal diamond growth. In general, the diamond linewidth can not exceed the linewidth of its substrate.

The sputtering parameter ranges investigated here were temperatures between 730 to 930 °C and film thicknesses between 85 to 850 nm. Ar pressure and flow rate were always held at 12 mTorr and 6 sccm, respectively. During the sputtering process, the temperature measured by the pyrometer (focused on the substrate) dropped by 100 °C after the initiation of Ir deposition. Since it is unlikely that the substrate could cool this much, it is

surmised that the pyrometer temperature is representative of the substrate holder temperature, and not the substrate, for the following reasons. Prior to sputtering, the pyrometer would be more sensitive to radiation from the holder, which passes through the transparent substrate, if the substrate were cooler than the holder. Once sputtering began, the apparent temperature dropped because the intervening Ir film blocked radiation from below so that the pyrometer read the Ir surface. The Ir and substrate were actually 100 °C cooler. On the other hand, when the pyrometer was focused on the sample holder, the temperature remained the same before and during sputtering. This is most easily explained in terms of poor thermal contact between the holder and substrate with a temperature difference of about 100 °C.

XRD analysis included a θ -2 θ and rocking curve scans of the Ir film measured with a Bruker AXS x-ray diffractometer using Cu K α radiation (0.154 nm wavelength) at 40 kV accelerating voltage and 40 mA emission current. The (002) Ir linewidth was found by fitting a Gaussian function to the rocking curve data. The Gaussian function $\exp(-x^2/2\sigma^2)$ has a full-width at half-maximum (FWHM) or linewidth equal to 2.354σ .

The surface topography and average roughness of the Ir films were studied by AFM in non-contact mode.

5.2.3.1 Topography and structure of the Ir films

Figure 5.4 shows the topographies of 500 nm thick Ir films grown at four different temperatures between 730 and 930 °C. In each image, unusual stripe-like structures can be seen aligned along [110]. The reason for this anisotropic morphology is not presently clear.

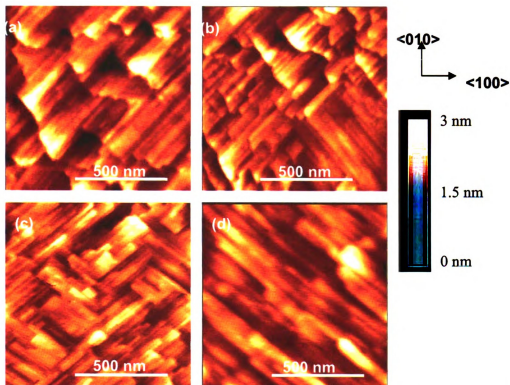


Figure 5.4 Topography of 500 nm thick Ir films on SrTiO₃ grown at different temperatures (a) 730 °C (b) 800 °C (c) 850 °C (d) 930 °C. The fuzziness in (d) is a measurement artifact.

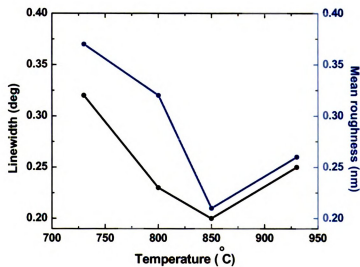


Figure 5.5 Variation of (002) linewidth and mean roughness of the sputtered Ir films with temperature

The 730 °C grown Ir film is quite rough. With higher growth temperatures, the Ir surface becomes smoother. Figure 5.5 shows the variation of average roughness with growth temperature. The lowest roughness occurs at 850 °C. Figure 5.5 also shows a plot of the Ir (002) x-ray linewidth versus substrate holder temperature. The linewidth is a minimum for the film grown at 850 °C.

Figure 5.6(a) shows a θ - 2θ x-ray scan of a 600 nm thick Ir film grown at 850 °C. The Ir (002) reflection, which occurs at $2\theta = 47.3$ deg, is quite strong. Although the Ir (111) reflection has twice the intensity of the Ir (002) reflection, this scan shows no detectable Ir (111) intensity at $2\theta = 40.6$ deg. Here, the ratio of background noise intensity to (002) Ir intensity is 0.0002. Note the logarithmic intensity scale. Some Al reflections, denoted as “Al”, come from scattering by the sample holder and not the sample. Since no monochromator was used here, additional peaks due to Cu K_{β} radiation appear for Ir and SrTiO₃.

Figure 5.6 (b) shows (002) Ir and (002) SrTiO₃ reflection regions taken in identical conditions. Linewidths were found by fitting a Gaussian function to data for SrTiO₃ and Ir with values 0.030 ± 0.002 and 0.16 ± 0.01 deg, respectively. The larger Ir linewidth is due to interfacial stress and dislocations. This linewidth is comparable to the previously reported linewidth for evaporated Ir on SrTiO₃ [9,56]

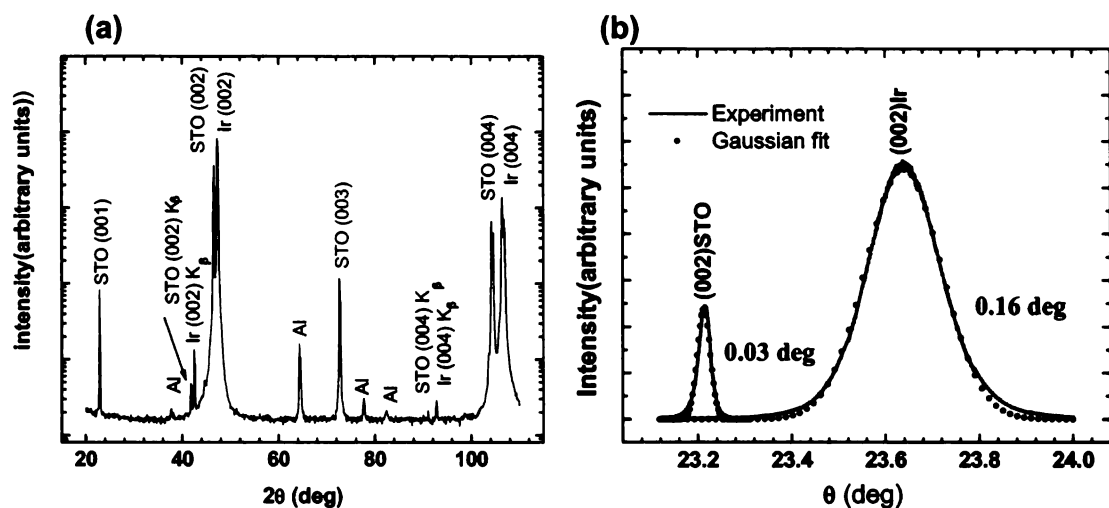


Figure 5.6 (a) θ - 2θ scan of a 600 nm thick Ir film on SrTiO₃ taken using Cu K α radiation. Note the log intensity scale (b) rocking curve of SrTiO₃ and Ir (200) reflections with linewidths 0.03 and 0.16 deg, respectively.

To confirm the in-plane epitaxial relation between Ir and SrTiO₃ a (111) pole-figure, out-of-plane scan of (001) Ir on (001) SrTiO₃ was performed. The substrate was mounted on the Bruker chuck with two lateral sides of the substrate vertical. The χ angle was set to 54.7 deg, the angle between (001) and (111) planes. The detector and the sample were fixed at the (111) reflection position at $2\theta = 40.6$ deg. The crystal was then rotated about the ϕ axis (the axis perpendicular to the (001) plane of the crystal) from 0 to 360 deg to bring a (111) plane to the Bragg condition. Four (111) reflections were observed as shown in Figure 5.7. The Ir and SrTiO₃ (111) reflections occur at the same angles, demonstrating that their $\langle 110 \rangle$ directions are parallel. Thus, the epitaxial relation between Ir and SrTiO₃ can be stated as $(001)_{\text{Ir}} \parallel \langle 110 \rangle_{\text{Ir}} \parallel (001)_{\text{SrTiO}_3} \parallel \langle 110 \rangle_{\text{SrTiO}_3}$.

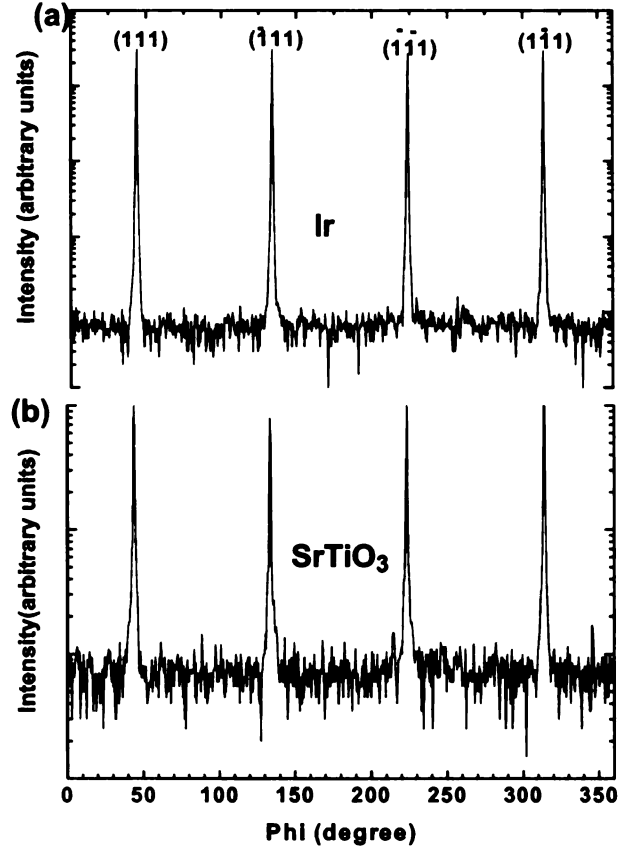


Figure 5.7 X-ray (111) pole figure (a) Ir (b) SrTiO₃. The (111) reflections from Ir and SrTiO₃ are at the same angular positions confirming the in-plane epitaxial relation between the two.

5.3 CVD reactor process

Heteroepitaxial diamond growth was carried out in the microwave plasma CVD reactor shown in Figure 5.8. It is powered by a 2.45 GHz microwave source capable of producing 6 kW. A waveguide connects the source to a cylindrical brass microwave cavity via a tunable electrostatic coupler. The vacuum and gas handling systems include mass flow controllers, a pressure controller, and a turbo-molecular pump backed by a roughing pump. A LabView system monitors biasing current, pressure, and temperature

and controls the process sequences. It shuts the system down if pressure and reflected microwave power exceed limiting values.

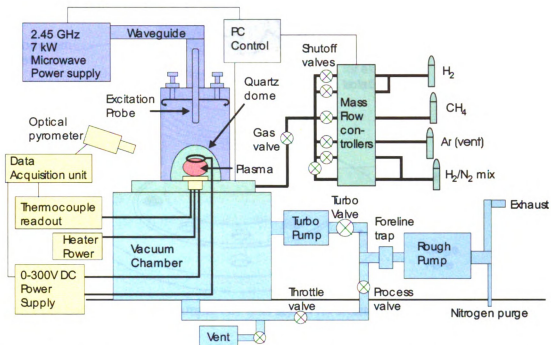


Figure 5.8 General schematic of the microwave plasma CVD reactor used for heteroepitaxial diamond growth [140].

5.3.1 Substrate stage and bias set up

The substrate stage, sample holder, and bias ring, within the CVD reactor, are shown in Figure 5.9. The stainless steel stage is electrically isolated from the lower stage plate by a fused quartz tube. A bias ring is supported above the sample stage assembly by Mo posts. During biasing, the lower part of the stage and the bias ring are grounded, whereas the components in contact with the sample stage can be placed at an arbitrary potential with respect to ground.

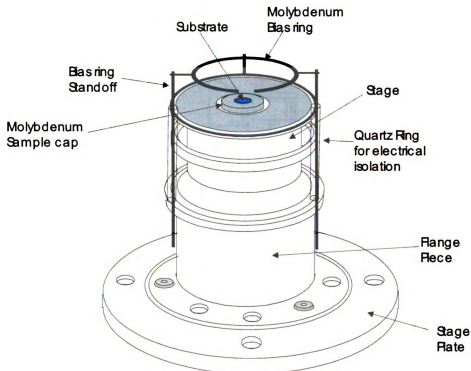


Figure 5.9 Schematic of the sample and bias set up for heteroepitaxial diamond growth

A Kepko DC power supply, 0-300V/0-200mA, generates the bias voltage. Two 50 Ω resistors are connected in series with the power supply, one at the positive and one at the negative terminal. The voltage drop across one of the 50 Ω resistors is measured by a Fluke data logger and used to monitor the bias current. The circuit is shown in Figure 5.10. A circular Mo wire ring is supported by three Mo posts which are grounded at the lower stage assembly. The bias ring is in contact with the microwave plasma and keeps the overall resistance of the bias circuit near 3 k Ω for typical operating conditions.

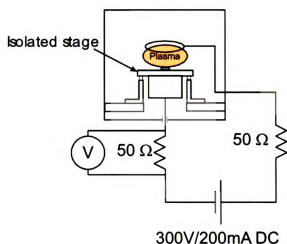
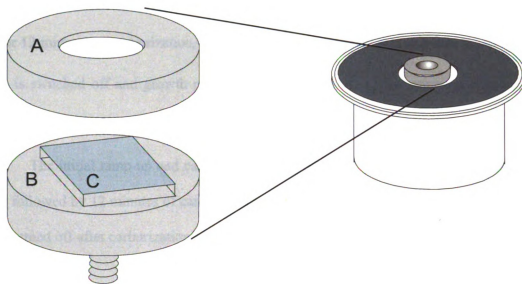


Figure 5.10 Electrical circuit used for biasing.

5.3.2 Substrate holder

The molybdenum substrate holder consists of a post and a cap, shown in Figure 5.11. The post is attached to the sample platform with a threaded rod. The substrate sits on the post and is covered by the cap. The standard design uses a $5 \times 5 \text{ mm}^2$ substrate with 3.5 mm dia circular aperture and 8 mm dia Mo post. To grow diamond on a $5 \times 5 \text{ mm}^2$ square substrate, a 10 mm dia cap is used with $6 \times 6 \text{ mm}^2$ square aperture. The sample is centered on a 9 mm dia post such that the edges have equal gaps. To prepare an 8 mm dia diamond sample on a $10 \times 10 \text{ mm}^2$ substrate, a 14 mm dia Mo post with a 15 mm dia cap having a 8.5 mm dia aperture is used.



- A. Mo cap
- B. Mo post
- C. Ir/oxide substrate

Figure 5.11 Schematic of sample post and cap with sample stage

5.4 Diamond nucleation

5.4.1 The bias process

To induce diamond nucleation on Ir, a negative bias voltage is applied to the substrate in the presence of the microwave plasma. The variables explored were: bias voltage V_b (fixed at -150V here), bias duration t_b , substrate temperature T_s (fixed here), methane concentration r (fixed here) and the geometry (fixed here). The diamond nucleation (and growth) process sequence is shown in Figure 5.12. To begin, pure hydrogen is introduced into the reactor bell jar and, at 10 Torr pressure, a plasma ignites at 700 W incident microwave power. At 15 Torr, the incident microwave power is increased to 1100 W. The sample temperature T_s increases rapidly and after 6 minutes reaches about 650 °C, where the pyrometer begins to register. Then, methane is

introduced and allowed to react with the sample; this step is referred to as carburization. After 12 minutes of carburization, the bias voltage is switched on for a time t_b . At t_b , the bias is switched off and growth proceeds for a time t_g . At t_g , the microwave power is turned off and gases are pumped out of the system.

The initial ramp-up and carburization time were not varied: 6 minutes of heating was followed by 12 minutes of carburization. For the zero-min biased sample, the plasma was turned off after carburization without turning on the bias voltage

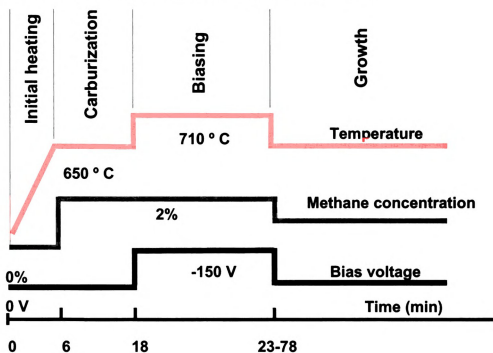


Figure 5.12 Time plot of the process sequence used in studies of diamond nucleation and growth

Throughout the process, heating of the sample occurred only by contact with the plasma; no external heater was used. In some cases, the bias and growth processes utilized pressures and methane concentrations that slightly varied from the aforementioned processing steps.

Two sets of experiments were carried out to understand the effect of the bias time duration t_b , on Ir morphology, nucleation rate, density and spatial distribution of nuclei.

Another experiment examined the effects of varying t_g , the growth time, at fixed t_b .

- In the first series of experiments, t_b was varied from 0 to 60 min, followed by abrupt turn-off of the microwave plasma and bias to minimize diamond growth after biasing. These runs are referred to as 0^+ growth runs, since cooling is not instantaneous and some growth may occur. The main goal of this part of the study was to observe how the Ir surface evolves after it interacts with the plasma for different times.
- In the second series of experiments, t_b was again varied. At t_b the bias voltage was switched off, but then followed by 20 minutes of growth. The finite growth period allowed diamond nuclei to grow to a size that could be imaged by SEM. This allowed us to estimate the density and distribution of the nuclei.
- In the third series, t_b was fixed at 60 min but the growth time was varied from 7 to 150 s. The reason for these experiments was to observe the early stages of diamond growth and coalescence.

The diagnostics used were AFM and SEM. We also have used HRTEM on thin sectioned samples to study the diamond-Ir interface.

5.4.1.1 0^+ growth experiments

In this series, t_b was varied from 0 to 60 min then the plasma quickly turned off. Figure 5.13(a) shows an AFM image for $t_b = 0$ min, i.e., a carburized sample. It cannot be

distinguished from the as-grown Ir surface, Figure 5.4. The Ir domain structures are similar. It should be noted that the domains are not evident by SEM, i.e., the Ir domains do not produce electron contrast. Average roughness (R_a) measured over an area $1 \times 1 \mu\text{m}^2$ was 0.4 nm, comparable to 0.3 nm for fresh Ir. Thus, carburization has little effect on the Ir surface.

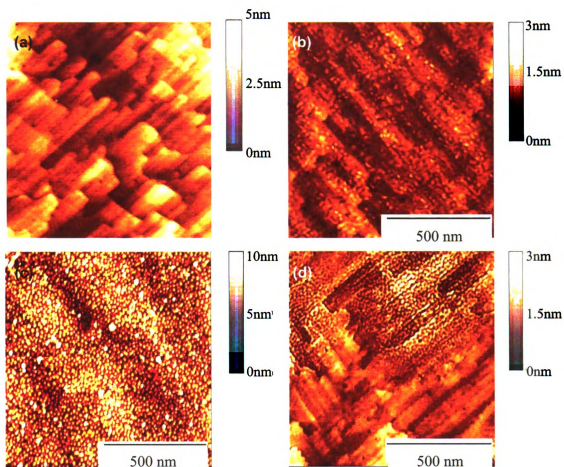


Figure 5.13 AFM images of the Ir surface after different biasing times (a) $t_b = 0$ min. little change is seen from the as-prepared surface. (b) $t_b = 5$ min, the surface is covered with dots and chain like structures. (c) $t_b = 20$ min, middle, the Ir surface is covered by dots separated by a mean nearest neighbor distance of 15 nm. About 1 % of the dots are 4-5 nm taller than average height. (d) $t_b = 20$ min, edge a two phase region appears. The upper part of the image shows chain-like structures with mean distance between the chains 15 nm. The lower part of the image has no chains or dots but the step edges are corrugated on a scale of 15 nm.

Figure 5.13(b) shows an AFM image for $t_b = 5$ min, taken in the middle of the Ir/oxide substrate. In contrast to (a), the surface is now covered by small round dots. They are preferentially aligned along the [110] Ir step edges. In some regions, instead of dots, elongated islands connect to each other to form a chain-like structure. The large-scale structure of the Ir step edges is still visible.

Figure 5.13(c) shows an AFM image for $t_b = 20$ min taken at the middle of the substrate. Now, the step edges are nearly erased and the surface is covered with dots, separated by 15 nm on average. The dot density is $\sim 10^{12}$ cm⁻². The white dots are about 4-5 nm taller than the typical dot, with density $\sim 10^{10}$ cm⁻². Since the AFM image is formed by the convolution of the tip and dot shapes, the dots are actually smaller than they appear in the images.

The previous images were taken at the middle of the substrate. However, when the edges of the sample were examined, a significant difference in topography was seen. Figure 5.13(d) shows an AFM image taken near the edge of the biased region of the sample where a two-phase topography occurs. In the upper part of the image, elongated dot-like structures connect to form [110] chains, similar to, but more distinct than, the $t_b = 5$ min sample, Figure 5.13(b). The mean inter-chain distance is 15 nm, the same as the mean distance between nearest neighbor dots in the middle of the sample. The surface in the lower part of figure 5.13(d) is not decorated with chains, but is similar to the $t_b = 0$ min sample. The Ir step edges show corrugated structures, separated by a mean distance of 15 nm, the same as the mean distance between nearest neighbor dots at the middle, or the mean inter-chain distance in the decorated regions at the edge.

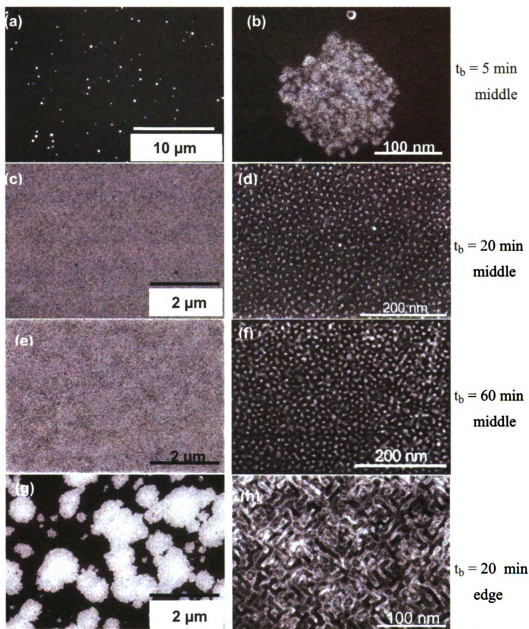


Figure 5.14 SEM images of the Ir surface after biasing for different durations. (a) $t_b = 5$ min; a few bright patches on the surface have appeared (b) magnified image of one of the bright patches shows internal structure (c) $t_b = 20$ min; sample middle shows uniform contrast (d) magnified image of (c) shows the surface to be covered by dots with 15 nm mean separation (e) $t_b = 60$ min; sample middle shows uniform contrast (f) Magnified image of (e) shows the surface covered by dots as in (d), with same separation (g) $t_b = 20$ min; sample edge shows isolated bright patches on μm scale. (h) Magnified image of the bright island shows structures similar to the chains observed in AFM image in Figure 5.18(d)

The chain-covered region is about 1-2 nm higher than the smooth region, and the chains are also 1-2 nm higher than their surroundings. These observations suggest that biasing initially leads to etching of Ir step edges in the higher regions of the substrate, creating chains, which then break up into dots under prolonged exposure to the plasma.

Figure 5.14 shows SEM images of samples produced with different bias durations, which varied from 5 to 60 minutes. Figure 5.14(a) shows an SEM image for $t_b = 5$ min at the middle of the sample. Small bright patches are observed on the surface of the entire sample. Figure 5.14(b) shows the magnified image of one of the bright patches seen in (a), which shows some internal structure.

Figure 5.14(c) shows the middle region of the $t_b = 20$ min sample. At this scale, the surface appears uniform, with little structure discernable. The magnified image of this region, Figure 5.14(d), shows, however, that the surface is covered by dots with 15 nm mean nearest-neighbor spacing. Both AFM, Figure 5.13(c), and SEM provide images of the same dot distribution.

Figure 5.14(e) shows the middle of a $t_b = 60$ min sample. This image is similar to (c), the $t_b = 20$ min sample. In 5.14(f), the magnified image from (e) shows a surface covered by dots with 15 nm mean nearest neighbor spacing. Samples produced within a $t_b = 20$ -80 min window show similar morphology.

Figure 5.14(g) shows an image taken near the edge of the biased region for $t_b = 20$ min. This image shows bright isolated islands on the scale of μm . Their contrast seems to be similar to that of the bright patches observed for $t_b = 5$ min as shown in Figure 5.14(a). Figure 5.14(f) shows the internal structure of the bright islands. The morphology is

similar to the chain structures observed in the AFM image shown in the upper region of Figure 5.13(d). The agreement between the AFM and the SEM images suggests that SEM contrast arises from topographical differences, i.e., the bright islands seen in the SEM image are locally high regions, and not from chemical differences. Since the undecorated regions here are similar to the 0^+ min biased sample, it suggests that these regions are etched less during the biasing. The etching of the Ir is thus not spatially uniform. Etching starts at locally high regions then propagates across the surface.

After 5 minutes of biasing, it is observed that the secondary plasma, initially centered over the circular cap, has become brighter at the middle of the sample. Because of this higher secondary plasma density, the middle of the sample now etches faster than the edges. As the biasing progresses, the secondary plasma gradually moves toward the edge of the sample, increasing the etching rate there. This creates the difference in surface topography seen, for example, at the middle and edge of the $t_b = 20$ min sample. Thus, the region at the edge is etched for an effectively shorter time than at the middle. We infer that the edge regions are then similar to the central regions at an earlier time of the biasing period.

HRTEM imaging was used to study the diamond-Ir interface on a scale as small as 0.1 nm. This technique requires the preparation of thin sections perpendicular to the interface using mechanical and ion milling. To protect the surface, an adhesive of Pt nano-particles mixed with epoxy was deposited on the surface. This glue appears in the HRTEM images and must be distinguished from the diamond-Ir sample.

Figure 5.15(a) shows a cross-sectional HRTEM image of the diamond-Ir interface for $t_b = 10$ min and $t_g = 20$ min. Of interest here is the structure of the Ir. The Ir surface

has faceted pillars with mean nearest neighbor spacing 15 ± 0.5 nm. These pillars are clearly the dots observed in AFM and SEM. Lateral sizes of the pillars, measured at the middle, vary from 5 to 12 nm, with a mean of 10 ± 0.5 nm. The mean height of the pillar is 4 ± 0.5 nm. The dimensions and the errors are calculated from the HRTEM images shown here.

Figure 5.15(b) shows an HRTEM image for $t_b = 60$ min and $t_g = 0$ min. The Ir shows faceted pillars with a mean spacing 14.6 ± 0.5 nm. Sizes of the pillars vary from 5 to 10 nm with an average of 8 ± 0.5 nm. The mean height of the pillar is 4.5 ± 0.5 nm. This may be evidence that a longer t_b leads to a slightly smaller pillar width. The results for the pillar spacings are consistent with AFM and SEM.

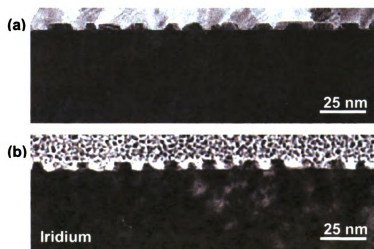


Figure 5.15 (a) HRTEM images of the Ir surface with (a) $t_b = 10$ min, $t_g = 20$ min (b) $t_b = 60$, $t_g = 0$ min [154].

5.4.1.2 20 minutes growth after biasing

We now discuss experiments with variable t_b followed by $t_g = 20$ min. SEM images taken at the middle of $t_b = 5$, 10 min and at the middle and edge of $t_b = 20$ min

diamond films are discussed. This yields the spatial distribution of diamond on the Ir surface for different t_b , whose precursor is the distribution of diamond nucleation sites.

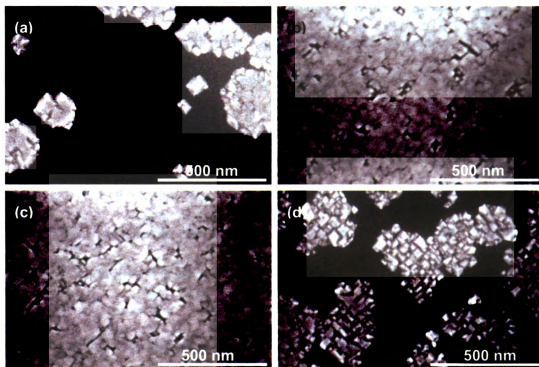


Figure 5.16 SEM images of samples with different t_b followed by $t_g = 20$ min (a) $t_b = 5$ min; film shows sparse diamond crystallites (b) $t_b = 10$ min, middle; film is mostly covered by epitaxial diamond except for some coalescence boundaries. (c) $t_b = 20$ min, middle; film is similar to (c) with better coalescence (d) $t_b = 20$ min, edge; sample shows diamond growth in μm size isolated islands

For $t_b = 5$ min and $t_g = 20$ min, the surface in the middle has a relative coverage of about 20% epitaxial diamond, Figure 5.16(a). When the bias time is lengthened, for $t_b = 10$ or 20 min, epitaxial diamond crystallites have grown and coalesced over most of the surface with a relative coverage of over 90%. Some coalescence boundaries can be seen in Figure 5.16(b) and (c), respectively. In contrast to the middle region, for $t_b = 20$ min, diamond grew as isolated islands at the edge of the film, Figure 5.16(d). These islands

apparently correspond to the bright areas seen in SEM after $t_b = 20$ min and $t_g = 0^+$, Figure 5.14(g), since the areal coverage in both figures is about the same. These results indicate that the etched regions provide the conditions for diamond nucleation. It is noted, however, that the etched structures in Figure 5.14(d) and (f) lead to well-coalesced diamond, whereas the structures in Figure 5.14(h) yields islands of diamond with fine inter-granular boundaries for equivalent growth time.

Figure 5.17 combines these results in a plot of diamond areal coverage vs. radial distance from the edge of the sample. The growth region is 3.5 mm dia on a 5 x 5 mm² substrate. Each point in the plot is derived from a separate SEM image. The Image J package [155] was used to analyze the areal coverage of 20 x 25 μm^2 SEM images. Since the analysis was made from an image with low magnification where the coalescence boundaries were not visible, the calculated value of the areal coverage is an overestimate. For example, using SEM image in Figure 5.16(b), the areal coverage is 96 %. With the lower magnification image, where the boundaries are not visible, the coverage is 100 %. For $t_b = 5$ min, only 20 % of the surface is covered by diamond at the middle. For $t_b = 10$ min, most of the sample is covered with epitaxial diamond except for a narrow band near the edge. Increasing t_b to 20 or 60 min increased the coverage at the edges. These results suggest that the modification of the Ir surface due to the biasing starts from the middle and propagates toward the edge.

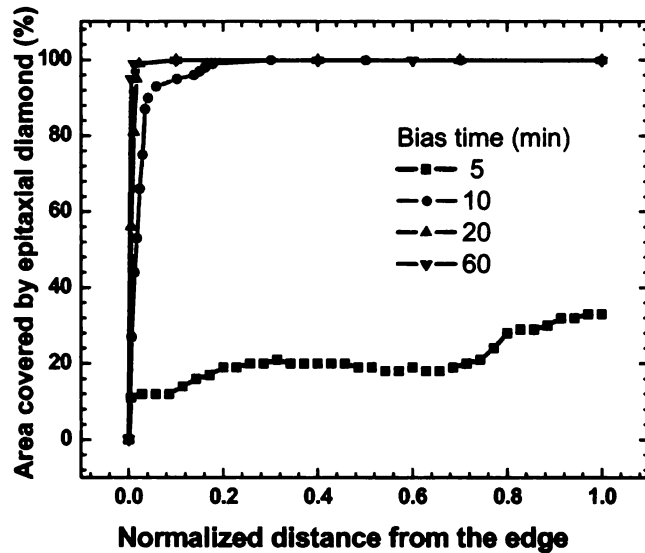


Figure 5.17 Plot showing % area covered by epitaxial diamond as a function of distance measured from the edge of the film for different biasing time. Higher biasing time increased the area covered by diamond at the edge.

5.4.1.3 60 minutes biasing followed by short growth

We now describe the experiments with $t_b = 60$ min in which t_g varied from 7 to 150 s, Figure 5.18(a) to (f). Here, we expect the Ir surface to be fairly uniformly covered with dots after bias. As shown in Figure 5.18(a), after $t_g = 7$ s Ir dots continue to be clearly visible. Note the simultaneous presence of diffuse patches. As the growth time increases, the dots become less visible and the cloudy, diffuse regions become more prominent and compact. For $t_g > 60$ s, the small, bright regions have become evident. Two reasons for the enhanced brightness are: more efficient emission of secondary electrons arising from the topography, or the large secondary yield of hydrogenated diamond, a consequence of its negative electron affinity. Since HRTEM images showed

that the topography of the Ir surface is invariant during growth, we ascribe the changing contrast after 60 s to the growth of diamond regions.

The interfaces between diamond clusters preferentially align along [110]. Although initially ascribed to faceting, it now seems likely to occur because diamond grows laterally in the channels between the dots, assuming that diamond nucleates in the channels but not on the top of the dots. The density of the bright regions in Figure 5.18(d) is $\sim 2 \times 10^{11} \text{ cm}^{-2}$, which is somewhat lower than the dot density. If there is little coalescence at this point, each region originates from a single diamond nucleus. This number may yield a more reliable estimate of the nucleation density. After 120 s, the bright regions have grown larger, yet many small dots are still visible. These could be the underlying Ir dots or correspond to freshly nucleated regions. The image in Figure 5.18(f) shows more compact bright regions than in Figure 5.18(e), although growth is somewhat longer; this could be due to sample to sample variation.

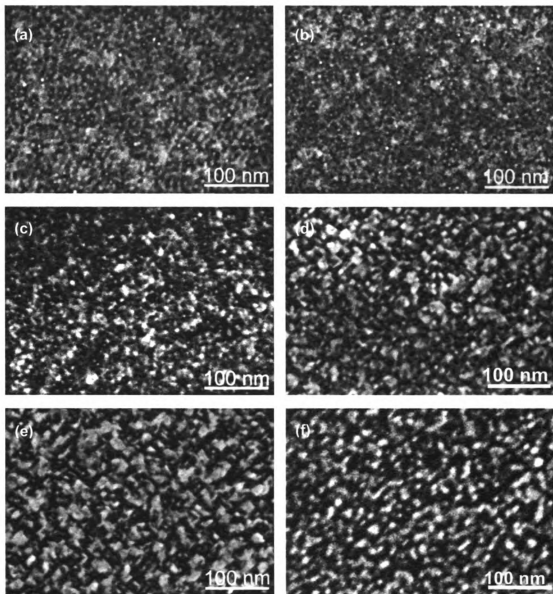


Figure 5.18 SEM images of 60 min biased samples followed by short growth (a) 7 s (b) 30 s (c) 60 s (d) 90 s (e) 120 s (f) 150s. Each image is from a different sample.

5.4.1.4 HRTEM study of the diamond-Ir interface

Here we discuss the results of HRTEM studies for samples with $t_b = 60$ min followed by $t_g = 0$ to 150 s. HRTEM images are formed by electrons transmitted through the crystal lattice. Contrast depends on the atomic number (Z) of the specimen, its

thickness, and the crystallographic orientation of the sample with respect to the incident electron beam. Specimens with larger Z scatter electrons better, producing higher contrast; however, thicker specimens absorb more electrons, producing lower contrast. Because of the ensuing large dynamic range, imaging of diamond and Ir simultaneously is difficult. Strain at the interface will also change the contrast.

Figure 5.19 [154] shows an HRTEM image for a $t_b = 60$, $t_g = 0$ min sample. The (110) plane is perpendicular to the incident beam. Ir pillars and (111) lattice planes can be seen. The lattice planes of the pillars and substrate are continuous, both of which exhibit the Ir (111) interplanar spacing, 0.222 nm. This confirms that Ir is etched by the bias process, leaving dots or pillars, with little deformation of the Ir lattice. No features are observed here that can be associated with diamond nuclei or crystals. The crystalline structures seen in some places above the Ir pillars are Pt nanoparticles embedded in an amorphous epoxy matrix used for specimen preparation. The bright region in the channels between the pillars, which is not Pt or epoxy, could arise from carbon deposited during the biasing, as previously reported [95,156].



Figure 5.19 HRTEM image of Ir surface for a $t_b = 60$ min, $t_g = 0$ min sample showing the Ir pillars [154].

Figure 5.20(a) shows a HRTEM image for $t_b = 60$ min and $t_g = 90$ s. Ir pillars can be seen, comparable in size and distribution to the $t_b = 60$ min and $t_g = 0$ min sample, discussed earlier. Here, the interfacial carbon layer is more clearly seen.

Figure 5.20(b) shows a magnified region from (a). Although diamond crystallites are not resolved in (a), here, two diamond crystallites can be seen in the channels between the pillars. The (111) interplanar spacing for Ir and diamond are 0.222 and 0.206 nm, respectively. Owing to the lattice mismatch, the planes cannot be aligned everywhere at the interface, and misfit dislocations occur. With a mismatch of 7.5 %, there should be misfit dislocations with an average period of 13-14 lattice spacings if the dislocation Burgers vector is inter plane spacing. The distance of the misfit dislocations from the interface is determined by a balance between the pseudomorphic interfacial strain energy and the energy of dislocation formation [157]. Elasticity theory predicts that the critical length for misfit dislocation formation should be 0.2-0.3 nm from the Ir-diamond interface. The HRTEM observations are consistent with the theory.

Misfit dislocations are clearly visible at the Ir-diamond interface shown in Fig. 5.20(b). No intervening phase can be seen between diamond and Ir, which means that diamond has directly nucleated on the Ir surface. No particles are observed on top of the diamond crystallites, other than the amorphous carbon layer deposited during biasing. The larger diamond crystallite is about 5 nm by 4 nm and the smaller crystallite about 3 by 3 nm. In figure 5.20(c), blue lines are drawn to show the corresponding (111) Ir and diamond lattice planes. A misfit dislocation is evident in the middle of the particle. Diamond crystallites of this size were only observed in the channels between Ir pillars or

on the sides of the pillars in images of this sample. Blue lines indicate corresponding Ir and diamond (111) planes

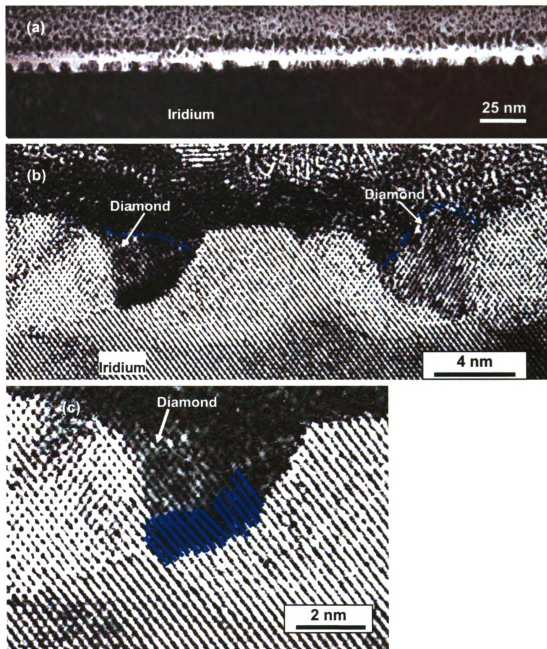


Figure 5.20 Cross section HRTEM images for a $t_b = 60$ min, $t_g = 90$ s sample. (a) Carbon-Ir interface showing a bright layer, possibly amorphous carbon. (b) Two diamond crystallites in the channels between the Ir pillars. (c) Misfit dislocation at the diamond-Ir interface [154].

Isolated diamond crystallites were not observed on the top (001) Ir surfaces. This observation lends credence to the idea that etching of the Ir surface generates nucleation sites that are absent on Ir (001).

Figure 5.21 [154] shows a high-resolution image of the diamond-Ir interface for a $t_b = 60$ and $t_g = 150$ s sample. For this slightly longer growth time, a diamond crystallite has now overgrown the top of an Ir pillar. The blue lines indicate the top boundary of the diamond crystallite, whose size is about 15 nm laterally and extends 3-4 nm above the Ir pillar. Two blue arrows show the positions of misfit dislocations about 14 lattice spacings apart. The Ir lattice is distorted close to the dislocation core due to the large local stress. Since there is no slip apparent at the interface, it suggests strong bonding between Ir and diamond.

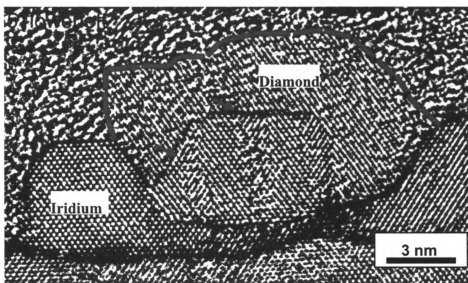


Figure 5.21 HRTEM image for $t_b = 60$ min, $t_g = 150$ s sample. This image shows a diamond crystallite over-growing on top of an iridium pillar. Blue line shows the top boundary of the diamond crystallite. Blue arrows show the positions of misfit dislocations [154].

Figure 5.22 [154] is an HRTEM image for a $t_b = 10$ and $t_g = 20$ min sample. This image shows the diamond-Ir interface after longer growth. Faceted Ir pillars are visible with typical spacing. Bright lines, which appear to radiate from the Ir pillars, are observed. Some of these features, at a 60 deg angle from the surface, are most likely twin boundaries. They may arise from different nucleation conditions on the opposite sides of an Ir pillar or may originate at imperfections on the Ir surface.

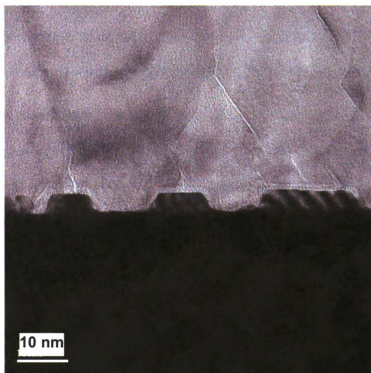


Figure 5.22 HRTEM image of a $t_b = 10$ min and $t_g = 20$ min sample [154].

5.4.2 Discussion

The previous sections have explored the role of the bias process in modifying the Ir surface. Under appropriate conditions, relatively dense, uniform, and highly correlated Ir pillars are created. Subsequently, diamond nucleates and grows to cover most of the Ir surface in about 20 min in the CVD reactor.

Under bias, ion bombardment etches the Ir surface initially along [110] step edges, as suggested by AFM images. If the secondary plasma moves to the center of the sample, strong etching of the Ir surface starts there after about 5 min, gradually expanding outward, reaching the edges in another 5 min or so. The initial 5 min may be associated with the time for the secondary plasma to move from the cap, where it first forms, to the middle of the sample. A time-dependent secondary plasma front explains how the etched structures at the sample center and edges are related: the edges are simply etched for a shorter time, since the etching begins at the center. The movement of the biasing front has been reported previously, for DC biased silicon [80,158]

We have also inferred that the etching of the Ir surface may be sensitive to the height fluctuations of the surface. Higher regions are etched faster, possibly because of the higher electric field at discontinuities or the higher temperatures closer to the plasma. These effects can create the two-phase region, seen near the sample edges. At the middle, the two-phase region is unlikely to persist more very long, owing to the faster etch rate.

The large increase in nucleation density that occurs after 5 min of bias suggests a non-linear process. During the period from 5 to 10 min after the start of bias, the area covered by diamond increased from 20 to 100 % in the middle and 15 to 20 % in the edge of the sample. Again we infer that this reflects the dynamics of the secondary plasma as it moves across the sample.

It has been proposed that Ir is sputtered during biasing, then redeposited, and could be responsible for the Ir dots on the Ir surface [94]. However, if this were true, the Ir particles would be randomly distributed on the surface and would not be expected to self-organize. Also the surface would become more deeply etched as time progressed, in

contrast to the observations. The 15 nm length scale is apparently imprinted on the Ir surface shortly after 5 min bias, and varies little for bias times up to 80 min.

The bias process not only etches the Ir surface, but leaves a small amount of amorphous carbon on Ir. XPS and XPD measurements estimated about 20 monolayers of carbon after 60 min bias [91,92]. This carbon layer may serve a number of roles during biasing and nucleation. As observed by HRTEM, the lateral size of the Ir pillars is slightly larger for $t_b = 10$ min than for $t_b = 60$ min. However, in both cases the height and the nearest neighbor spacing are comparable. This suggests that as biasing progresses only the side walls of the Ir pillars are etched away. Two ideas may explain this selectivity. As the pillared landscape is created, the biasing front may propagate to the topographically higher un-etched regions. In addition, the deposited carbon layer may protect the Ir from further etching.

If the carbon deposited during the biasing is predominantly sp^3 bonded, it may serve as a precursor for diamond nucleation. Since tetrahedral amorphous carbon (ta-C) is structurally close to crystalline diamond, only a small energy barrier separates the two phases. The barrier could be overcome when a thermal spike is created when energy is dissipated in the Ir lattice by a hydrocarbon ion extracted from the plasma. Once a stable diamond nucleus is created, any nearby ta-C would readily transform to diamond, enhancing the growth of the diamond cluster.

From the HRTEM images presently available, diamond appears to nucleate preferentially between, or on the sides, of the Ir pillars. No image shows nucleation on the top (001) surface. Therefore a function of the bias process may be the creation of nucleation sites

on higher index planes or at special step edges. Alternatively, if the nucleation process is due to ion subplantation, subplanted regions would need to organize into channels, leaving intact Ir pillars. Subplantation models may invoke carbon saturation of the sub-surface region during the bias process. Within the subplanted region, diamond nuclei may form, effectively at high pressure due to confinement in the substrate. Subsequently, the substrate surface is etched away, leaving the diamond nucleus [73]. This model is consistent with observation, although it cannot be proven. Another possibility is that ion bombardment leads to demethylation reactions and formation of special compounds at the interface, i.e., an Ir hydrocarbide [159] as opposed to a monatomic ta-C layer. This material could act to enhance nucleation or could serve as a protective layer to prevent erosion of the Ir. At this time, no evidence exists that supports the presence of a chemical species at the interface other than carbon.

XPD measurements have shown the presence of crystalline, epitaxial diamond on the Ir surface after $t_b = 60$ min and zero growth, but HRTEM does not reveal any diamond nuclei [92]. The XPD result is not necessarily incompatible with our observations, since the size of the nuclei may be too small at that stage to be resolved by electron microscopy.

From the SEM images after 150s growth and the HRTEM images after 90s growth, it seems that the nucleation density must be less than the density of the Ir pillars, which is $\sim 3 \times 10^{11} \text{ cm}^{-2}$. However, the HRTEM image region is a slice that cannot reveal the 3-D environment of a pillar. Thus there may be additional diamond crystallites that are not visible, leading to an underestimate of the nucleation density.

HRTEM images have reinforced x-ray data for the specific epitaxial relation between diamond and Ir. The presence of the misfit dislocations at the diamond-Ir interface confirms that diamond growth is not pseudomorphic. The critical distance for misfit dislocation from the interface based on elasticity theory, which predicts 0.2 nm as the critical distance, is in accordance with our observations.

5.4.3 Summary

Based on the findings presented in this section, we propose the following scenario for the nucleation and the growth of diamond on Ir.

1. During biasing, ion bombardment etches the Ir surface creating first chains, then pillared structures.
2. Strong etching begins at the center of the sample then propagates to its edges. The dynamics are controlled by movement of the secondary plasma. This explains the temporal and spatial patterns that are observed.
3. Diamond nucleation does not occur during biasing because of intense ion bombardment. Nucleation is triggered at the end of the bias step.
4. Growth is largely determined by transport from the vapor phase. Epitaxial crystallites start coalescing with one another after only 90 s of growth.

5.5 *Diamond thin film growth*

In this section we describe processes for producing diamond thin films. These studies led to a focus on the role of sample holder geometry.

Typical growth conditions needed to produce a 500-600 nm diamond film, grown over a 3.5 mm dia region on a 5 x 5 mm² Ir/oxide substrate, are given in Table 5.1. The variables are bias voltage V_b , bias ring height h_b , bias current I_b , methane to hydrogen ratio r , incident microwave power P_i and growth pressure p .

Table 5.1 Growth conditions for 3.5 mm dia diamond film on 5 x 5 mm² Ir/oxide substrate

	Time (min)	P_i (W)	T (°C)	p (Torr)	V_b (V)	I_b (mA)	r (%)	h_b (mm)
heating	6	0-1100	25-660	0-18	0	0	0	32
carburization	12	1100	660	18	0	0	2	32
biasing	60	1100	710	18	-150	30-40	2	32
growth	180	1100	670	18	0	0	1	32

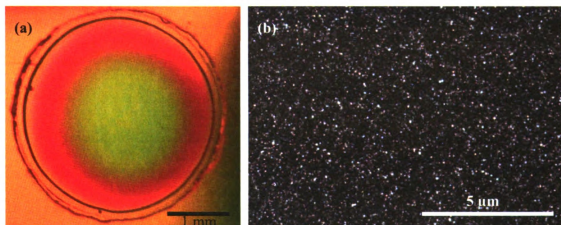


Figure 5.23 (a) DIC micrograph and SEM image of a 3.5 mm dia diamond film. (a) DIC micrograph, the circular band at the edge of the film is the region below the cap. Asymmetry in the left and right side of micrograph is due to sample tilt (b) SEM image of the same film at its center. Bright white dots are locally high regions. Diamond crystallites have undergone complete coalescence.

A typical maximum thickness at the middle of a diamond film grown under these conditions with $t_g = 3$ h is about 550 nm. A DIC micrograph of such a film is shown in Figure 5.23(a). The diamond film is transparent, so that interference occurs between the light rays reflected from the front and the back surface of the film. The color differences

seen in the diamond film are interference fringes, arising from thickness variations across the film. The thickness variation from the middle to edge of the film is estimated to be 150 nm.

Figure 5.23(b) shows an SEM image of the same film taken at the center. Diamond crystallites have already coalesced with each other. No coalescence boundaries, voids or bare regions can be seen. The small bright regions arise from small height fluctuations on the surface.

Now we discuss growth in a square geometry with a $5 \times 5 \text{ mm}^2$ Ir/oxide substrate. A different Mo cap and post were used. The height of the bias ring above the substrate was found to influence the formation of the pillared Ir surface. As the bias ring is moved closer to the surface it flattens the plasma, increasing the uniformity of the plasma over a larger area.

Typical growth conditions for this geometry are given in Table 5.2. Bias current increased from 40 to 50 mA at a bias voltage of -150 V. Growth temperature was 780 °C, 10 °C higher than for the smaller area diamond film.

Table 5.2 Growth conditions for $5 \times 5 \text{ mm}^2$ diamond film on $5 \times 5 \text{ mm}^2$ Ir/oxide substrate.

	Time (min)	P _i (W)	T(°C)	P (Torr)	V _b (V)	I _b (mA)	r (%)	h _b (mm)
heating	6	0-1100	25-660	0-18	0	0	0	25
carburization	12	1100	660	18	0	0	2	25
biasing	60	1100	715	18	-150	40-50	2	25
growth	180	1100	680	18	0	0	1	25

Figure 5.24 (a) shows a DIC micrograph of the overall diamond film on a Ir/SrTiO₃ substrate. Diamond has grown to the edges without any voids. An SEM image

taken at film center is shown in figure 5.24(b), which is similar to the image in Figure 5.23(b) for the smaller film. Thickness variation, estimated from the number of interference fringes, is about 350 nm.

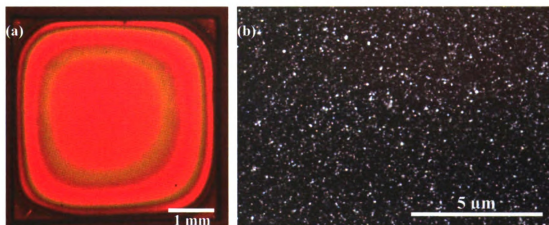


Figure 5.24 DIC micrograph and SEM image of a $5 \times 5 \text{ mm}^2$, 3 hour diamond film. (a) The color bands are due to film thickness variation. (b) SEM image of the same film taken at the middle. Diamond crystallites are completely coalesced. Bright dots are due to the local height variation of the film.

Diamond was also grown over an 8 mm dia region on $10 \times 10 \text{ mm}^2$ Ir/SrTiO₃ substrates. The substrate was supported by a 14 mm dia Mo post. A Mo cap, 15 mm dia with an 8.5 mm aperture covered the substrate. The bias ring height and bias voltage are listed in Table 5.3, which shows process parameters. The increased lateral extent of the plasma led to better nucleation uniformity over the 8 mm region.

Table 5.3 Growth conditions for 8mm dia diamond on $10 \times 10 \text{ mm}^2$ Ir/STO substrate

	Time (min)	P _i (W)	T (°C)	p (Torr)	V _b (V)	I _b (mA)	r (%)	h _b (mm)
heating	6	0-1100	25-660	0-18	0	0	0	13
carburization	12	1100	660	18	0	0	2	13
biasing	60	1100	710	18	-200	120-150	2	13
growth	180	1100	670	18	0	0	1	13

Figure 5.25(a) shows a DIC micrograph of a diamond film grown under these conditions. It has grown without any apparent voids and with high uniformity near the center. The thickness variation is about 250 nm across the film, less than for the smaller film. Figure 5.25(b) shows an SEM image taken near the middle of the film. The microstructure is similar to the films shown in Figs 5.23(b) or 5.24(b) except that a few coalescence boundaries are now visible.

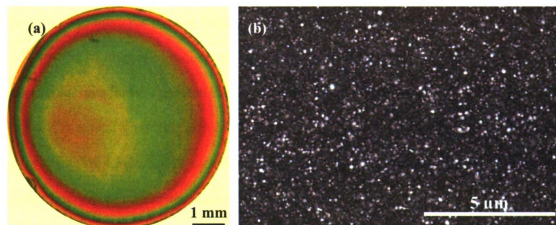


Figure 5.25 DIC micrograph and SEM image of a 8mm dia, 3 hour diamond film. (a) DIC micrograph. (b) SEM image of the same diamond film shows the diamond crystallites coalescing to each other. Residual coalescence boundary can be seen

5.6 Diamond thick film growth

To grow thicker films, a two-step process was used. In the first step, diamond was grown for 3 h in the heteroepitaxial CVD reactor under the conditions described above. In the second step, the film on its substrate was transferred to an AsTeX CVD reactor. Here, process conditions appropriate for homoepitaxial growth were used, as discussed in Ch. 6. When diamond is grown in the heteroepitaxial reactor, no substrate cooling is available so that the microwave power and growth pressure must be low to maintain the correct temperature. Diamond growth under these conditions also requires methane to

hydrogen ratios at or below 1% to suppress growth of nonepitaxial diamond hillocks. The typical growth rate is $0.5\mu\text{m/h}$. Furthermore, the diamond film may shatter during cooling, due to differential thermal contraction. For homoepitaxial growth, using a cooled substrate stage, growth rates of $5\mu\text{m/h}$ were achieved.

A $5 \times 5 \text{ mm}^2$ diamond film grown on SrTiO_3 for 3 hours with the heteroepitaxial reactor was first cleaned by etching in a pure hydrogen plasma in the AsTeX reactor. Process conditions for etching (and growth) are shown in Table 5.4. Figure 5.26 (a) and (b) show SEM images of a diamond film before and after hydrogen etching. Square and rectangular pits have appeared on the surface with sides aligned along $[110]$. After etching, diamond growth proceeded under the conditions in Table 5.4. For this film a growth rate of $4.3\mu\text{m/h}$ was measured. The higher growth rate is a consequence of the higher microwave power density and methane concentration.

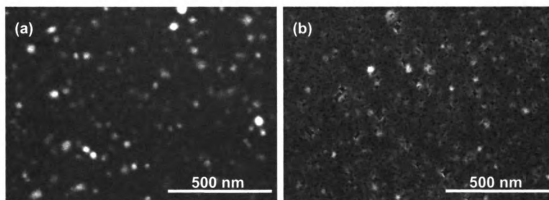


Figure 5.26 SEM image of a heteroepitaxial diamond film (a) before hydrogen plasma etching (b) after hydrogen plasma etching for 15 min.

Table 5.4 Growth conditions of heteroepitaxial diamond film in high growth rate conditions.

	P (W)	p (Torr)	T (°C)	Time (h)	r (%)
H₂ etching	800	150	770	0.25	0
growth	800	150	770	3	7

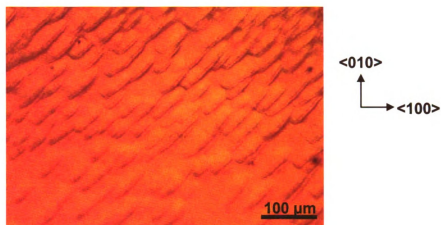


Figure 5.27 DIC optical micrograph of a diamond film after 3 h growth under high rate conditions. Macroscopic steps cover the growth surface.

A DIC micrograph of a diamond film grown for 3 h in each stage of the two-step process is shown in Figure 5.27. The film is a single crystal, but steps of macroscopic height and extent are aligned along $[110]$. This $5 \times 5 \text{ mm}^2$ diamond film cracked and detached from the SrTiO_3 substrate during growth. The film surface was slightly curved because interfacial stress between the diamond and the underlying substrate led to bowing.

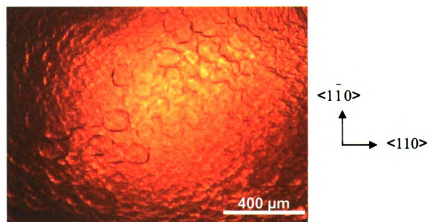


Figure 5.28 DIC micrograph of a $65 \mu\text{m}$ thick heteroepitaxial diamond on Ir. Steps are observed on the surface. Sample is slightly curved due to stress.

A part of the detached film with Ir remaining intact on the back surface was grown for an additional 12 hours. Figure 5.28 shows a DIC micrograph; again macrosteps are observed. The film thickness was 65 μm and its area 1.5 x 3 mm^2 .

The two-step process always concluded with the substrate cracking. It was noticed that after diamond growth the SrTiO_3 turned black. Also, an intact substrate would break during cool down to room temperature even after growth for short times. This stress-induced cracking can occur for several reasons. Owing to the different coefficients of thermal expansion of diamond, Ir and SrTiO_3 , 1.5×10^{-6} , 6.8×10^{-6} and $10.3 \times 10^{-6} \text{ K}^{-1}$ at 25 $^\circ\text{C}$, respectively [61], cooling induces a large strain at the interfaces, especially between diamond and Ir. However, since the Ir layer is relatively thin and its adhesion with diamond is very good, it is believed that Ir will deform to relieve the interfacial stress with diamond. Then, cooling leads to bending of the composite structure until a critical stress is exceeded and the SrTiO_3 fractures. This can explain the cooling-induced breakage. On the other hand, a different mechanism must be found to explain the cracking of SrTiO_3 during growth at constant temperature. The blackened condition of SrTiO_3 is due to its reduction by the hydrogen plasma at high temperature. As oxygen is removed, the lattice parameter of SrTiO_{3-x} becomes larger than that of SrTiO_3 . $\text{SrTiO}_{2.5}$, which has the same structure as SrTiO_3 , is black and conductive with lattice parameter 0.400 nm[160]. The oxygen depletion zone could be uniform throughout the SrTiO_3 , if the oxygen diffusion rate is very high, or it could be non-uniform, with greater oxygen depletion at the exposed edges. In both cases, interfacial stress would develop, whereas in the latter case, internal stress would occur within the SrTiO_{3-x} a result of the lattice

parameter gradient. Since the substrate sits on a cooled stage in the AsTeX reactor, a vertical thermal gradient is also present. The temperature gradient ~ 500 °C across the 0.5 mm substrate, would also lead to a gradient in the oxygen depletion rate, leading to a lattice parameter gradient. It was observed that the substrate would break just after 3 h of growth if the sides and the edges of the SrTiO₃ substrate were exposed. When the edges and the sides of the substrate were masked with a Mo cap, the time before breaking was extended to 15 h.

5.6.1 Raman spectroscopy

The 65 μm thick heteroepitaxial diamond film discussed above was examined with Raman spectroscopy. Figure 5.29(a) shows the Raman spectrum of this film, excited at 532 nm. A strong first-order Raman peak is observed at 1332.6 cm^{-1} , characteristic of unstrained diamond. No evidence for graphitic phase that exhibit Raman intensity between $1500\text{-}1600\text{ cm}^{-1}$ was seen.

In Figure 5.29(b) two small peaks appear at 1415 cm^{-1} (575 nm wavelength) and at 3120 cm^{-1} (637 nm wavelength). These peaks are identified as photoluminescence (PL) from substitutional nitrogen-vacancy (N-V) centers. The first peak is emission from the (N-V)⁰ center, which is a substitutional nitrogen adjacent to a vacancy in a neutral charge state. The second is emission from the (N-V)⁻ center, a substitutional nitrogen adjacent to a vacancy which has trapped an electron. Since either PL signal occurs only for a N-V pair, it cannot be used to determine the total nitrogen concentration. To estimate the nitrogen concentration, we note that homoepitaxial diamond grown with 2 ppm nitrogen intentionally added to the feed gases, produced N-V photoluminescence intensities

relative to the Raman line, larger than that seen here [123]. If it is assumed that the vacancy concentrations and their pairings with nitrogen are similar in both crystals the present crystal should have a total nitrogen incorporation of about 1 ppm.

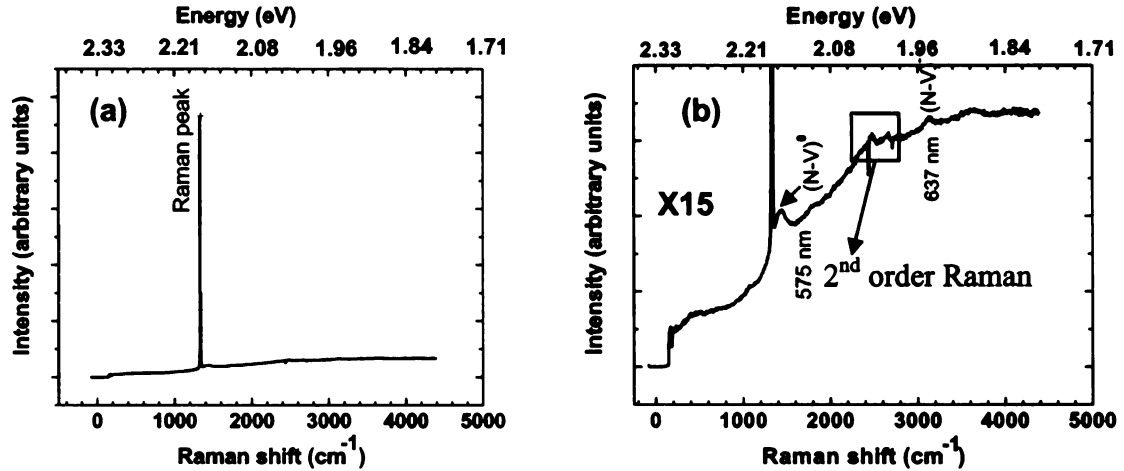


Figure 5.29 (a) Raman spectrum of heteroepitaxial CVD diamond (b) same spectrum with 15x magnification. (N-V) photoluminescence peaks and the second order Raman peak are visible. Two bad pixels in the CCD camera are responsible for the spikes seen in the vicinity of the 2nd order Raman peak.

Figure 5.30 shows Raman linewidths of heteroepitaxial and natural Type IIa diamond. Since the linewidth of Type IIa natural diamond is 1.65 cm^{-1} [143,161], we can infer an instrumental linewidth of about 1 cm^{-1} , which is also consistent with the known grating resolution. Taking this into account, the linewidth of the $65 \mu\text{m}$ heteroepitaxial diamond, grown under high growth rate conditions, is estimated as 2.9 cm^{-1} , whereas for heteroepitaxial diamond grown under low growth-rate conditions by the single-step process, the linewidth is about 7.0 cm^{-1} . Thus, the two-step process leads to a significant decrease in diamond internal strain. With even thicker crystals, one would expect heteroepitaxial diamond to approach the quality of high-purity natural diamond.

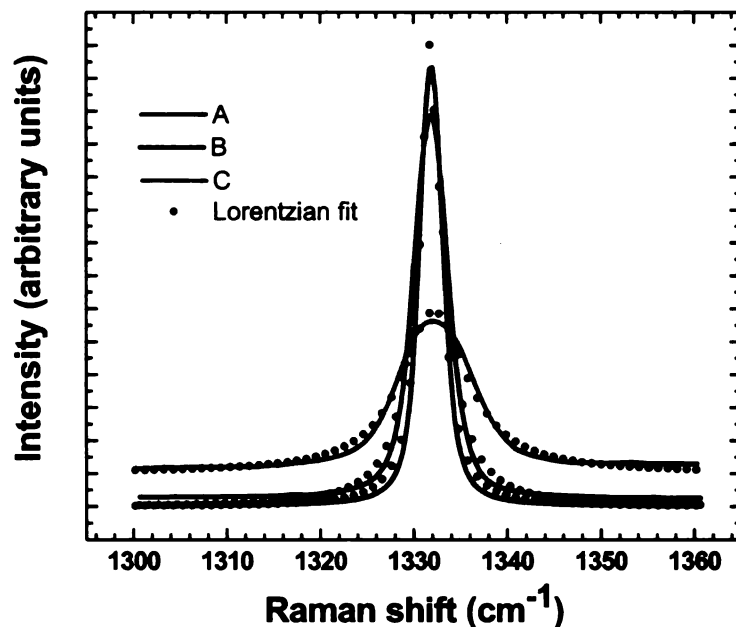


Figure 5.30 Raman spectra of two heteroepitaxial diamond crystals and a Type IIa natural diamond crystal (line A). High growth-rate heteroepitaxial diamond (line B) and low growth-rate heteroepitaxial diamond (line C). Linewidth values obtained after Lorentzian fits are respectively 2.6, 3.9 and 8.5 cm^{-1} , where an instrumental line width of 1.0 cm^{-1} has not been deconvolved from the spectra.

5.6.2 Free exciton luminescence

Observation of the free exciton luminescent signal from diamond has often been used as a measure of crystal quality. Here, we compare exciton luminescent intensities of heteroepitaxial diamond and natural Type IIa diamond. When a photon with above bandgap energy excites an electron from the valence band, it leaves a hole which can bind with the electron to form a bound state, or exciton. The exciton will decay by emitting a photon, whose energy is less than the original photon. This is called exciton luminescence.

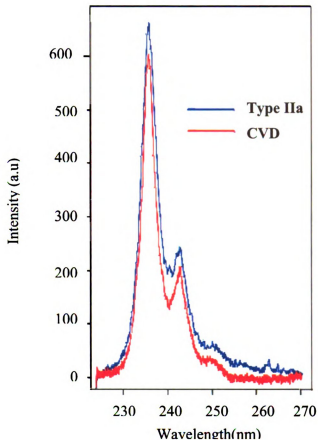


Figure 5.31 Comparison of free exciton luminescence of CVD heteroepitaxial diamond with Type IIa natural diamond, excited with 213 nm laser radiation under identical conditions at room temperature [163].

In diamond, the free exciton has a binding energy of 75 meV [162], which is large compared to typical semiconductors such as Si or GaAs with smaller bandgaps. Decay at room temperature is thermally induced so that lifetimes are relatively long. Figure 5.31 [163] shows a comparison between the free exciton luminescence from high growth rate heteroepitaxial diamond and natural Type IIa diamond, both taken at room temperature with 213 nm laser excitation under identical conditions. Both spectra are similar, but the intensity, which reflects non-radiative recombination processes, is only slightly larger for the natural diamond. This measurement suggests that the high growth rate heteroepitaxial

diamond compares favorably with natural Type IIa diamond, a conclusion which was reached from analysis of the Raman scattering.

5.7 Summary

In this study, we used Ir/SrTiO₃ substrates to understand the role of biasing in modifying the Ir surface. By systematically changing the biasing time and examining the spatial evolution of the Ir surface, we found that the Ir surface is etched by the hydrocarbon ions during the biasing. The etching process is not uniform. It first starts from the middle and then propagates toward the edge of a substrate. Faceted Ir pillars are created after biasing for only 10 min. Diamond nucleates in the channels between two faceted pillars but not, apparently, on the top (001) surface. Misfit dislocations are observed at the diamond-Ir interface as expected from equilibrium elasticity theory. The two-step process for growing thick heteroepitaxial diamond can be used to grow diamond with quality approaching that of the natural type IIa diamond.

6 Chapter 6 Homoepitaxial Growth of Diamond

In this section, growth processes for homoepitaxial diamond are described. Whereas in heteroepitaxial growth the goal was to increase the lateral dimensions of diamond crystals, here we are concerned with the growth of much thicker diamond by homoepitaxy. The growth of diamond on diamond does not rely on a difficult nucleation step; however, preparation of the diamond substrate requires careful attention prior to CVD growth. Since lattice mismatch is not an issue in homoepitaxy, the structural quality of the epitaxial diamond can be very high, virtually indistinguishable from the substrate. In diamond homoepitaxy, a common substrate is HPHT Type Ib diamond. This material contains high concentrations of impurities, so it is of interest to see whether higher purity diamond can be grown as a thick epilayer. The most common impurity in diamond is associated with nitrogen, which creates several types of defects. These may act as scattering centers for charge carriers in electronic devices, leading to sub-optimal performance. Much of this work, therefore, focuses on ways the growth process affects impurity levels, as well as the overall structural quality.

A new CVD reactor was used for this work. A significant part of the system was modified and constructed as part of this research program. After a description of some of these improvements, methods used for preparation of substrate surfaces are explained, followed by results from experiments on homoepitaxial growth. As a result of this work, free-standing diamond crystals with thicknesses over 0.5 mm and outstanding optical and structural quality were grown, as demonstrated with a variety of optical and x-ray characterization methods.

6.1 Experimental methods

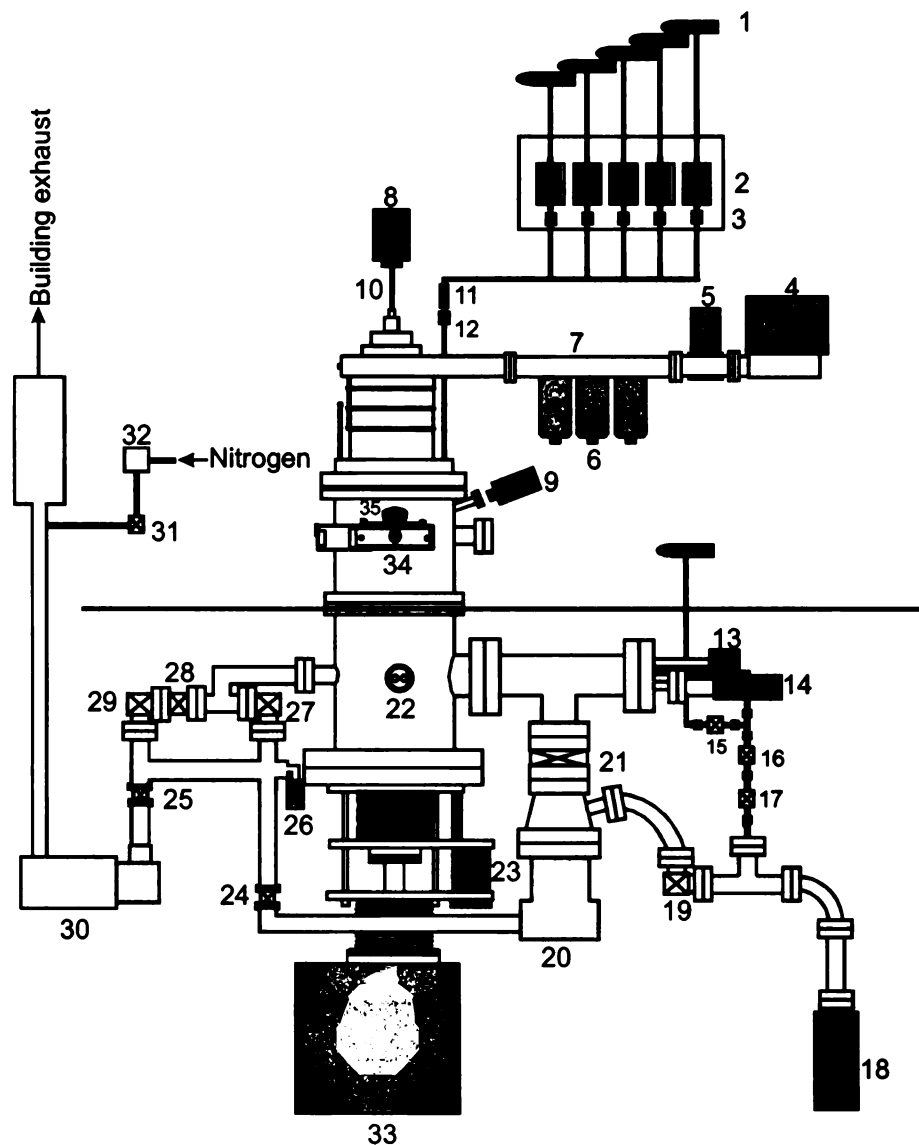
This section describes the microwave plasma CVD reactor. The reactor, based on an AsTeX design, was acquired from Seki Technotron (Japan). Since only the reactor body and microwave system were supplied, the gas handling and vacuum system were designed and constructed from individual components. A major improvement in the reactor was made by designing, constructing, and installing a water-cooled sample stage, that was retrofitted into the AsTeX system. Methods for temperature measurement, residual gas analysis, and computer-control of the CVD process are described below.

6.1.1 AsTeX diamond CVD reactor

6.1.1.1 Instrument design overview

The AsTeX-style CVD reactor is shown in Figure 6.1. Only the reactor, the central vertical structure in the figure, and the microwave components, were acquired from Seki Technotron. A 1.5kW max, 2.45 GHz microwave source connects to a TM01 mode cavity by rigid waveguide. A triple-stub tuner impedance matches the source to the cavity. The cavity contains a water-cooled motorized substrate stage, which can move 6 cm vertically. A vacuum- and microwave-tight access door is used to load samples. Two vacuum pumps are used to evacuate the chamber prior to growth and to maintain a constant pressure during the growth process. Introduction of feed gases into the chamber occurs by computer-interfaced mass-flow controllers. Temperature is monitored by two pyrometers positioned outside the reactor chamber. A PC-based LabView interface was developed to monitor and control gas flows, microwave power, substrate temperature and

system pressure. Multiple process steps can be programmed into the system, which is designed to shut down in the event of malfunctions.



- | | | |
|-------------------------------|-------------------------------|----------------------------------|
| 1. Feed gas tanks | 13. Baratron pressure gauge | 25. Isolation valve (V_{10}) |
| 2. Mass flow controllers | 14. Vacuum pressure gauge | 26. Pirani gauge |
| 3. Toggle valves | 15. Vent valve (V_5) | 27. Roughing valve (V_1) |
| 4. Magnetron head | 16. Needle valve (V_7) | 28. Throttle valve (V_{11}) |
| 5. 50 Ω load | 17. Toggle valve (V_9) | 29. Isolation valve (V_2) |
| 6. Triple stub tuner | 18. Residual gas analyzer | 30. Roughing pump |
| 7. Rectangular wave guide | 19. Shut-off valve (V_8) | 31. Flushing valve (V_{12}) |
| 8. Two color pyrometer | 20. Turbo-molecular pump | 32. Flow meter |
| 9. One color pyrometer | 21. Gate valve (V_6) | 33. Heater power feedthrough |
| 10. Optical fiber | 22. Cooling water feedthrough | 34. Loading door |
| 11. Inline gas filter | 23. Stage control motor | 35. Growth chamber |
| 12. Inlet gas valve (V_4) | 24. Backing valve (V_3) | |

Figure 6.1 Schematic of CVD reactor used for homoepitaxial diamond growth.

6.1.1.2 Gas handling

The gas handling system is responsible for producing and maintaining the gaseous environment in the reactor chamber. An air-cooled turbo-molecular pump (Pfeiffer) backed by a roughing pump (Alcatel) reduces system pressure to a base level of 3×10^{-8} Torr. A low base pressure is necessary to insure that residual gas concentrations are reduced below the ppm level. A high-throughput gate valve (VAT) isolates the main chamber from the turbo-pump. Feed gases, from high-pressure cylinders, are introduced by individual mass flow controllers (MKS 1249). They are interfaced to a control box (MKS 427 type D), which is monitored and controlled by the PC. Each mass flow controller is isolated from the main flow line by a shutoff valve to eliminate leakage through the flow controller. Pressure is controlled by a throttle valve (MKS type 653) interfaced to a pressure controller (MKS type 651C) that uses as pressure sensor a 0-1000 Torr range capacitance gauge (MKS type 626A). The pressure controller is interfaced to the PC and system pressure is maintained within ± 0.1 Torr of the set-point (typically in the 30-200 Torr range).

Since the system does not have a load lock, it is necessary to expose the sample chamber to atmosphere when loading. This introduces nitrogen into the system which must be removed by the turbopump. A residual gas analyzer is used to evaluate vacuum quality. When the system is brought to atmospheric pressure, Ar gas is used as a venting gas since it does not affect crystal properties. During plasma processing, the dominant gases used are H_2 and CH_4 . At the roughing pump output, exhaust gases are mixed with nitrogen to reduce the hydrogen concentrations below 4 %, the explosive lower limit, before they are exhausted through a vent.

6.1.1.3 Sample stage and sample cooling

The as-received reactor was equipped with an inductively-coupled heating stage. For homoepitaxial growth, it is desirable to maintain a relatively low substrate temperature in the presence of high microwave power. Therefore, the original stage was modified for water cooling, as shown in Figure 6.2. Water is introduced by one of two 0.25" dia stainless steel tubes into a hollow stainless steel stage clamped onto the top of an existing platform. Since the reactor allows for application of a DC bias to the sample stage, all connections, including the water lines, needed to be electrically isolated from ground potential. Water is circulated by a water-to-water heat exchanger (Haskris) with 16 l/min flow capacity for cooling reactor walls and magnetron head. Part of this flow, 6 l/min, was used for stage cooling. Since the cooling is critical to reactor function, a low-flow condition triggers an alarm and initiates a reactor shutdown.

In the microwave cavity, the substrate is placed on a Mo post threaded into the cooled stage. A Mo cap is placed around the post so that plasma forms at the sample position. The height of the substrate relative to the top of the cap is adjusted by rotating the threaded post. A Mo plate on short stand-offs protects the cold plate from the plasma.

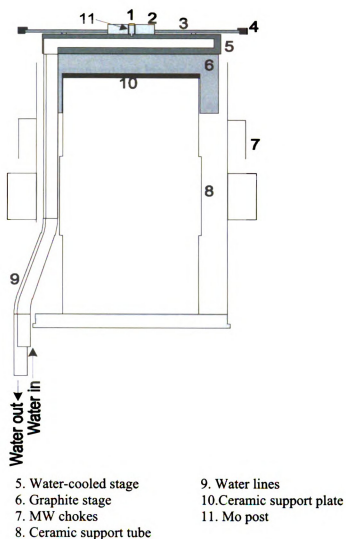


Figure 6.2 Schematic of cooling stage and substrate holder

6.1.1.4 Temperature measurement

Infrared pyrometers are used to measure substrate temperature. A two-color pyrometer (Williamson) (sensitive to 2.4 and 2.2 μm ir radiation) is positioned directly above the substrate with only a single, intervening fused quartz window. The focal point can be adjusted with the help of a laser beam that passes through two focusing lenses onto the emitting region. The field of view is 4 mm dia at a distance of 45 cm.

Differential absorption at the two ir wavelengths must be negligible if the pyrometer calibration is to be maintained. A single-color pyrometer (Ircon) is focused on the sample through a side window. This instrument has higher sensitivity and was used as a working thermometer. The pyrometers were calibrated at the Au melting point (1065 °C) inside the reactor. Details are given in Appendix B.

6.1.1.5 Residual gas analysis

The gas handling system included a residual gas analyzer (RGA) used to monitor gas composition during reactor operation. Since the RGA only functions below 10^{-4} Torr, a differentially-pumped RGA chamber was constructed, in which reactor gases were introduced by a needle valve, Figure 6.1. When the process chamber is at low pressure with the turbopump running, the gate valve and isolation valve are open so the RGA can be operated below the upper-pressure limit. During growth, with the main chamber above 100 Torr, the gate valve is closed so that the RGA is connected to the main chamber through the needle valve side. The turbopump then pumps on the RGA through the open isolation valve without affecting the main chamber, so that the pressure remains below 10^{-4} Torr.

Figure 6.3 shows how partial pressures of several mass species evolve during a 4 h growth run. Only hydrogen and methane were introduced into the reactor here, at a 4% methane to hydrogen ratio. Prior to methane introduction, all partial pressures were below 10^{-7} Torr, with the exception of hydrogen, which is always present at high concentrations. With methane in the chamber, chemical reactions create hydrocarbon species, predominantly 26 amu acetylene (C_2H_2). Since the RGA is located far from the reaction

chamber, transient species will probably not be detected. However, the RGA itself can create radicals, accounting for the observation of methyl species at 15 amu, derived from methane at 16 amu. Unambiguous detection of N_2 is difficult since it coincides with ethylene (C_2H_4) at 28 amu.

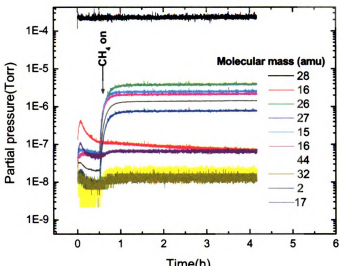


Figure 6.3 RGA spectrum taken during diamond growth at 150 Torr.

6.1.2 Operational procedures

An abbreviated procedure for homoepitaxial diamond growth is given in this section.

6.1.2.1 Substrate loading

The Mo post is first threaded into the cooling plate and the Mo cap inserted around the post. The substrate is placed on the Mo post and the Mo plate installed around the cap. The stage is translated vertically to its standard position and pyrometers are

focused onto the substrate. The reactor door is closed and the chamber turbopumped to 1×10^{-7} Torr or lower.

6.1.2.2 System operation

With system pressure below 1×10^{-7} Torr, gas partial pressures are recorded. Gases consist mostly of water vapor, 3×10^{-8} , N_2 , 3×10^{-9} and Ar, 1×10^{-9} Torr. With the turbopump off and gate valve closed, H_2 flow is initiated at 300 sccm until the pressure reaches 100 Torr. The growth chamber is then slowly pumped out to flush the roughing line with H_2 . At 10 Torr, application of 300 W microwave power ignites the plasma. After ignition, pressure and power are slowly increased to the required level. After stabilization of temperature and pressure, other gases are introduced as needed. After completion of the run, all gases with the exception of H_2 are turned off, and system power and H_2 pressure are gradually reduced to 100 W and 10 Torr, respectively. MW power is turned off and the remaining gases are pumped out. After 10 min or so, when the sample has cooled, the main chamber is vented with Ar and the sample is removed in flowing Ar. The main chamber is then pumped out and sealed under vacuum.

6.2 Growth process

This section describes the details of diamond substrate preparation using chemical cleaning and plasma etching. The rationale is to prepare the substrate surface so that no defects propagate into the growing epitaxial film from the substrate.

6.2.1 Diamond substrate preparation

6.2.1.1 Type Ib diamond substrates

In homoepitaxy, the surface of the substrate on which the epilayer is grown plays a crucial role. Homoepitaxial diamond is grown on HPHT Type Ib diamond substrates. The (001) surface was chosen since the probability of defect formation, principally penetration twins, is lower relative to (110) or (111) surfaces [164]. Type Ib Somicrystals (Sumitomo Electric) are yellow since they normally contain 100-150 ppm substitutional nitrogen and were supplied as $3 \times 3 \text{ mm}^2$ parallelepipeds with (001) polished major surfaces. The crystals were $0.5 \pm 0.05 \text{ mm}$ thick, with a misorientation angle less than 1 deg from (001) as confirmed by x-ray diffraction. Figure 6.4 shows an optical photograph of a HPHT crystal taken in white light.

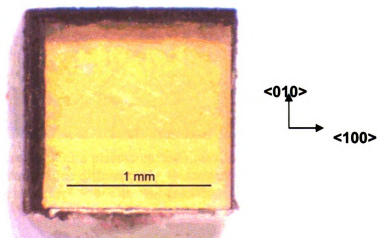


Figure 6.4 Optical photograph of a HPHT Type Ib diamond substrate taken in white light. Left and the top sides were laser-cut with a slight bevel.

HPHT diamond contains several types of imperfections that may influence subsequent epitaxial growth, such as growth sectors, inclusions, and surface damage.

Growth sectors arise during HPHT growth when different crystal planes grow at different rates and incorporate different concentrations of nitrogen [165]. When the crystal is cut into small pieces, each piece may contain several growth sectors, usually representing [001] and [111] growth directions.

Fig. 6.5 shows a HPHT crystal after 1 h of plasma etching. The dark objects on the surface are etch pits, to be described below. For this crystal, all 6 surfaces are {100} planes. The two lines intersecting the top surface at 45 deg are {111} planes at the boundaries of growth sectors. The change of refractive index at the boundary creates sharp contrast in a DIC image.

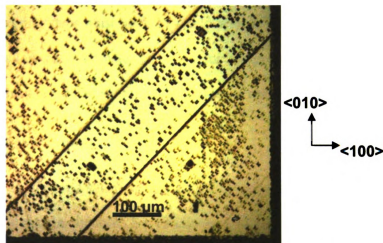


Figure 6.5 DIC micrograph of a plasma-etched diamond substrate. Dark objects are etch pits. The crystal contains three different growth sectors, separated by the dark lines along $\langle 110 \rangle$. They represent regions with different growth directions.

HPHT growth uses transition metals, predominantly Fe and Ni, as catalysts. Inclusions arise when part of the catalytic melt is trapped inside a crystal. Inclusions are generally quite small and not easily visible by optical microscopy of as-received substrates. They may appear after plasma etching, as discussed below.

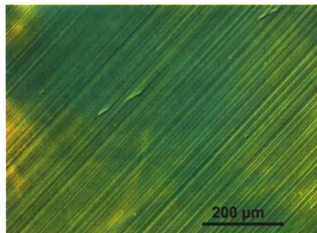


Figure 6.6 Polishing scratches on the surface of a type Ib HPHT diamond substrate

Surface-related damage is generally associated with polishing of the surface. Diamond grit leaves scratches, Figure 6.6, which can penetrate 3-4 μm below the surface. A series of processing steps must be followed to remove scratches, embedded diamond grit, and any shallow catalyst inclusions. The surface preparation must be sufficiently reliable that not even one defective region is allowed to remain.

6.2.1.2 Chemical cleaning

As-received diamond substrates are cleaned sequentially in acetone, iso-propanol and water using ultrasonic agitation for 10 min each to remove organic or water-soluble contaminants. They are then ultrasonicated in Alconox solution in DI water for 0.5-1 h to remove particulates. A solution of 25 ml of H_2O_2 (hydrogen peroxide) and 25 ml of H_2SO_4 (sulphuric acid) is mixed in a round-bottom flask. The diamond substrate is placed in the flask and the solution boiled at 300 $^\circ\text{C}$ for 0.5 h using a flask heater. This process removes metallic and graphitic contaminants. After cooling, the substrate is rinsed in DI water, N_2 dried, and placed inside a clean substrate carrier box. The substrate is sequentially ultrasonicated in DI water and iso-propanol and optical micrographs taken

made reference. Sample thickness is measured with a stand-mounted gauge (Mahr) with 1 μm resolution and maximum travel 5 cm. Since the gauge's tip can transfer iron to the diamond surface, each time a thickness measurement is made the crystal must be cleaned with aqua-regia to remove contamination. This gauge is also used to measure changes in crystal thickness so that vertical growth rates can be calculated.

6.2.1.3 Hydrogen –Oxygen plasma etching

A plasma etching process was developed to remove the damaged region from the top surface of diamond substrates. The idea is to remove the minimum amount of diamond necessary to produce a microscopically-undamaged surface suitable for subsequent CVD growth. Typical etch chemistry has previously utilized pure hydrogen[109] or a hydrogen-oxygen plasma [127,166,167]. In most cases, we used a dilute oxygen-in-hydrogen plasma. Several variables were examined and optimized, including system pressure, substrate temperature; etch time, and oxygen-hydrogen ratio.

Etching experiments were conducted inside the CVD reactor, with oxygen concentrations 0.5-3.3 % relative to H_2 concentration, total gas pressure 70-150 Torr, and temperatures from 675-930 $^\circ\text{C}$. The etch rate was determined by thickness measurements, with uncertainty $\pm 2\mu\text{m}$, made at the middle and four corners of the sample.

When diamond is plasma etched, material removal is not spatially uniform, but small pits appear, often with crystallographic registration. At 675 $^\circ\text{C}$, 150 Torr, and 2 % oxygen-hydrogen ratio, etching was slow and scratch marks remained after 1.5 h. The etch depth was about 1 μm and etch pits of average lateral size 1 μm appeared. At 725 $^\circ\text{C}$ the surface was covered with shallow pits and an etch rate of 1.5 $\mu\text{m}/\text{h}$ was observed. The

typical lateral pit size was 15 μm . At 800 $^{\circ}\text{C}$, the vertical etch rate increased to 3 $\mu\text{m}/\text{h}$ with lower pit density, but the average lateral pit size became larger, 25 μm .

It was realized that etch pits do not necessarily lead to defects that propagate into the growing crystal. The types of pits that appeared were readily classified, and malicious pits identified. Two benign types of rectangular/square pits were commonly observed: one with (111) lateral facets (type A) and the other with a flat (001) bottom (type B) as shown in Figure 6.7. The pit sides are aligned along [110].

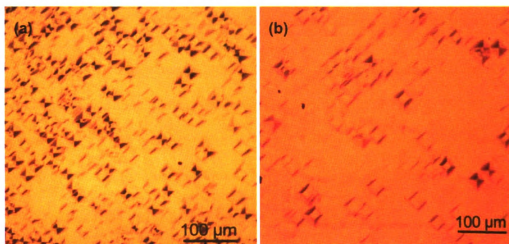


Figure 6.7 Diamond surface after plasma etching at $r_o = 2\%$, $p = 150$ Torr (a) $T = 725$ $^{\circ}\text{C}$, $t = 1$ h (b) $T = 800$ $^{\circ}\text{C}$ $t = 1$ h. Two types of etch pits are observed

The size of the pits could be reduced by operating at 100 Torr. Figure 6.8(a) shows the surface of a diamond substrate etched at 2% oxygen concentration, 800 $^{\circ}\text{C}$ and 100 Torr for 1.5 h to a depth of 2 μm .

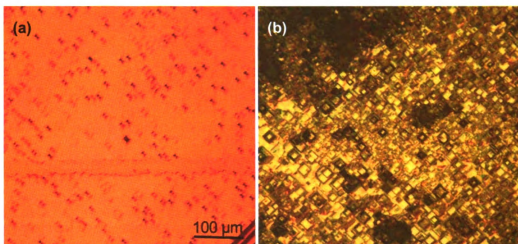


Figure 6.8 Diamond surface after plasma etching at $p = 100$ Torr, $r_o = 2\%$ (a) $T = 800$ °C, $t = 1.5$ h (b) 930 °C, $t = 1.5$ h, deep holes and large pits are created on the surface

Etching at higher temperature and higher oxygen concentration created many deep, large holes on the surface as seen in Figure 6.8(b) for etching at 930 °C and 1.5 h. An etch time of 2 to 3 hours at 800 - 850 °C, 100 Torr and 2% oxygen concentration was found to be optimal for most substrates.

To study the effect of etch duration on the morphology of the pits, a diamond sample was etched in four sequential steps at 100 Torr, 850 °C and 2% oxygen concentration for a total of 2.5 h. After each step, the sample was removed from the reactor and examined optically. The first etching step was 1 h while the other steps lasted 0.5 h. After 2.5 h, the total etch depth was about 4 μm .

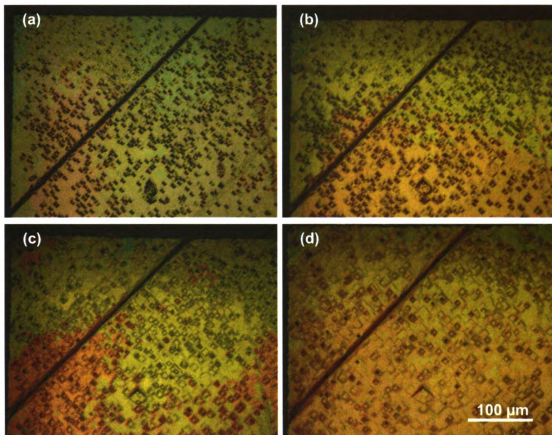


Figure 6.9 DIC micrograph of diamond substrate after etching in plasma for a total time of 2.5 h at $r_o = 2\%$, $T = 850\text{ }^\circ\text{C}$ and $p = 100\text{ Torr}$; (a) 1h (b) 1.5 h (c) 2 h (d) 2.5 h. Dark line is a growth sector.

Figure 6.9(a)–(d) shows micrographs taken after each step of the etching. Image J software was used to analyze the size and the number of the etch pits in the figure. Figure 6.10(a) shows the total number of etch pits per image vs. etch time. The number of etch pits decreased after one hour. Figure 6.10(b) shows the average etch-pit size and areal coverage vs. etch time. The average size increased from $6\text{ }\mu\text{m}$ to $13\text{ }\mu\text{m}$ and the coverage increased from 12 to 26%, when the time increased from 1 to 2.5 h. Figure 6.10(c) shows the number of type A and type B etch pits vs. etch time. Type A pits decreased from 800 to 60, whereas type B etch pits increased from 250 to 360, with the

maximum at the third etching step with 380, when the etching time increased from 1 to 2.5 h.

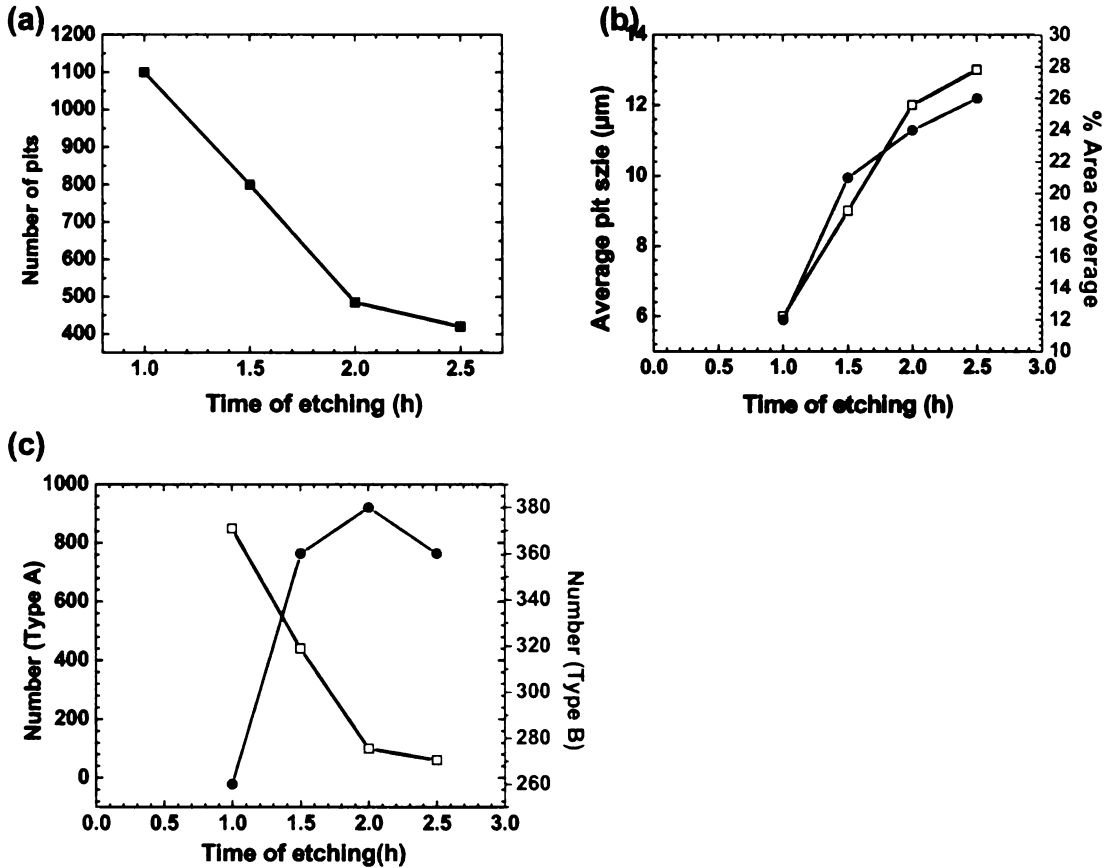


Figure 6.10 Etch pit statistics. (a) Number of etch pits vs. time of etching; etch pit number decreases with time. (b) Average pit size, % area coverage vs. time of etching (c) number of type A and B pits vs. time of etching. Number of type A decreases but B increases.

After 1 h, a few polishing scratches remained on the surface but all were removed after 2.5 h. The decrease in the pit density after 1 h etching was most likely caused by the merging of pits as their size increased. Clearly, the pit density must reach a maximum before 1 h. The A and B pits are not independent. The A pits form initially with $\{111\}$ sidewalls. As etching continues, they become deeper. At a relatively shallow depth, the

anisotropy of the etching changes, with the {111} surfaces etching faster than {100}. This leads to flat-bottomed etch pits.

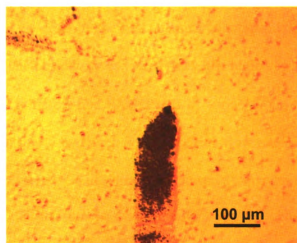


Figure 6.11 Diamond surface after plasma etching at $T = 850\text{ }^{\circ}\text{C}$, $p = 100\text{ Torr}$, $r_o = 2\%$ and $t = 1\text{ h}$. The large dark region is a pit forming at inclusions.

In addition to these benign pits, a third type of etch pit was sometimes observed. This pit had depths as large as $10\text{ }\mu\text{m}$ and showed no specific geometrical shape. It is believed that it forms at regions with foreign inclusions. Figure 6.11 shows a diamond sample etched for 1 h at $850\text{ }^{\circ}\text{C}$ 100 Torr and 2 % oxygen concentration. The dark region in the micrograph is a group of malicious pits. Energy dispersive x-ray (EDX) showed the signatures of Ni, Fe and Al in this region. Defects will emerge from these regions if the inclusions are not removed prior to growth. Usually, flat-topped pyramidal hillocks (without non-epitaxial crystallites) grew out of these pits

6.2.2 CVD homoepitaxial diamond growth process

6.2.2.1 Preliminary processing results

In this section we describe the first attempts at homoepitaxial growth using 1.5 x 1.5 mm² substrates. The objective was to determine the region of parameter space where growth was reasonably defect-free. Definitions of variables are: substrate (or growth) temperature, T_g , methane to hydrogen ratio (based on flow rates), r , growth duration of step i , t_i , total gas pressure, p , and microwave power, P . For the experiments discussed immediately below, the pressure was held constant and the geometry was not varied. Growth was carried out in steps, with the sample taken out of the reactor after each step and examined by optical microscopy.

Diamond was grown on four different substrates at $r = 4\%$ and $T_g = 800\text{-}950\text{ }^\circ\text{C}$, as given in Table 6.1. Substrate temperature was controlled by adjusting the microwave power. Growth pressure was fixed at 150 Torr and growth duration was varied from 3-6 h.

Table 6.1 Growth conditions for 4 samples grown at different temperatures. The symbol h_i is the epilayer thickness and V_{001} is the $\langle 001 \rangle$ growth rate

sample	p (Torr)	P (W)	T_g ($^\circ\text{C}$)	r (%)	t_i (h)	h_i (μm)	V_{001} ($\mu\text{m/h}$)
A ₁	150	1450	950	4	3	12	4
A ₂	150	1350	900	4	4	14	3.5
A ₃	150	1300	850	4	3	8	2.7
A ₄	150	1100	800	4	3	7	2.3

Figure 6.12 shows diamond surfaces grown at different temperatures. With $T_g = 950\text{ }^\circ\text{C}$, after 3 h the surface of A₁ was almost fully covered by pyramidal hillocks (a). The dark region on the top of the hillock is a non-epitaxial crystallite; hillock sides show

macro-steps parallel to [110]. The height of the highest hillock was 2.5 μm , as measured by a Dektak profilometer. The growth rate under these conditions was 4 $\mu\text{m}/\text{h}$.

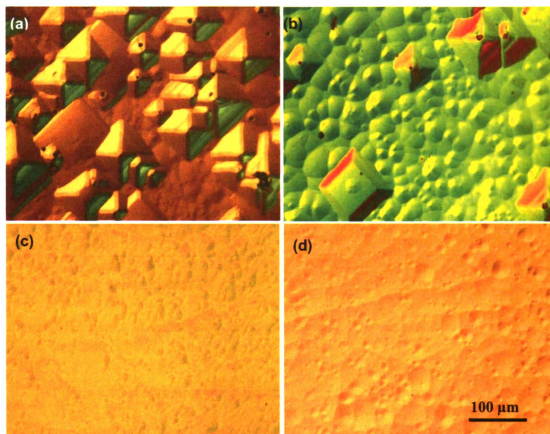


Figure 6.12 DIC micrographs of diamond surfaces grown at 4% methane concentration, 150 torr and (a) 950 °C (b) 900 °C (c) 850 °C (d) 800 °C temperature.

With $T_g = 900$ °C, hillock density is shown in Figure 6.12(b). As in (a), most hillocks contained a non-epitaxial crystallite at their apex. Growth rate in this case dropped to 3.5 $\mu\text{m}/\text{h}$.

Growing at $T_g = 850$ °C produced no large pyramidal hillocks, but the surface was covered by tiny round hillocks without non-epitaxial crystallites, as shown in Figure 6.12 (c). Maximum height of these hillocks is 0.2 μm .

Growth at $T_g = 800\text{ }^\circ\text{C}$ produced the diamond surface shown in Fig. 6.12(d). Note the shallow height fluctuations and absence of hillocks; however, the growth rate decreased to $2.3\text{ }\mu\text{m/h}$ under these conditions.

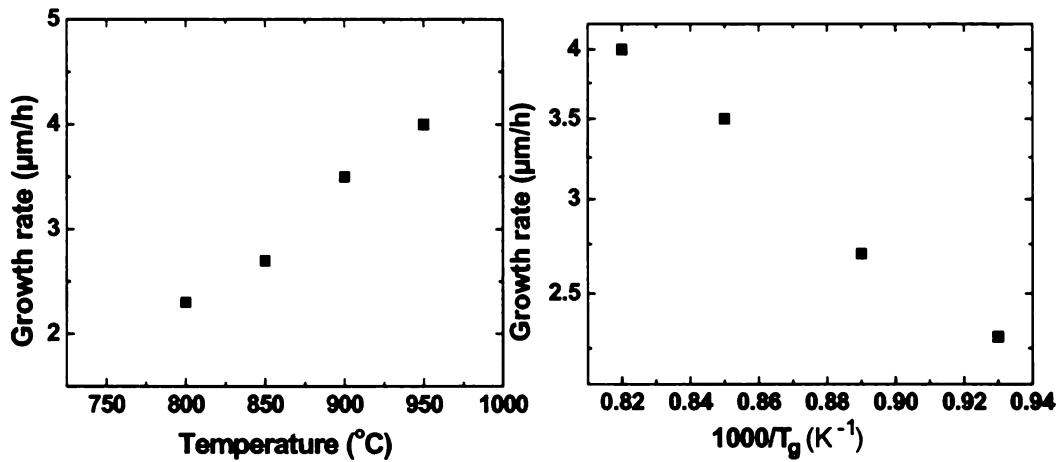


Figure 6.13 Effect of temperature on growth rate at 4 % methane concentration in gas phase.

Figure 6.13 shows a plot of the growth rate vs. substrate temperature. Growth rate obeys an Arrhenius relation given by $V_{001} = A \exp(-E_a/k_B T_g)$. The activation energy E_a for this temperature range is found to be 10 Kcal mol^{-1} or 0.5 eV/atom , similar to values previously reported [109,125].

To study the effect of methane concentration on defect formation and growth rate, three different diamond crystals were grown at $r = 2.6\text{-}8\%$. First, an epilayer was grown at $r = 2.7\%$ at $800\text{ }^\circ\text{C}$ for 7 h. Then it was overgrown at $r = 4\%$ and $800\text{ }^\circ\text{C}$ for an additional 3 h. Figure 6.14(a) shows the diamond surface after the first growth. There are several shallow pits visible; however, all the pits filled in after the second growth stage at higher methane concentration. The resulting surface is quite smooth.

Table 6.2 Growth conditions for diamond grown in two stages at different methane concentrations; $r = 2.7$ and $r = 4\%$ at $800\text{ }^{\circ}\text{C}$.

Sample	p (Torr)	P (W)	T _g (°C)	r (%)	T ₁ (h)	h ₁ (μm)	V ₀₀₁ (μm/h)
A ₅	150	1150	800	2.7	7	12	1.7
A ₅	150	1100	800	4	3	7	2.3

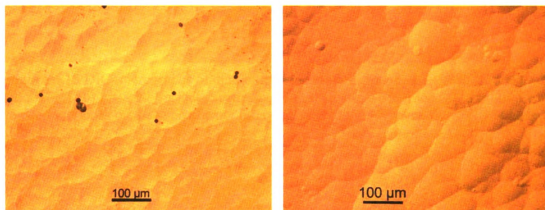


Figure 6.14 DIC images of a diamond sample after growth at $800\text{ }^{\circ}\text{C}$, (a) at $r = 2.7\%$, $t = 7\text{ h}$ and (b) at $r = 4\%$, $t = 3\text{ h}$.

Table 6.3 Growth conditions for two diamond samples grown at different methane concentrations at $T = 770\text{ }^{\circ}\text{C}$ and $t = 6\text{ h}$.

sample	p (Torr)	P (W)	T _g (°C)	r (%)	t ₁ (h)	h ₁ (μm)	V ₀₀₁ (μm/h)
A ₆	150	1000	770	7	6	28	4.5
A ₇	150	1000	770	4	6	29	4.8

Next diamond films were grown on different substrates at $770\text{ }^{\circ}\text{C}$ for 6 h at $r = 7$ and 8% , Table 6.3. Figure 6.15 shows their surfaces, both of which are quite smooth and defect-free.

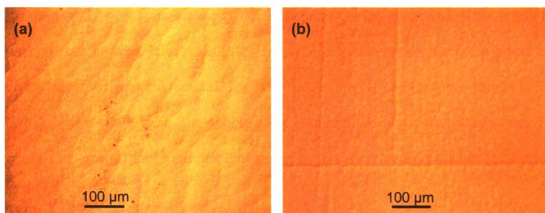


Figure 6.15 DIC micrographs of diamond surfaces after growth at $T = 775\text{ }^{\circ}\text{C}$ and $t = 6\text{ h}$, (a) $r = 7\%$ (b) $r = 8\%$. Surfaces seem smoother than at $r = 4\%$. Lines seen in (b) are due to deep scratches on the substrate not removed by etching; however, they did not generate defects.

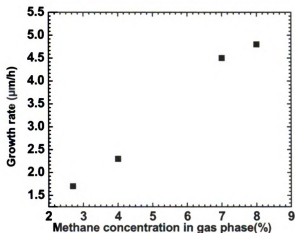


Figure 6.16 Growth rate vs. methane-hydrogen ratio r . The upper two points represent growth at $T_g = 770\text{ }^{\circ}\text{C}$; the lower two are for $T_g = 800\text{ }^{\circ}\text{C}$.

Next, thicker diamond crystals were grown by a multi-step process to $310\text{ }\mu\text{m}$. Crystal A_6 was grown at $r = 7\%$ and A_7 was grown at $r = 8\%$ under the conditions given in Table 6.4. Smooth surfaces without hillocks resulted; only a few shallow pits appeared. Figure 6.17 shows an SEM image of A_6 tilted at 45 deg to the electron beam. The top

surface is (001); {111} facets appear in each corner. At the lower part of the image the substrate can be seen. It is evident that appreciable lateral growth has taken place. The major lateral surfaces are rounded, not faceted. An optical micrograph is shown in Fig. 6.18, taken in white light. The yellow color is due to the substrate, still attached. The crystal is as-grown; only some graphitic deposits were removed from the back surface.

Table 6.4 Growth conditions for samples A₆ and A₇

sample	p (Torr)	P (W)	T _g (C)	r (%)	t (h)	h (μm)	V ₀₀₁ (μm/h)
A ₆	150	1000	775	7	68	310	4.6
A ₇	150	1000	775	8	59	290	4.9

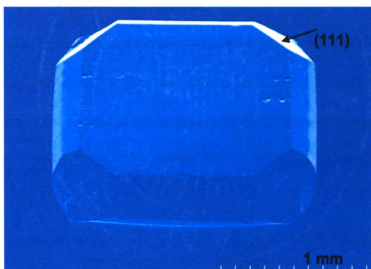


Figure 6.17 SEM image of a 290 μm thick diamond crystal on substrate. {111} faceting at the corners occurs. Tilt angle is 45 deg.

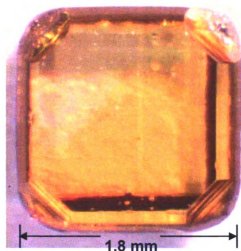


Figure 6.18 Optical photograph of a $290\ \mu\text{m}$ thick film on its substrate. The dark bands are artifacts which occur in regions where total internal reflection occurs.

6.2.3 Long-term growth procedures

We have used multi-step processes to obtain diamond crystals as thick as $550\ \mu\text{m}$ on $3 \times 3\ \text{mm}^2$ substrates. A film was grown for a specified period, taken out of the reactor, examined in an optical microscope, returned to the reactor, and growth resumed. As many as 8 stages were used, usually with different processing parameters at each stage.

A film grown at $T_g = 770\ ^\circ\text{C}$, $r = 7\%$, and $t_1 = 6\ \text{h}$ produced a smooth diamond surface as shown in Figure 6.19(a) with $V_{001} = 4.2\ \mu\text{m}/\text{h}$, comparable to earlier experiments on small substrates.

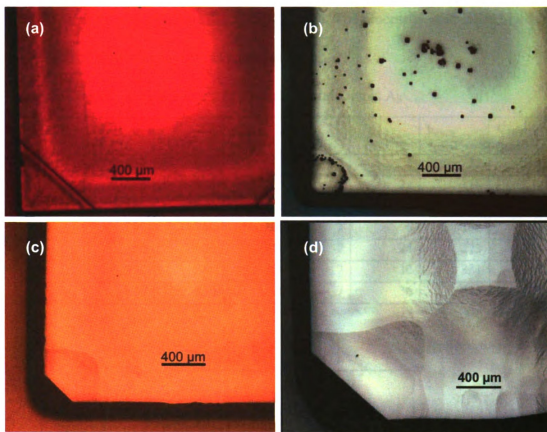


Figure 6.19 DIC micrographs of crystal A_8 after different growth periods and conditions (see Table 6.5); (a) 770 °C, 25 μm , growth sector boundary is seen at the corner, (b) 755 °C, 117 μm , faceted deep pits appeared, (c) 800 °C, 273 μm , pits are healed at higher temperature, (d) 800 °C, 515 μm macro steps observed. Total thickness of epilayer at each stage is given.

Growth at 755 °C for 22 h in the next step produced several deep pits as shown in Figure 6.19(b). The sides of the pits are parallel to [100]. There is no apparent correspondence between these pits and those formed during plasma etching on the substrate. In the next step, growth at 800 °C for 24 h healed all pits, leaving a smooth surface, Figure 6.19(c). In the next two steps, the crystal was grown for 48 h at 800 °C to a cumulative thickness $h_{\text{cum}} = 515 \mu\text{m}$. The total growth time for all steps was 110 h,

yielding an average growth rate $V_{\langle 100 \rangle} = 4.7 \mu\text{m/h}$. The process is summarized in Table 6.5 where cumulative epilayer thicknesses are given.

Table 6.5 Growth conditions for a 515 μm thick film sample A_8

Sample	P (Torr)	P (W)	T_g ($^{\circ}\text{C}$)	r (%)	t_i (h)	h_{cum} (μm)	V_{100} ($\mu\text{m/h}$)
A_8	150	950	770	7	6	25	4.2
A_8	150	900	755	7	22	118	4.4
A_8	150	950	800	4	4	132	3.5
A_8	150	900	800	7	6	158	4.3
A_8	150	900	800	7	24	273	4.8
A_8	150	860	800	7	12	331	4.8
A_8	150	850	800	7	36	515	5.1

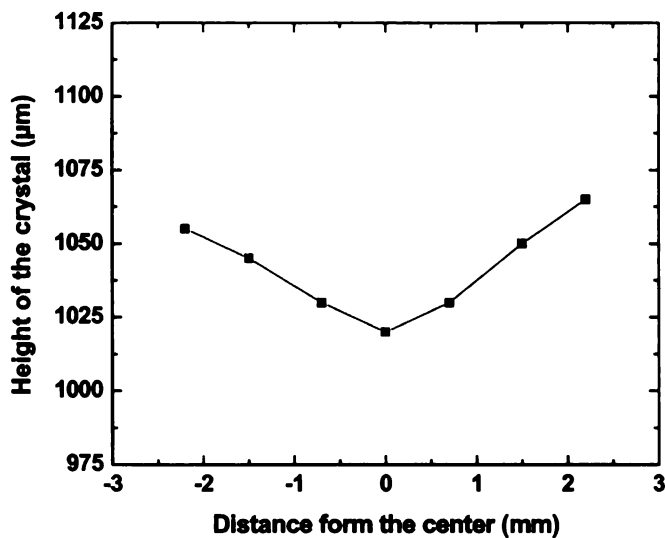


Figure 6.20 Height profile of diamond crystal A_8 along its top surface diagonal

In contrast to the small substrates, the diamond growth rate here was faster at the edges of the substrate. At the end of the growth stages, the film edges were 50 μm higher than in the middle of the top surface. Roughening was more pronounced, with macrosteps

appearing along the thickness gradient, as seen in Figure 6.19(d). The surface profile, taken by scanning along the diagonal, is shown in Fig. 6.20.

Figure 6.21(a) is an optical photograph of crystal A_8 on its substrate. Here, surface steps, though present, are not visible. Significant (111) faceting appears at the four corners. No sign of pits or growth defects can be seen. During growth, the lateral dimensions increased from 3.0 to 3.8 mm. To examine the epitaxial diamond without the influence of the substrate, the crystal was processed by a commercial diamond cutter. The substrate was removed by grinding, resulting in the crystal shown in Figure 6.21(b). The clarity and absence of optical distortion of the diamond is evident. However, it was found that at least $35\ \mu\text{m}$ of substrate was not removed, resulting in the slightly yellow tinge in the image.

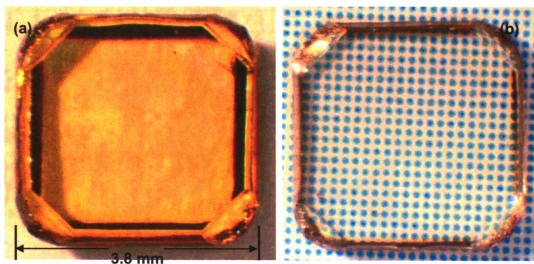


Figure 6.21 Optical photographs of a $515\ \mu\text{m}$ thick diamond crystal taken in white light (a) on its substrate. (b) after removal of most of the substrate. The crystal still contains at least $35\ \mu\text{m}$ of its substrate.

Another crystal, A_9 , was grown to a final thickness of $550\ \mu\text{m}$. In this case, four stages were used, as shown in Table 6.6. To better understand the role of residual

impurities, purer feed gases were used, 99.9999% for H₂ and 99.999% for CH₄, compared to 99.9995% for H₂ and 99.99% for CH₄ used before. The first stage was carried out at low *r* to suppress defect formation at the substrate-epilayer interface. After growth, the substrate was removed by mechanical grinding; the top surface was also flat ground and polished, as shown in Figure 6.22. In contrast to most growth experiments, the substrate used for A₉ did not have (001) and (010) lateral edges. As a result, the {111} corner facets of the homoepitaxial crystal were smaller and rotated with respect to the crystal's edges.

Table 6.6 Growth conditions for sample A₉

sample	<i>p</i> (Torr)	<i>P</i> (W)	<i>T_g</i> (C)	<i>r</i> (%)	<i>t_i</i> (h)	<i>h_i</i> (μm)	<i>V₁₀₀</i> (μm/h)
A ₉	150	1050	800	4	6	15	2.5
A ₉	150	950	800	7	10	48	4.8
A ₉	150	900	800	7	48	231	4.8
A ₉	150	900	775	8	49	256	5.2

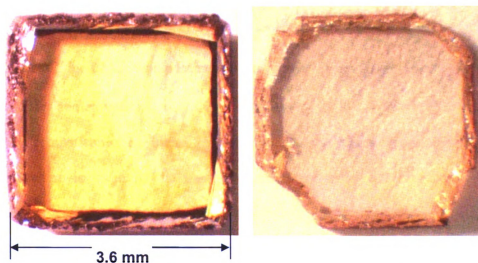


Figure 6.22 (a) Optical photograph of a 550 μm thick crystal on its substrate. For this substrate <110> was 11 deg from a lateral face. (b) CVD diamond crystal after polishing off the substrate. This crystal's corners were damaged during polishing.

A diamond crystal A₁₀ was grown to a thickness 515 μm for a total of 120 hours at $r = 6\%$ and $T_g = 800\text{ }^\circ\text{C}$. This sample was characterized using x-ray diffraction and Raman scattering discussed in section 6.3.

6.2.4 Nitrogen in CVD diamond

In this section we discuss the role of nitrogen in CVD diamond. As noted previously, a manifestation of nitrogen in diamond at the 100 ppm level is the yellow color imparted to crystals. There may be several types of nitrogen-related centers introduced in the epitaxial growth process. The tools to study the impurity states were Raman scattering, photoluminescence spectroscopy, and infrared absorption spectroscopy. Fortuitously, the spectral range of the cleanroom Raman instrument, when using 532 nm excitation light, included the PL wavelengths of the two dominant nitrogen-vacancy centers. The zero-phonon line (ZPL) for the (N-V)⁻ center occurs at 1.95 eV (637nm) and at 2.16 eV (575 nm) for the (N-V)⁰ center[29]. By assuming that the 1332 cm⁻¹ line for the single Raman-active phonon has the same intensity for all Type Ib substrates and epilayers, it is possible to normalize the PL signals to the Raman line, allowing comparison of PL intensities taken under different conditions. Justification for this procedure is given by the identical Raman linewidths observed for all crystals studied. The same experimental setup was used for all measurements, namely, a 100x objective to focus the excitation light to a spot at the surface of the sample. Since the system is not strictly confocal, backscattered Raman light and PL are collected from a region approximately 50-75 μm below the surface. Additional evidence for the high structural quality of CVD diamond is given by high-resolution XRD. The object of the

research presented in this section is to relate the concentrations of nitrogen and N-V centers to growth conditions.

6.2.4.1 Type Ib substrate

Since many of the studies were made with the epilayer attached to the substrate, the properties of the HPHT diamond substrate were first examined, using the Raman instrument, to study sample-to-sample variability of luminescence intensity and distribution. Although the Raman lines were nearly indistinguishable for all samples, some substrates showed a broad luminescence background that appeared simultaneously with weak N-V PL peaks, as seen in Figure 6.23.

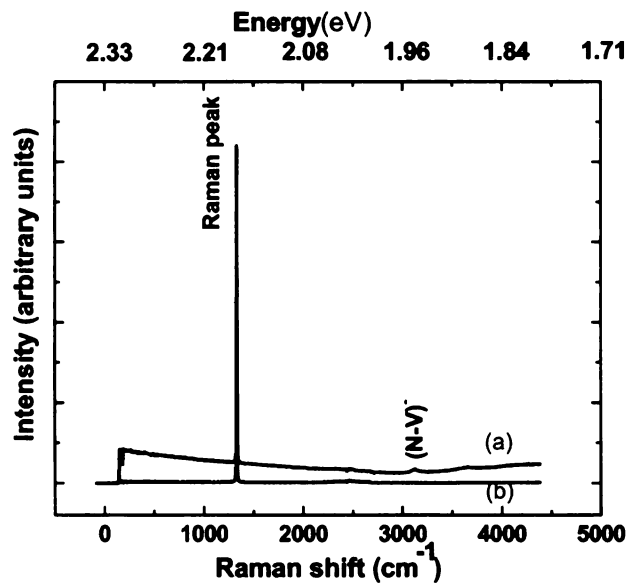


Figure 6.23 Spectra of Type Ib diamond substrates (a) broad background and weak (N-V) peaks, (b) no background and no (N-V) peaks.

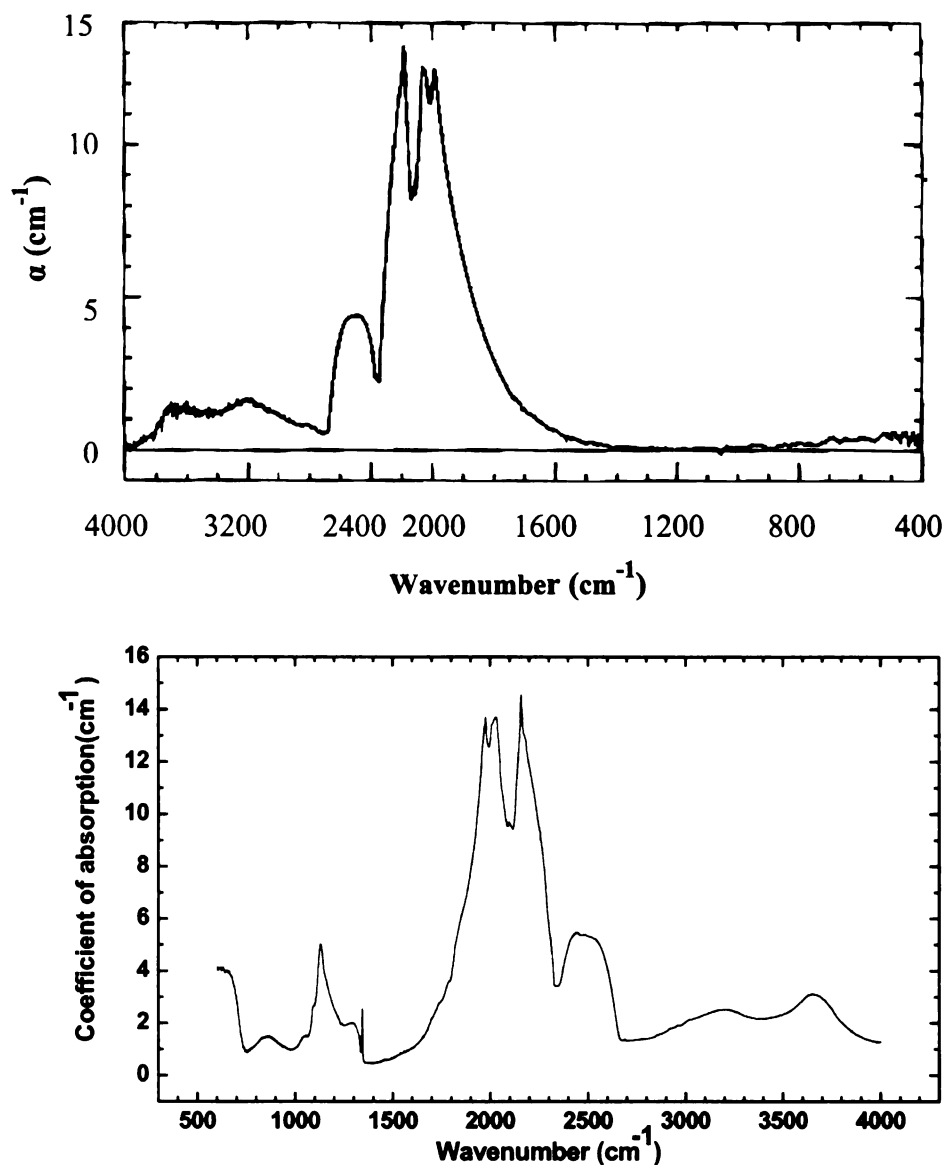


Figure 6.24 FTIR spectrum of diamond (a) natural Type IIa (b) Type Ib. Substitutional nitrogen absorption peaks appear at 1130 cm^{-1} and 1344 cm^{-1} in (b).

Substrates were also studied by Fourier Transform Infrared Spectrophotometry (FTIR) using a Matson-type FTIR instrument with resolution 0.4 cm^{-1} between 600 and 4000 cm^{-1} . The measurement was made with the samples at room temperature. Figure 6.24 shows the FTIR spectrum of a HPHT substrate together with a natural type IIa

diamond with very low level of impurities. It shows two absorption peaks, a broad one at 1130 cm^{-1} and a sharp one at 1344 cm^{-1} which indicate the presence of substitutional nitrogen. Above 2800 cm^{-1} , two and three-phonon absorption bands characteristic of diamond appear.

The (004) X-ray linewidth of several substrates was measured with the Bruker instrument, using the $0.154\text{ nm Cu K}_\alpha$ line, and a Ge monochromator with instrumental resolution 0.0014 deg . Figure 6.25 shows a (004) rocking curve for a Type Ib crystal, yielding a total linewidth of $1.8 \pm 0.1\text{ mdeg}$, uncorrected for instrumental broadening

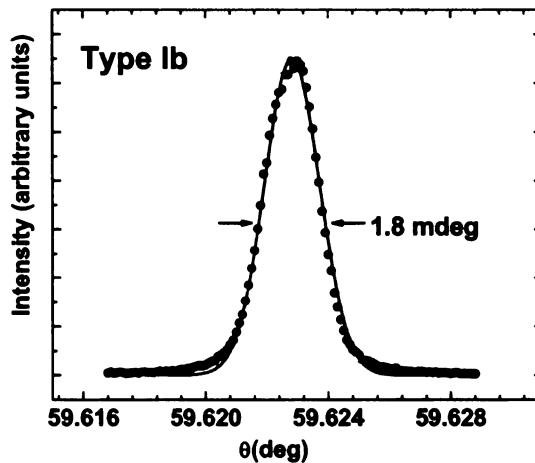


Figure 6.25 X-ray (004) rocking curve linewidth of a Type Ib diamond substrate

6.2.4.2 CVD epilayers

Diamond epilayers grown at $r = 4\text{--}8\%$ and $T_g = 750\text{--}880\text{ }^\circ\text{C}$ were examined with the Raman instrument. In the growth process, no nitrogen was added intentionally and the growth chamber was evacuated for the same amount of time before starting. The base

pressure and the nitrogen partial pressure were monitored before growth to insure no external leaks.

Diamond grown with $r = 4\%$ showed no (N-V) PL for $T_g = 770-880\text{ }^\circ\text{C}$. Only one exception to this observation occurred, where a very weak (N-V) PL was observed for a crystal grown at the initiation of homoepitaxial experiments when small leaks into the growth chamber might have been present. Similarly, growth at $r = 6\%$ and $T_g = 800\text{ }^\circ\text{C}$ showed no (N-V) emission as was the case at $r = 7\%$ with $T_g = 880\text{ }^\circ\text{C}$. Figure 6.26 shows spectra taken from these three diamond crystals. No luminescence background or (N-V) ZPL lines are evident even after 20x magnification (b) where the second-order Raman spectrum is easily seen.

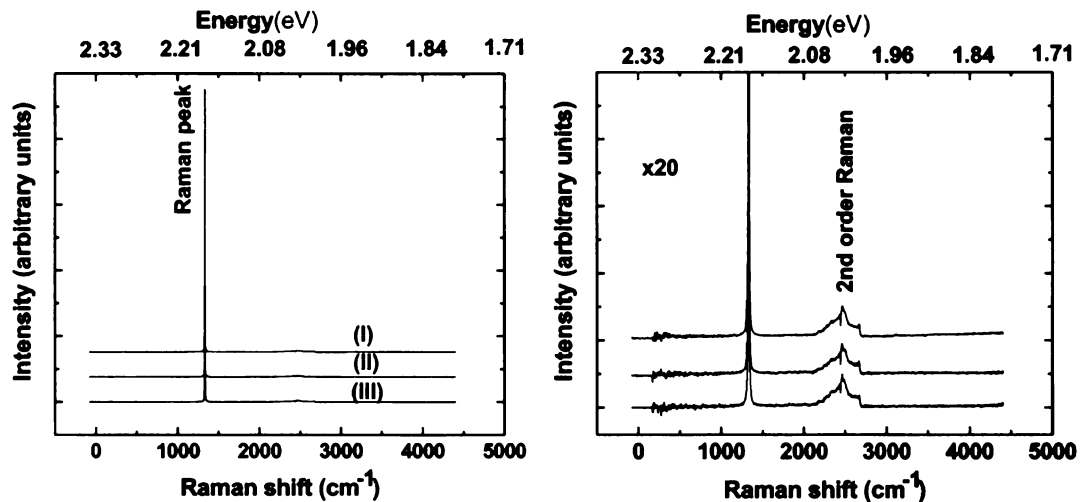


Figure 6.26 (a) Raman spectra taken from CVD homoepitaxial diamond grown at different conditions: (I) $r = 4\%$, $T_g = 770\text{ }^\circ\text{C}$; (II) $r = 6\%$, $T = 800\text{ }^\circ\text{C}$; and (III) $r = 7\%$, $T = 880\text{ }^\circ\text{C}$. (b) Data in (a) is magnified 20x. No (N-V) related PL is observed.

At higher methane concentrations, however, with $r = 7-8\%$, (N-V)-related PL was observed for $T_g \leq 800\text{ }^\circ\text{C}$. Furthermore, evidence was discovered that the charge state of

the (N-V) center depends on growth conditions. With $T_g = 750-770$ °C, the intensity ratio, $I(N-V)^0$ to $I(N-V)^-$, was found to be greater than 1, whereas close to 800 °C the ratio was unity or less than 1.

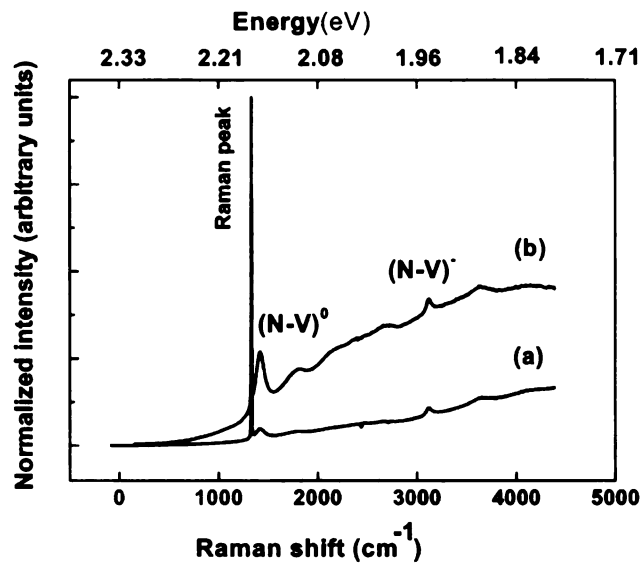


Figure 6.27 Raman spectra of CVD diamond crystals grown at 770 °C (a) $r = 7\%$ (b) $r = 8\%$, PL luminescence from (N-V) centers are observed with 532 nm excitation.

Figure 6.28 summarizes the results of PL spectra from 22 different CVD diamond crystals plotted in the $T_g - r$ plane. Three regions in the parameter space are identified on the basis of (N-V) PL intensity. There is a clear delineation between the region with no (N-V) PL intensity at high T_g and low r , and the remaining part of the diagram. In the region where PL intensity is seen, it is found that $I(N-V)^0 > I(N-V)^-$ at the lower growth temperatures.

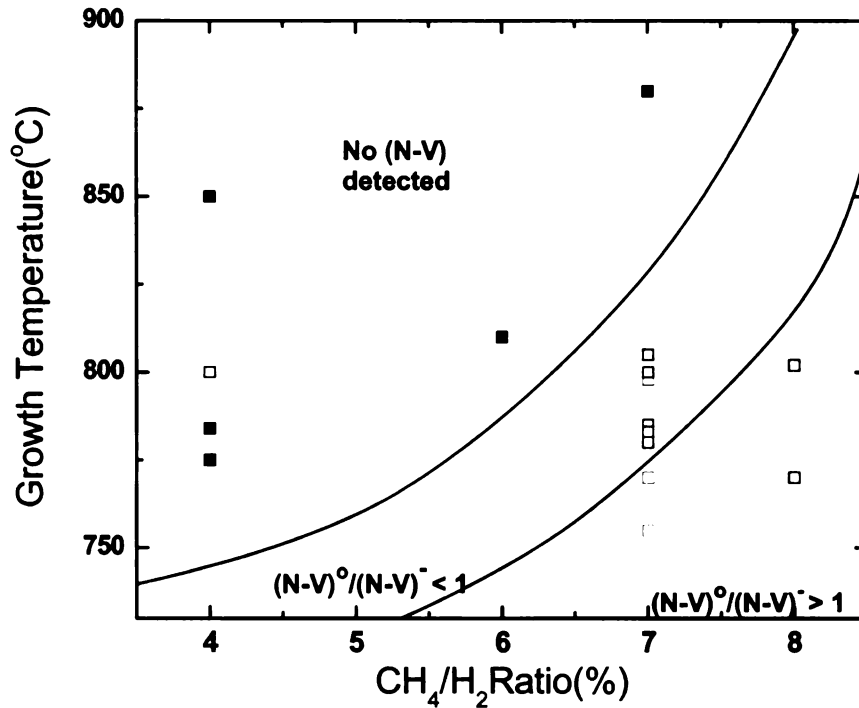


Figure 6.28 Graph showing three different regions in T_g - r space; no I(N-V), $I(N-V)^0/I(N-V)^-<1$ and $I(N-V)^0/I(N-V)^->1$.

Table 6.7 PL intensities from (N-V) centers in CVD diamond grown under different conditions, relative to the diamond Raman peak height.

T_g (°C)	r (%)	$I(N-V)^0/I_R$	$I(N-V)^-/I_R$
770	4	0	0
880	4	0	0
800	6	0	0
880	7	0	0
780	7	0.048	0.021
750	7	0.055	0.030
770	7	0.030	0.023
800	7	0.003	0.005
800	7	0.004	0.005
770	8	0.135	0.003
780	7	0.023	0.014

(N-V) PL intensities from a subset of the diamond crystals used in this study are listed in Table 6.7. The ZPL intensities are given in units relative to the 1332 cm^{-1} Raman peak intensity (I_R).

6.2.4.3 Effect of nitrogen

To study how nitrogen influences growth rate and (N-V) PL intensities, diamond was grown in stages with 0, 10 and 50 ppm nitrogen deliberately introduced into the H_2 feed gas. As is well known [13,123,128,168], small amounts of nitrogen greatly enhance diamond growth rates, as confirmed in Figure 6.29.

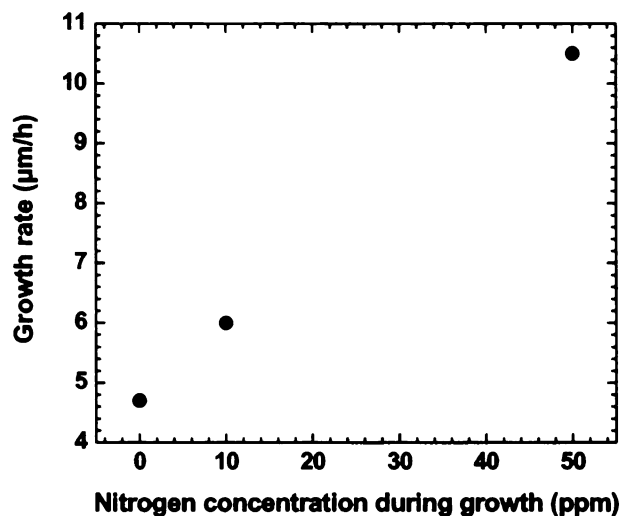


Figure 6.29 Growth rate vs. nitrogen concentration (relative to H_2).

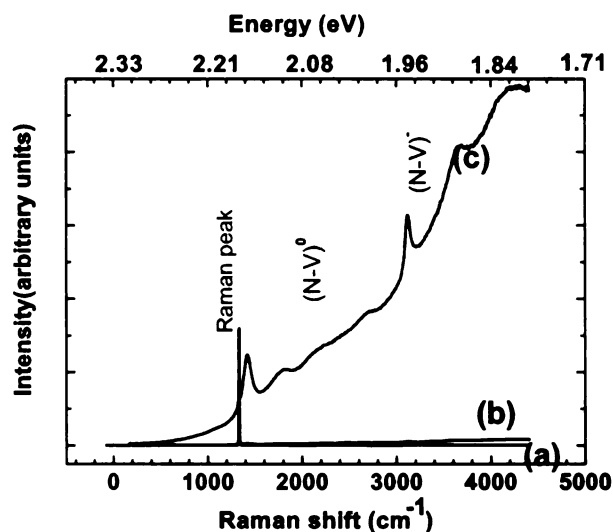


Figure 6.30 Room temperature spectra excited at 532nm for diamond grown with N₂ in feed gases: r_N = (a) 0 (b) 10 (c) 50 ppm.

Spectra taken at room temperature under identical conditions with 532 nm laser excitation after each growth step are shown in Figure 6.30. With 10 ppm nitrogen added, (N-V) and background luminescence noticeably increased above the levels for the nominally undoped crystal. At 50 ppm, the luminescence background became almost as intense as the diamond Raman peak. Figure 6.31 shows a plot of (N-V) peak intensities, after background subtraction, vs. feed gas nitrogen concentration. Although there are not enough data to extract the functional form of the $I(\text{N-V})$ nitrogen concentration relation, it is clear that there is a supra-linear dependence.

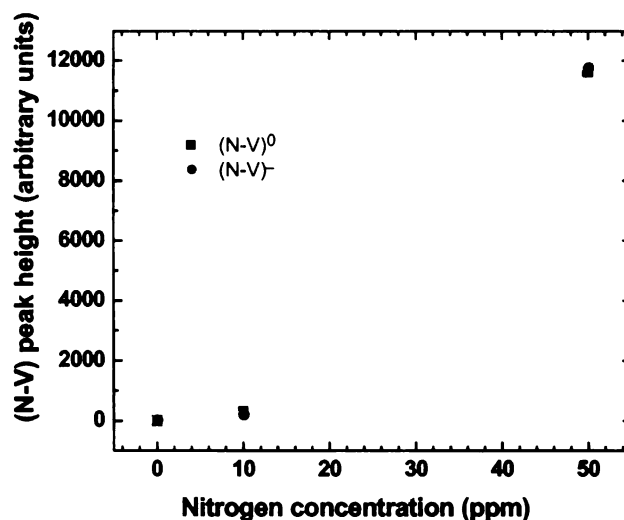


Figure 6.31. (N-V) PL peak heights, after background subtraction for different nitrogen concentrations during growth.

6.3 *Homoepitaxial diamond characterization*

6.3.1 High resolution x-ray diffraction

Figure 6.32(a) shows a (004) rocking curve for crystal A₁₀. The linewidth was extracted by performing an unweighted, least-squares fit of a Gaussian function to the data, assuming a flat background. The linewidth is 2.1 ± 0.1 mdeg. For comparison, Figure 6.32(b) shows the same measurement for the Type Ib substrate. The measurements were taken in consecutive scans with no adjustment of the monochromator between scans. However, owing to the miscut angle of the substrate, the absolute line positions are not accurate, since the goniometer position was changed for different crystals. The linewidth for the substrate (004) reflection is 1.8 ± 0.1 mdeg. In general, XRD linewidths this narrow are found only for strain-free, nearly perfect crystals, such as Si or Ge grown by float zone methods, or molecular-beam epitaxy grown films such as GaAs. This

linewidth value is lower than previously reported for CVD homoepitaxial diamond [13, 169, 170].

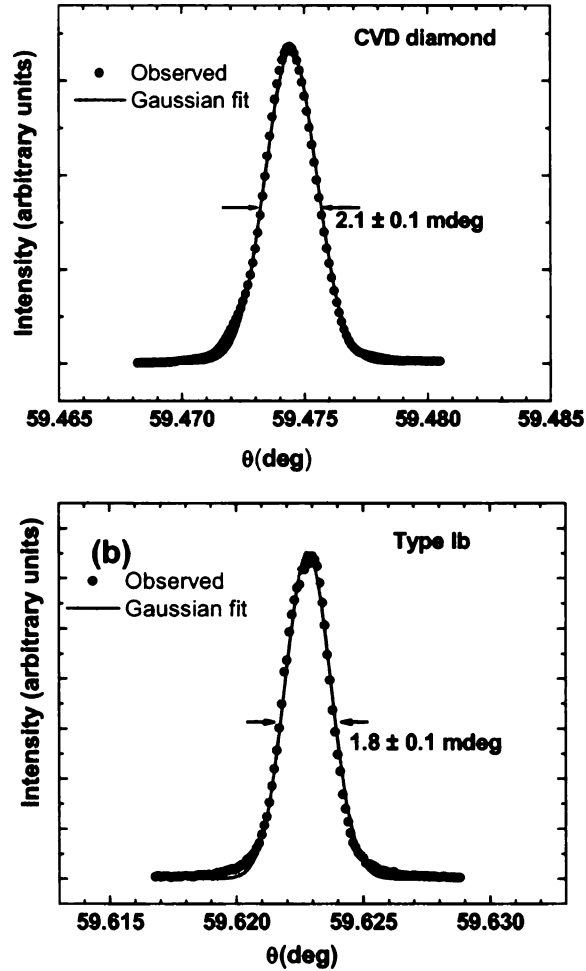


Figure 6.32 X-ray rocking curve for the (004) reflection of (a) CVD homoepitaxial diamond crystal A₁₀ (b) a HPHT Type Ib substrate.

To establish that the diamond grown was actually a single crystal, an XRD pole figure scan was made. This measurement examines how similar reflections transform under rotation. Figure 6.33 shows an x-ray (111) pole figure of sample A₁₀. Four (111) reflections appear at angular rotations (φ) of 45, 135, 225 and 315 deg, as expected for a

diamond single crystal. The difference in peak intensities arises from slight misalignment. The logarithmic scale shows the dynamic range of the measurement and the signal to noise ratio.

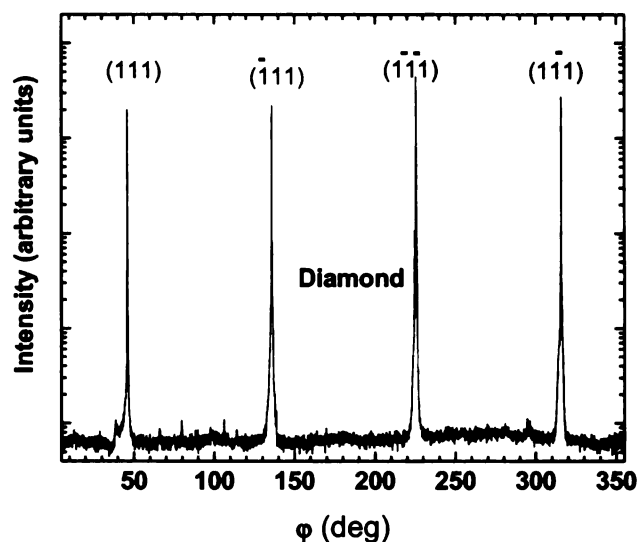


Figure 6.33 X-ray (111) pole figure from homoepitaxial CVD diamond film. The intensity axis is logarithmic.

6.3.2 Raman spectroscopy

Diamond sample A₁₀ was studied by Raman spectroscopy using 532 nm laser excitation at room temperature. The Raman spectrum for this sample is shown in Figure 6.34(a). The first-order Raman shift appears at 1332.6 cm⁻¹. The second order Raman peak can be clearly seen after 20x magnification in Figure 6.34(b). No luminescence background or nitrogen-related PL can be detected with the present sensitivity.

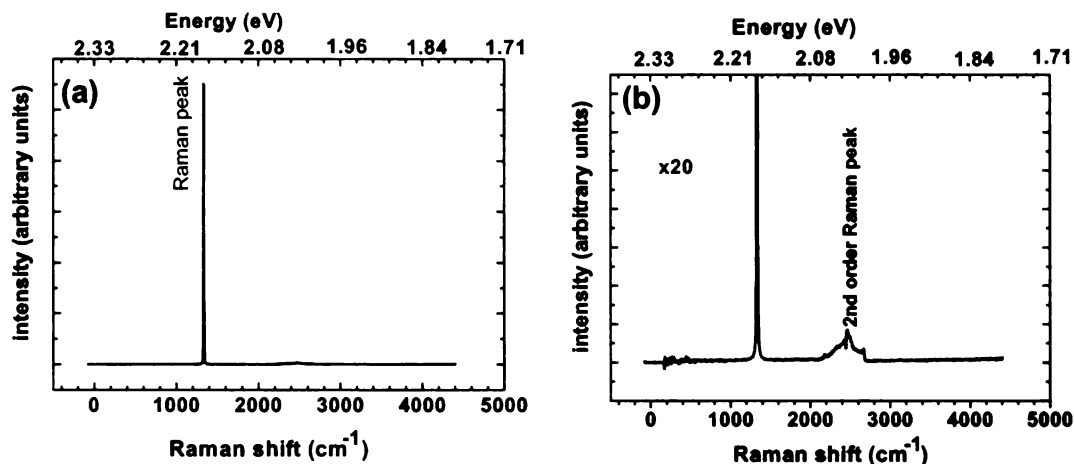


Figure 6.34 (a) Raman spectrum of sample A₁₀ taken at room temperature using 532 nm laser excitation (b) after 20x magnification. Note the complex line shape of the second-order Raman peak near 2665 cm⁻¹.

The Raman linewidth could not be directly measured because of the finite instrumental resolution of the spectrometer grating. It is known that the spectrometer resolution is approximately 1 cm⁻¹. This was confirmed by measurements on a reference sample of high-purity, high-quality Type IIa diamond, where the standard value of the Raman linewidth at room temperature is 1.65 cm⁻¹ [143]

Figure 6.35 shows the vicinity of the 1332 cm⁻¹ Raman line for (a) CVD sample A₁₀, (b) HPHT substrate diamond, and (c) a Type IIa natural diamond crystal. A Lorentzian function was fit to the experimental data. The fit results for the linewidths are: (a) CVD sample A₁₀, 2.55 cm⁻¹ (b) Type Ib substrate, 2.64 cm⁻¹, and (c) Type IIa, 2.60 cm⁻¹. Since the actual resolution function is not known, it was not possible to deconvolve the diamond spectra to obtain the true linewidth. However, the actual linewidth can be estimated by subtracting the instrumental resolution from the values measured for the

three samples. It appears that all samples are nearly indistinguishable and very close to the value of 1.65 cm^{-1}

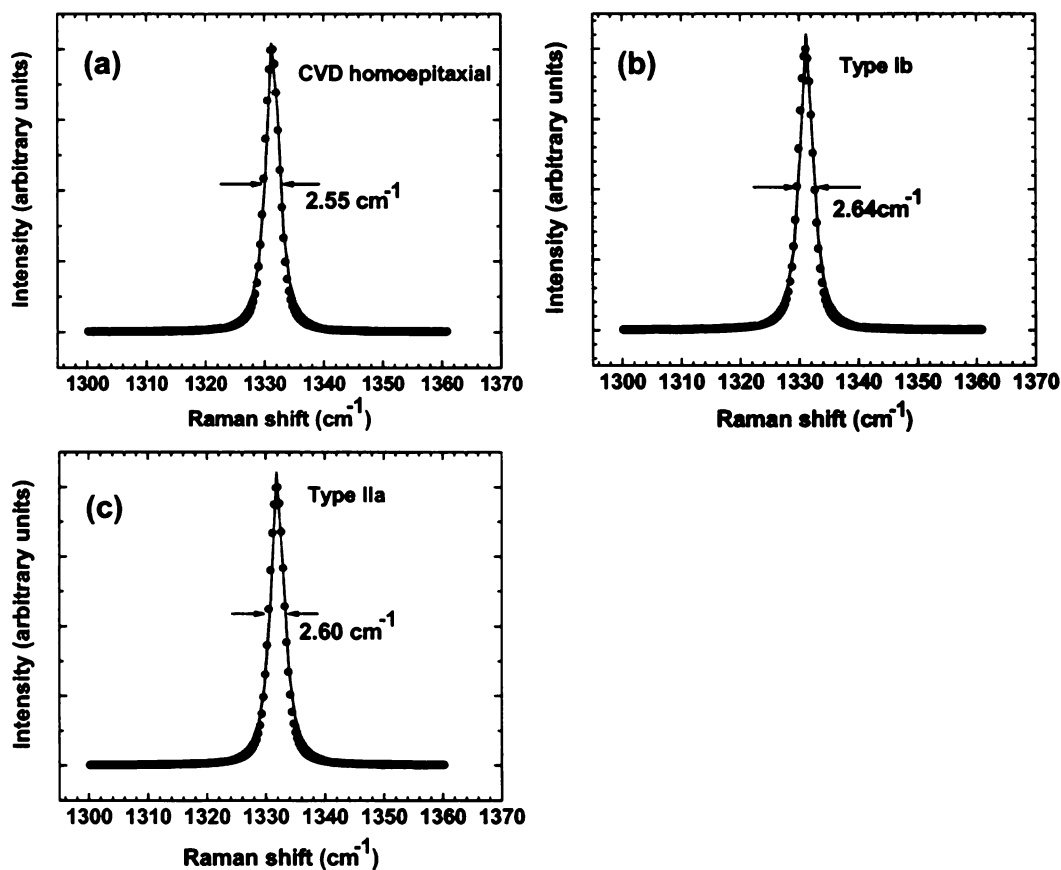


Figure 6.35 Raman spectra and Lorentzian fits for (a) CVD homoepitaxial diamond A₁₀ (b) HPHT homoepitaxial substrate (c) Type IIa natural diamond. The Raman spectrometer increases the linewidth by approximately 1.0 cm^{-1} .

6.3.3 Fourier transform infrared spectrophotometry (FTIR)

CVD diamond samples A₈ and A₉ were examined by FTIR at room temperature. The results for these CVD crystals can be compared to the HPHT substrates, which have about 100 ppm of substitutional nitrogen. Absorption spectra are shown in Figure 6.36. The substrate shows substitutional nitrogen peaks at 1130 cm^{-1} and 1344 cm^{-1} . Both

CVD crystals show weak absorption peaks at 1344 cm^{-1} , as seen with higher magnification in Figure 6.37(a). Weak hydrogen-related absorption can be observed at 2800 , 2960 and 3020 cm^{-1} , as shown in Figure 6.37(b). These peaks are due to C-H stretching modes, indicating the presence of small quantity of hydrogen in the film [31,171].

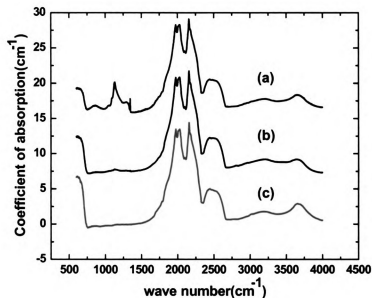


Figure 6.36.FTIR spectrum of diamond crystals (a) Type Ib (b) CVD diamond A₈ (c) CVD diamond A₉. Type Ib diamond shows strong absorption at 1130 cm^{-1} and 1344 cm^{-1} , but for CVD diamond the absorption peaks are difficult to see on this scale. Vertical scale is shifted by arbitrary amount for clarity

Now we use the results of Kiflawi et al. [172] to set an upper limit on the nitrogen concentration in the CVD diamond. They reported that 25 ± 2 ppm of single substitutional nitrogen produced 1 cm^{-1} absorption at 1130 cm^{-1} . Using this calibration factor, the nitrogen concentration in a 0.5 mm thick HPHT Type Ib substrate is 120 ppm.

Using the same calibration factor for CVD diamond crystal A₈ the concentration is 9 ± 1 ppm, However, it is known that this crystal has at least 35 μm of substrate attached. The residual substrate material contribution is thus 8 ± 1 ppm of nitrogen. This leads to an upper limit for nitrogen in the CVD diamond crystal of 2 ppm. Diamond crystal A₉ does not show a peak at 1130 cm^{-1} but at 1160 cm^{-1} . The source of this weak absorption peak is not clear, but there is evidently very little nitrogen.

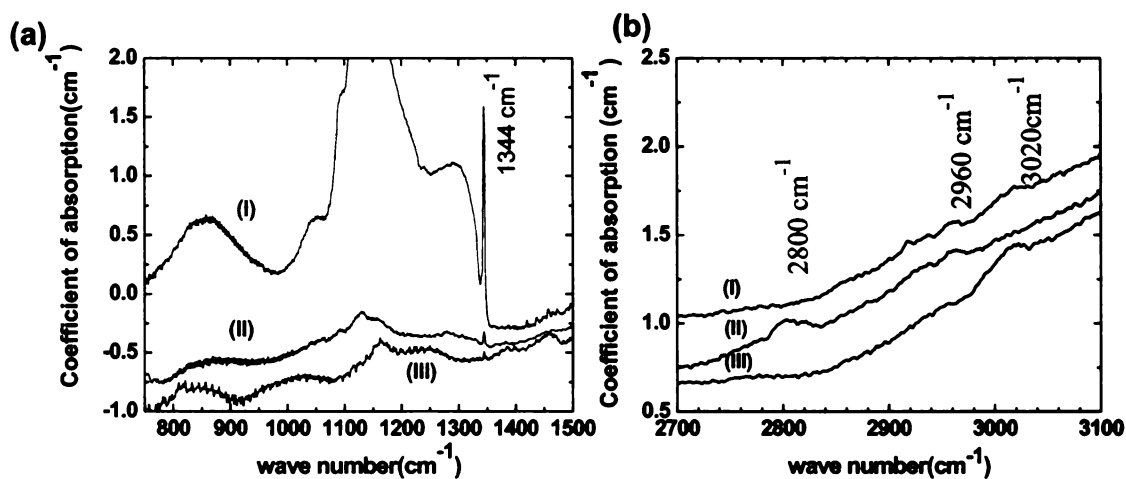


Figure 6.37 Magnified FTIR absorption spectra of (I) Type Ib substrate (II) CVD diamond sample A₈ (III) CVD diamond A₉. (a) Region near 1344 cm^{-1} (b) region with C-H absorption bands at 2800 , 2960 and 3020 cm^{-1} . Vertical scale is shifted by arbitrary amount.

6.4 Discussion

In summary, experiments on homoepitaxial growth have led to a better understanding of the roles of various important growth parameters. Examination of the effect of plasma etching of substrates prior to homoepitaxial growth, led to methods that reduced, or eliminated, the propagation of defects from substrate to diamond epilayer.

Several highly perfect homoepitaxial crystals were grown, as evidenced by their narrow x-ray and Raman linewidths.

By studying the (N-V) PL intensities for crystals grown under differing reactor conditions, we were able to map regions in the growth temperature-methane concentration space in which no N-V centers could be detected by optical emission. Furthermore, there appeared to be regions in this space which were favorable to formation of either neutral or negatively-charged N-V centers. These results suggest that growth temperature and methane concentration are not independent variables in forming nitrogen-vacancy complexes. The situation is quite complicated, but it is likely that vacancy concentrations will be quite sensitive to growth temperature. On the other hand, the vacancies must become associated with a single N impurity, also implicating vacancy diffusion dynamics. It is also a possibility that the major effect of increased methane concentration is to increase growth rate, thereby introducing greater vacancy concentrations for the same growth temperature. Recent work showed lower N-V concentrations for growth at 950 °C compared to 875 °C [173]. The interpretation given was that less nitrogen was incorporated into diamond as growth temperatures increased.

The x-ray examination of CVD diamond crystals found extremely narrow x-ray linewidths, comparable to the best crystals of any substance. Also, Raman widths for CVD material were superior to those from high-purity natural diamond. With the use of FTIR, it was possible to set limits on the total amount of nitrogen incorporated into CVD diamond grown with high-purity gases to no more than 2 ppm. This result is encouraging as it suggests that the present process should be able to produce detector-grade diamond for use as high-speed, energetic particle detectors.

7 Chapter 7 Discussion and conclusions

During the course of this research, the growth of single crystals of diamond has been investigated by heteroepitaxy and by homoepitaxy. The initial motivation for heteroepitaxial diamond growth was based on the premise that large area, diamond substrates could be produced by a CVD process. In this work, the diameter of (001) diamond thin films has been increased from 3.5 mm to 8 mm. Although not yet at the wafer scale, many of the insights derived from this work are pointing the way to achieving larger and better quality diamond. The rationale for pursuing homoepitaxial growth has also been justified by the production of essentially defect-free, high-purity diamond single crystals. It is worth noting that the $3.8 \times 3.8 \times 0.5 \text{ mm}^3$ crystal represents about 1/8 carat of diamond, where the carat (ct) is defined as 200 mg. The knowledge obtained in developing the homoepitaxial process has been helpful in devising the two-step process for heteroepitaxy, where the second step is essentially a variant of the process used for high-rate, homoepitaxial growth.

Some of the major conclusions of this research work can be summarized as follows:

1. The biasing process for enhancing diamond nucleation on Ir is a complex etching process. The appearance of highly correlated Ir nanopillars originates in the self-organization of facets on the [110] step edges of (001) Ir. As etching proceeds, the facets develop into the isolated nanopillars, which protrude above the Ir surface 3-4 nm. The pillars attract the plasma, which propagates across the Ir surface, leaving etched regions of pillars in its path. An incubation period, lasting about 5

min, has been explained as the time interval required for the secondary plasma to form at the center of the biased substrate. High densities of nanopillars are associated with high densities of diamond nucleation sites.

2. HRTEM images have revealed atomic-scale details of the interface between diamond and Ir. True epitaxy occurs, with misfit dislocations forming within 0.3 nm of the interface. No evidence for diamond nucleation occurring on (001) Ir surfaces was seen. Thus, the role of biasing may be simply to expose higher index planes which may be more favorable to diamond nucleus formation.
3. Earlier work with the same biasing process led to the suggestion that nucleation of diamond does not occur while the bias process is operative [140]. This idea contradicted the standard view that nucleation and growth proceeds throughout the bias period. However, by viewing HRTEM images of Ir surfaces subsequent to the bias process, for time intervals up to 150 s, it was seen that diamond crystals do not emerge until roughly a minute after bias ceases.
4. In homoepitaxial diamond growth, diamond crystals exhibit x-ray linewidths which are among the narrowest observed for any crystal, at the limit of resolution of the x-ray spectrometer. With high-purity feed gases, the nitrogen-related impurity centers can be limited to the ppm level or less. Again, the ability to measure impurity concentrations is at the limit of the available instrumentation.

7.1 *Suggestions for future work*

In heteroepitaxy, two-step growth was found to be a viable method for producing diamond. By changing the sample holder geometry so that the secondary plasma uniformity is increased, it should be possible to significantly increase the diamond

nucleation area. However, the cracking of the SrTiO₃ substrate needs to be eliminated. More attention should be paid to Ir growth on Al₂O₃. Since Al₂O₃ is stronger than SrTiO₃, it can survive greater stresses and is more resistant to reduction by the plasma.

In homoepitaxial growth, nitrogen-related defects can be further reduced by using higher purity feed gases and by selecting the appropriate growth parameters from the T_g-r map prepared during this work. Plasma uniformity should be improved so that a uniform vertical growth rate occurs. This can be done with the present CVD reactor by geometrical changes in the vicinity of the sample. Higher microwave power could be advantageous if efficient cooling of the substrate is provided.

There are many applications for high-quality diamond. A particularly attractive one is in particle detection. Crystals of heteroepitaxial diamond were used at the NSCL to detect relativistic heavy ions. Sub-ns response times were observed [23]. Application to beam tracking would be appropriate for thin diamond films since diamond is insensitive to radiation damage.

Another application is for fission neutron detection. In the spectral range where energy loss is by nuclear recoil, diamond possesses the greatest sensitivity to neutrons of any semiconductor, with over 4% of the fast neutrons interacting per mm. Besides the low carbon mass, this property originates in the short sp³ C-C bond length, only 0.154 nm. The resultant three-dimensional tetrahedral coordination of the diamond cubic structure leads to the highest elemental packing density; the strong bonding produces extremely high resistance to radiation damage. Furthermore, the low Z of carbon yields the lowest photoelectric cross-section in this group of semiconductors. This is useful in

discriminating against gamma emission. The diamond crystals produced in this research should be seriously considered for these, and similar, particle detection applications.

8 Appendix A

8.1 Sample information

8.1.1 Heteroepitaxial sample information

Figure no	Sample no	Date	Comments
5.13 (a)	03-09-06-17-2	08-12-06	$t_b = 0$ min
5.13 (b)	03-09-06-15-2	08-21-06	$t_b = 5$ min, $t_g = 0$ min
5.13 (c) & (d)	08-10-06-1-2	08-20-06	$t_b = 20$ min, $t_g = 0$ min
5.14 (e) & (f)	12-20-05-11-2	02-25-06	$t_b = 60$ min, $t_g = 0$ min
5.15 (a)	03-09-06-16-4	08-03-06	$t_b = 10$ min, $t_g = 20$ min
5.16 (a)	08-10-06-1-3	08-28-06	$t_b = 5$ min, $t_g = 20$ min
5.16 (c) & (d)	03-09-06-16-1	08-02-06	$t_b = 20$ min, $t_g = 20$ min
5.18 (a)	12-20-05-11-4	02-28-06	$t_b = 60$ min, $t_g = 7$ s
5.18(b)	12-20-05-11-3	02-26-06	$t_b = 60$ min, $t_g = 3$ s
5.18(c)	12-20-05-12-1	03-02-06	$t_b = 60$ min, $t_g = 60$ s
5.18(d)	03-09-06-16-2	07-31-06	$t_b = 60$ min, $t_g = 90$ s
5.18(e)	03-0-06-14-3	08-08-06	$t_b = 60$ min, $t_g = 120$ s
5.18(f)	08-10-06-1-1	08-16-06	$t_b = 60$ min, $t_g = 150$ s
5.23	09-13-06-10-1	09-21-06	$t_b = 60$ min, $t_g = 3$ h
5.24	08-10-06-2-2	09-06-06	$t_b = 60$ min, $t_g = 3$ h
5.25	08-10-06-6	12-14-06	$t_b = 60$ min, $t_g = 3$ h
5-27 & 5-28	03-09-06-13-3	07-06-06 to 10-20-06	65 μ m thick hetero diamond

8.1.2 Homoepitaxial sample information

Figure or No. in thesis	Sample no	Start date	Last date
6.7 (a)	S1-52-2	04-01-06	04-04-06
6.7 (b)	S1-52-1	03-22-06	03-26-06
6.8 (a)	S1-53-4	05-29-06	06-06-06
6.8(b)	S1-53-1	04-30-06	05-02-06
6.9	S1-25-1	10-03-06	10-17-06
6.10	S1-25-2	02-15-07	03-05-07
A ₁	S1-51-4	03-14-06	03-16-06
A ₂	S1-52-1	03-22-06	03-26-06
A ₃	S1-52-2	04-01-06	04-04-06
A ₄	S1-52-4	04-12-06	04-15-06
A ₅	S1-53-3	05-10-06	05-19-06
A ₆	S1-54-2	06-15-06-	06-21-06
A ₇	S1-53-04	05-29-06	06-06-06
A ₈	S1-25-1	10-03-06	10-17-06
A ₉	S1-25-6	11-01-06	12-20-06
A ₁₀	S1-25-15	07-19-07	07-29-07

9 Appendix B

9.1 *Pyrometer calibration*

The Williamson type two-color pyrometer works by calculating the ratio of its intensity at two wavelengths, 2.4 and 2.2 μm . Temperature measurement based on two wavelengths eliminates the need for an absolute emissivity measurement. In contrast, a single color pyrometer requires knowledge of the surface emissivity coefficient.

It was first used in the sputtering system to measure the temperature of the Ir surfaces and was compared with the single color pyrometer measurement. In this measurement two-color pyrometer measurement was about 250 $^{\circ}\text{C}$ higher than the single color measurement, which was quite puzzling. Then we tried to measure the temperature of an alumina boat inside a tube furnace. It measured about 300 to 400 $^{\circ}\text{C}$ higher than an R type (Pt-Rh) thermocouple (TC), calibrated against the gold melting point. This result was very puzzling and similar to that of the sputtering system measurement. We considered the following argument. The alumina tube in the furnace is transparent so that the radiation from the heating elements, that are much hotter than the specimen, would actually radiate inside the tube leading to the specimen reflecting this radiation to the pyrometer. Thus, the pyrometer would be sensing the heating element temperature. This also explained measurement inconsistencies in the sputtering system. Here, the sample holder contained small holes allowing radiation from the heater to have a direct path to the pyrometer. To address this problem, four layers of optically opaque furnace tubes were used as inserts for the outer quartz tubes. Now, with the pyrometer focused on the closed end of the innermost mullite tube the pyrometer read within ± 10 $^{\circ}\text{C}$ of the thermocouple.

This confirmed that our previous explanation was indeed correct. Figure 9.1 shows the plot of the pyrometer- and the thermocouple-based temperature scales.

In the CVD system the signal from inside the growth chamber passes through a quartz window which could affect the pyrometer. By inserting a spare window before the pyrometer, we found that the pyrometer measured more than 100 °C lower than without the window.

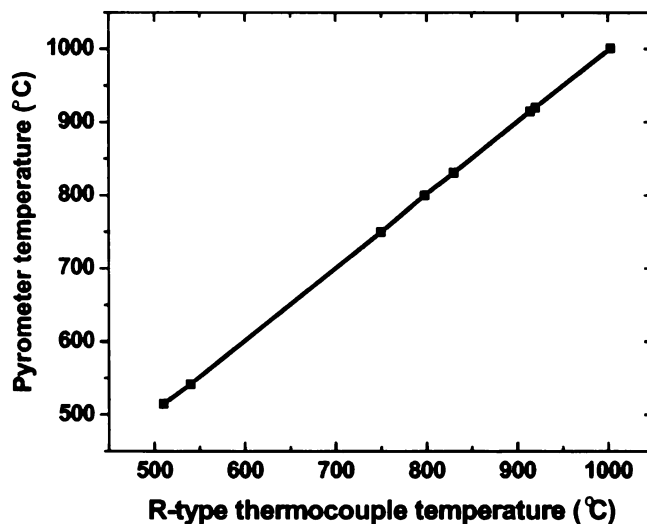


Figure 9.1 Pyrometer temperature vs R Type thermocouple temperature

This confirmed that the quartz plate has a strong effect in the temperature measurement. Hydroxyl ions, if present in fused quartz, have absorption bands in the near-ir. Figure 9.2 shows the pyrometer and the TC measurement in this case. A GE 124 quartz plate that contains less than 10 ppm OH was available. Figure 9.2 shows the pyrometer temperature vs. the R Type TC temperature with these two different quartz plates in place. Temperature measured with the GE 124 quartz plate was just about 10-15 °C lower than the TC temperature. In the pyrometer there is a correction method defined

as the E-slope offset correction, which changes the ratio of the wavelengths by a constant factor.

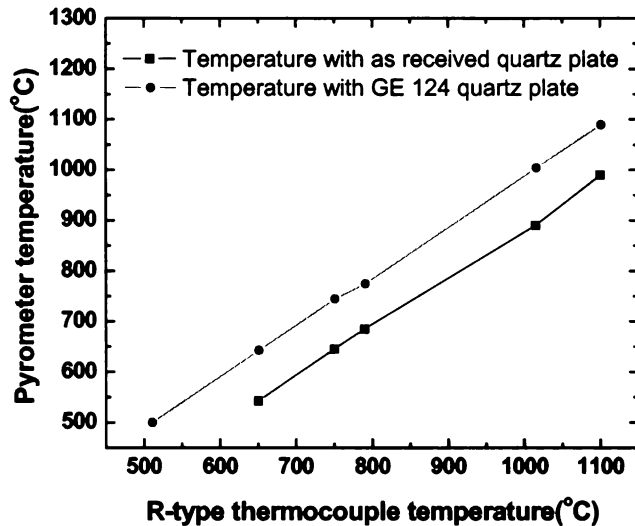


Figure 9.2 Pyrometer and TC temperature with 2 kinds of quartz plate

E slope offset correction was applied to correct the temperature measurement with the quartz plate in place. The factor was found to be -0.036 for the as received quartz plate and -0.004 for the GE 124 quartz plate. Figure 9.3 shows the temperature measured by the pyrometer after the correction factor was used. This measurement was consistent with the temperature without the correction factor and the quartz plate.

After this correction, the temperature measurement was correct within ± 10 °C with the temperature measured without the quartz plate and the E-slope offset. This measurement suggested that the E-slope offset works. Nevertheless, it was necessary to calibrate the reactor pyrometer in the presence of the OH-containing quartz window.

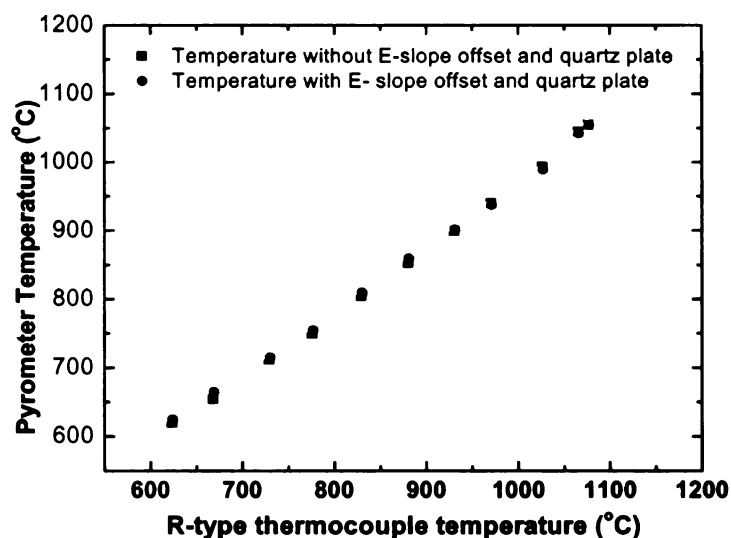


Figure 9.3 Pyrometer temperature with and without quartz plate

To calibrate inside the reactor, the two-color pyrometer was focused on a gold foil on the sample stage. The foil was then heated with a hydrogen plasma until it melted. The temperature at which gold melted was recorded as 960 °C. The E-slope correction factor required to bring it to 1065 °C, the gold melting point, was -0.022. This correction factor is actually smaller than the previous correction factor. This might be because the two quartz plates are different or the measurement in the presence of the plasma is different.

After this calibration, the two-color pyrometer was focused on a diamond sample from the top. A single color pyrometer, which was already calibrated in the furnace with a thin quartz window, was focused on the sample from the side window. In this case the two-color pyrometer was fluctuating about ± 50 °C, so that the temperature shown in Figure 9.4 is the average temperature measured. In contrast, the temperature measured by the single color pyrometer was very stable.

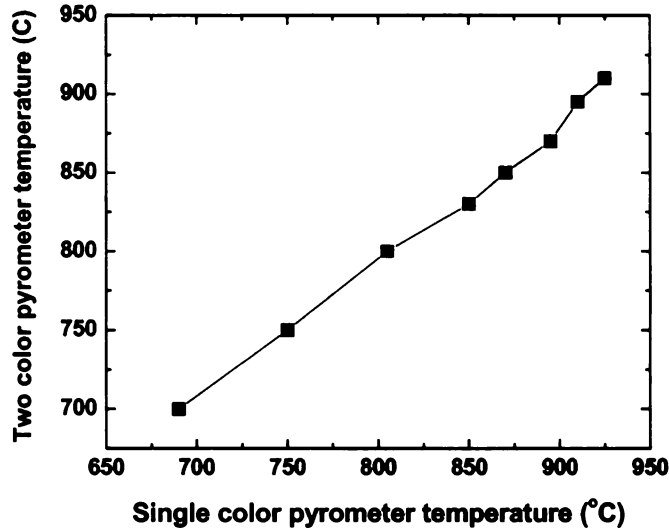


Figure 9.4 Two-color vs. single color pyrometer temperature on diamond sample

Figure 9.4 shows the temperature measured by the two pyrometers focused on a diamond sample at different microwave power. This measurement agrees to within ± 25 °C.

Since the two-color pyrometer was fluctuating about ± 50 °C, temperature measured by the single color pyrometer was considered to be the more accurate. Most of the time the difference between the two and the single color pyrometer measurement is within ± 50 °C, but in some growth runs the temperature measured by the two-color pyrometer could be as much as 100 °C higher than the single-color measurement. This could be attributed to small variations in sample geometry.

10 Appendix C

10.1 *Ir growth on Al₂O₃*

10.1.1 Al₂O₃ preparation

Two inch diameter 0.5 mm thick (11 $\bar{2}$ 0) Al₂O₃ substrates having 1.3 deg vicinal angle rotated about the m-axis and epi-polished on one side were purchased from Substrates Technology (Russia). Two standard sizes were prepared: 10x10 mm² and 5x5 mm². As-received wafers were coated with photoresist and cut with a dicing saw. Each piece was solvent-cleaned and degreased to remove photoresist and particulates. After optical inspection the substrates were annealed in a tube furnace at 1400 °C in air for 15 hours.

A typical surface structure after annealing is shown in Figure 10.1. The topography depends on the vicinal angle and miscut direction. In contrast to SrTiO₃, the (11 $\bar{2}$ 0) Al₂O₃ surface for this vicinal angle does not show a simple reconstruction. In fact, the terraces are separated by steps of 4-6 unit cells height. For other vicinal cuts, different surface reconstructions have been observed [11]. The reconstruction depends on annealing temperature and may also depend on the gaseous environment.

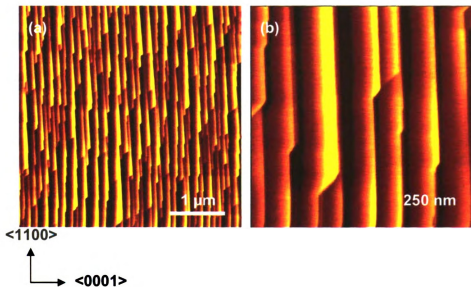


Figure 10.1 Topography of vicinal $(11\bar{2}0)$ Al_2O_3 surface after annealing in air at 1400°C for 15 hours.

10.1.2 Ir growth on Al_2O_3

Ir growth was carried out on vicinal $\alpha\text{-Al}_2\text{O}_3$ substrates. The temperature, thickness, and Ar gas pressure were systematically varied to optimize growth. In general, both (001) and (111) Ir grains grow on Al_2O_3 , but it is possible to suppress (111) growth considerably. Figure 10.2 shows the topography of a 500 nm thick Ir film grown on Al_2O_3 at 800°C , with 3 nm/min deposition rate and 12 mTorr Ar pressure. The topography is quite different from Ir on SrTiO_3 . Alignment of the elongated structures in this case is along the $\langle 1100 \rangle$ direction. Mean roughness is 0.8 nm, almost 3 times greater than for Ir on SrTiO_3 .

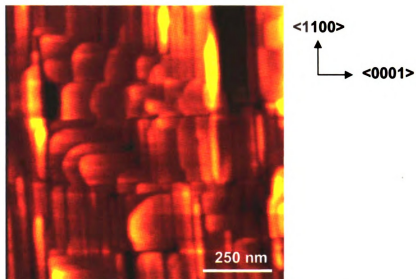


Figure 10.2 Topography of 500 nm thick (001) Ir surface grown on vicinal α - Al_2O_3 surface at 800 °C, 3 nm/min deposition rate and 12 mTorr Ar gas pressure.

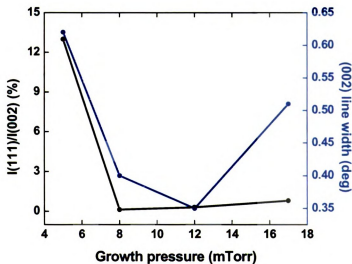


Figure 10.3 Plot of (002) Ir linewidth and the ratio of (111) to (002) reflected x-ray intensity vs deposition temperature. Substrate vicinal angle is 1.3 deg with respect to the rotation about m-axis.

Figure 10.3 shows (002) Ir linewidths vs. deposition temperature for 500 nm thick films. It also shows the ratio of (111) to (002) intensity, denoted as $I(111)/I(002)$ vs.

deposition temperature. The linewidth minimum occurs at 930 °C, but I(111)/ I(002) is higher than its optimum value of 0.13% for 800 °C film.

To study the effect of film thickness on (002) Ir linewidth and I(111)/I(002), five Ir films were grown at 800 °C, 3nm/min deposition rate and 12 mTorr gas pressure, with thicknesses from 85 to 850 nm. Figure 10.4 shows the variation of linewidth and I(111)/I(002) with film thickness. The (002) Ir linewidth is smaller for thicker films, but I(111)/I(002) shows no systematic variation.

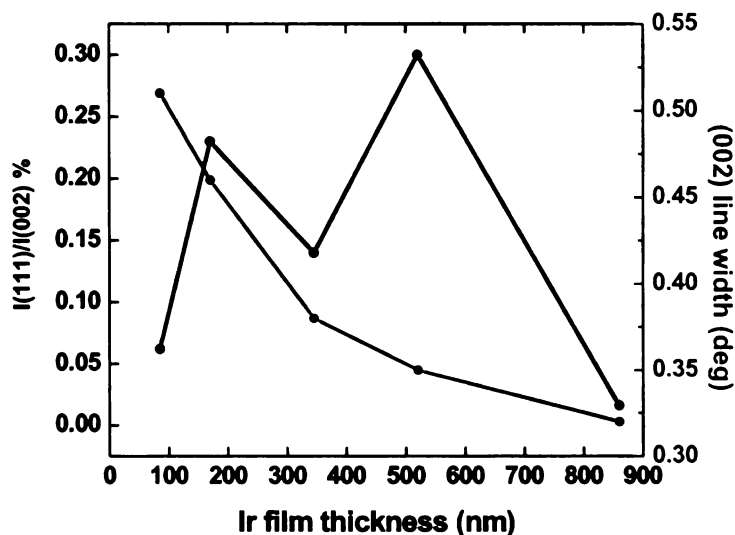


Figure 10.4 Variation of (002) Ir line width and the ratio of (111) to (002) reflected x-ray intensity with Ir film thickness.

Variation of linewidth and I(111)/I(002) was also studied by changing Ar pressure from 5 to 17 mTorr. Four Ir films each 500 nm thick were grown at 800 °C and 3 nm/min deposition rate at different pressures. Figure 10.5 shows the results of this study. The (002) Ir linewidth is a minimum at 12 mTorr, whereas I(111)/I(002) is minimum at 8 mTorr.

The (002) Ir linewidth is much smaller for Ir on SrTiO₃ than for the film grown on Al₂O₃. However comparable linewidth values were found for electron-beam evaporated Ir on both of these substrates in previous studies [11] The reason for this difference is not clear presently and further investigation is required.

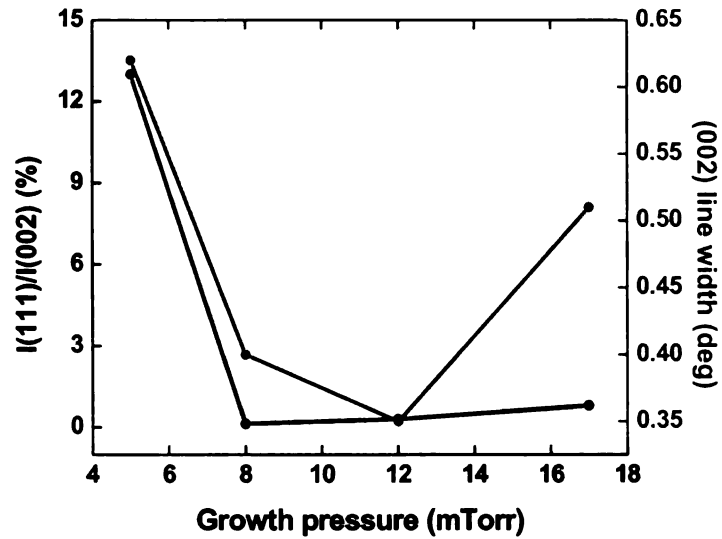


Figure 10.5 Variation of (002) Ir linewidth and the ratio of (111) to (002) reflected x-ray intensities with Ar pressure.

11 References

- [1] W. Adam, E. Berdermann, P. Bergonzo, W. De Boer, and R D collaboration, "The development of diamond tracking detectors for the LHC," *Nuclear instruments and methods in physics research A* **514**, 79-86, 2003.
- [2] W. Adam , B. Bellini, E. Berdermann, P. Bergonzo, and R D collaborations, "status of the R & D activity on diamond particle detectors," *Nuclear instruments and methods in physics research A* **511**, 124-131, 2003.
- [3] J. Isberg, J. Hammersberg, E. Johansson, T. Wikstrom, D. J. Twitchen, A. J. Whitehead, S. E. Coe, and G. A. Scarsbrook, "High carrier mobility in single-crystal plasma-deposited diamond," *Science* **297**, 1670-1672, 2002.
- [4] X. Jiang and C.-P. Klages, "Heteroepitaxial diamond growth on (100) silicon," *Diamond and Related Materials* **2** 1112-1113, 1993.
- [5] C. Wild, P. Koidl, W. Mullersebert, H. Walcher, R. Kohl, N. Herres, R. Locher, R. Samlenski, and R. Brenn, "Chemical-Vapor-Deposition and Characterization of Smooth (100)- Faceted Diamond Films," *Diamond and Related Materials* **2**, 158-168, 1993.
- [6] K. Ohtsuka, K. Suzuki, A. Sawabe, and T. Inuzuka, "Epitaxial growth of diamond on iridium," *Japanese Journal of Applied Physics Part 2* **35**, L1072, 1996.
- [7] K. Ohtsuka, H. Fukuda, K. Suzuki, and A. Sawabe, "Fabrication of epitaxial Diamond Thin Film on iridium (Reprint)," *Japanese Journal of Applied Physics Part 2* **36**, L1214, 1997.
- [8] T. Tsubota, M. Ohta, K. Kusakabe, S. Morooka, M. Watanabe, and H. Maeda, "Heteroepitaxial growth of diamond on an iridium (100) substrate using microwave plasma-assisted chemical vapor deposition," *Diamond and Related Materials* **9**, 1380-1387, 2000.
- [9] F. Hormann, H. Roll, M. Schreck, and B. Stritzker, "Epitaxial Ir layers on SrTiO₃ as substrates for diamond nucleation: deposition of the films and modification in the CVD environment," *Diamond and Related Materials* **9**, 256-261, 2000.
- [10] M. Schreck, F. Hormann, H. Roll, J. K. N. Lindner, and B. Stritzker, "Diamond nucleation on iridium buffer layers and subsequent textured growth: A route for the realization of single-crystal diamond films," *Applied Physics Letters* **78**, 192-194, 2001.
- [11] Z. Dai, C. Bednarski-Meinke, R. Loloee, and B. Golding, "Epitaxial (100) iridium on A-plane sapphire: A system for wafer-scale diamond heteroepitaxy," *Applied Physics Letters* **82**, 3847-3849, 2003.

- [12] C. S. Yan and Y. K. Vohra, "Multiple twinning and nitrogen defect center in chemical vapor deposited homoepitaxial diamond," *Diamond and Related Materials* **8**, 2022-2031, 1999.
- [13] C. S. Yan, Y. K. Vohra, H. Mao, and R. J. Hemley, "Very high growth rate chemical vapor deposition of single crystal diamond," *PNAS* **99**, 12523-12525, 2002.
- [14] A. Tallaire, J. Achard, F. Silva, R. S. Sussmann, and A. Gicquel, "Homoepitaxial deposition of high-quality thick diamond films: effect of growth parameters," *Diamond and Related Materials* **14**, 249-254, 2004.
- [15] G. Bogdan, M. Nesladek, J. D. Haen, V. V. Moshchalkov, K. Haenen, and M. D'Olieslaeger, "Growth and characterization of nearly-atomically flat, thick homoepitaxial CVD diamond films," *Physica Status Solidi* **202**, 2066-2072, 2005.
- [16] M. Behravan, "Electrical conductivity of heteroepitaxial diamond," Ph.D. thesis, *Physics and Astronomy*. East Lansing, MI: Michigan State University, 2005.
- [17] C. Y. Fong and B. M. Klein, "Electronic and vibrational properties of bulk diamond," in *Diamond: Electronic properties and applications*, L. S. Pan and D. R. Kania, Eds. Boston: Kluwer Academic publisher, 1995, 1-29.
- [18] K. Miyoshi, "Structures and mechanical properties of natural and synthetic diamond, report," NASA, Lewis Research Center, Cleveland, Ohio 107249, Chapter 8, 1998.
- [19] T. Teraji, M. Hamada, H. Wada, and M. Yamamoto, "High rate growth and electrical/optical properties of high-quality homoepitaxial (100) diamond films," *Diamond and Related Materials* **14**, 255-260, 2005.
- [20] A. K. Ekimov, V. A. Sidorov, E. D. Bauer, N. N. Melnik, N. J. Curro, J. D. Thomson, and S. M. Stishov, "Superconductivity in diamond," *Nature* **428**, 542-545, 2004.
- [21] I. Sakaguchi, M. N. Gamo, Y. Kikuchi, E. Yasu, H. Haneda, T. Suzuki, and T. Ando, "Sulfur: A donor dopant for n-type diamond semiconductors," *Physical Review B* **60**, R2139-R2141, 1999.
- [22] R. Kalish, A. Reznik, C. Uzan-Saguy, and C. Cytermann, "Is sulfur a donor in diamond?," *Applied Physics Letters* **76**, 757-759, 2000.
- [23] A. Stolz, M. Behravan, M. Regmi, and B. Golding, "Heteroepitaxial diamond detectors for heavy ion beam tracking," *Diamond and Related Materials* **15**, 807-810, 2006.
- [24] J. Wilks and E. Wilks, *Properties and applications of diamond*, 1st edition. Oxford, UK: Butterworth Heinemann, 1991.
- [25] G. Davies, "The A nitrogen aggregate in diamond- its symmetry and possible structure," *Journal of Physics C: Solid State Physics* **9**, L537-L542, 1976.

- [26] A. Mainwood, "Points defects in natural and synthetic diamond: what they can tell us about CVD diamond," *Physica Status Solidi* **172**, 25-35, 1999.
- [27] G. S. Woods, "Platelets and the infrared absorption of type I_a diamond," *Proceedings of the Royal society of London A: Mathematical and Physical Sciences* **407**, 219-238, 1986.
- [28] I. Kiflawi, A. Mainwood, H. Kanda, and D. Fisher, "Nitrogen interstitials in diamond," *Physical Review B* **54**, 16719-16726, 1996.
- [29] A. T. Collins, "The fermi level in diamond," *Journal of Physics: Condensed Matter* **14**, 3743-3750, 2002.
- [30] A. T. Collins, "The Optical and Electronic-Properties of Semiconducting Diamond," *Philosophical Transactions of the Royal Society of London Series a-Mathematical Physical and Engineering Sciences* **342**, 233-244, 1993.
- [31] F. Fuchs, C. Wild, K. Schwarz, and P. Koidl, "Hydrogen-Related IR absorption in chemical vapor deposited diamond," *Diamond and Related Materials* **4**, 652-656, 1995.
- [32] J. Venables, G. Spiller, and M. Hanbuecken, "Nucleation and growth of thin films," *Report in Progress in Physics* **47**, 399, 1984.
- [33] J. A. Venables, "Nucleation calculations in a pair binding model," *Physical Review B* **36**, 4153-4162, 1986.
- [34] J. E. Field, "The properties of natural and synthetic diamond." London: Academic Press, 1992.
- [35] X. Jiang, "Epitaxial diamond thin-films on (001) silicon substrates," *Applied Physics Letters* **62**, 3438-3440, 1993.
- [36] S. Wolter, B. Stoner, J. G. P. Ellis, D. Buhaenko, C. Jenkins, and P. Southworth, "Textured growth of diamond on silicon via in situ carburization and bias-enhanced nucleation," *Applied Physics Letters* **62**, 1215, 1993.
- [37] N. Ishigaki and S. Yugo, "Mechanism of diamond epitaxial growth on silicon," *Diamond and Related Materials* **9**, 1646-1649, 2000.
- [38] X. Jiang, "High quality heteroepitaxial diamond films on silicon: recent progress," *Diamond and Related Materials* **9**, 1640-1645, 2000.
- [39] X. Jiang, K. Schiffmann, C. P. Klages, D. Wittorf, C. L. Jia, K. Urban, and W. Jager, "Coalescence and overgrowth of diamond grains for improved heteroepitaxy on silicon(001)," *Journal of Applied Physics* **83**, 2511-2518, 1998.
- [40] S. Koizumi, T. Murakami, T. Inuzuka, and K. Suzuki, "Epitaxial-growth of diamond thin-films on cubic boron nitride(111) surfaces by DC plasma chemical vapor-deposition," *Applied Physics Letters* **57**, 563-565, 1990.
- [41] S. Koizumi, "Heteroepitaxy of diamond on cubic boron nitride," *Israel Journal of Chemistry* **38**, 33-40, 1998.

- [42] W. Yarbrough and R. Messier, "Current issues and problems in the chemical vapor deposition of diamond," *Science* **247**, 688, 1990.
- [43] H. Kawarada, T. Suesada, and H. Nagasawa, "Heteroepitaxial growth of smooth and continuous diamond thin films on silicon substrates via high-quality silicon-carbide buffer layers," *Applied Physics Letters* **66**, 583-585, 1995.
- [44] H. Kawarada, C. Wild, N. Herres, R. Locher, P. Koidl, and H. Nagasawa, "Heteroepitaxial growth of highly oriented diamond on cubic silicon carbide," *Journal of Applied Physics*. **81**, 3490, 1997.
- [45] T. Tachibana, Y. Yokota, K. Miyata, T. Onishi, K. Kobashi, M. Tarutani, Y. Takai, R. Shimizu, and Y. Shintani, "Diamond films heteroepitaxially grown on platinum (111)," *Physical Review B* **56**, 15967-15981, 1997.
- [46] T. Tachibana, Y. Yokota, K. Kobashi, and M. Yoshimoto, "Heteroepitaxial growth of {111}-oriented diamond films on platinum {111}/sapphire{0001} substrates," *Journal of Crystal Growth* **205**, 163-168, 1999.
- [47] T. Tachibana, Y. Yokota, H. Hayashi, and K. Kobashi, "Growth of {111}-oriented diamond on Pt/Ir/Pt/ substrate deposited on sapphire," *Diamond and Related Materials* **10**, 1633-1636, 2001.
- [48] T. Tachibana, Y. Yokota, K. Kobashi, and Y. Shintani, "X-ray diffraction pole figure measurements of diamond films grown on platinum (111)," *Journal of Applied Physics* **82**, 4327-4330, 1997.
- [49] T. Tachibana, Y. Yokota, K. Nishimura, K. Miyata, K. Kobashi, and Y. Shintani, "Heteroepitaxial diamond growth on platinum(111) by the Shintani process," *Diamond and Related Materials* **5**, 197-199, 1996.
- [50] W. Zhu, P. C. Yang, and G. J. T., "Oriented diamond films grown on nickel substrates," *Applied Physics Letters* **63**, 1640-1642, 1993.
- [51] P. C. Yang, R. Schlessler, C. A. Wolden, W. Liu, R. F. Davis, and Z. Sitar, "Control of diamond heteroepitaxy on nickel by optical reflectance," *Applied Physics Letters* **70**, 2960-2962, 1997.
- [52] Z. Sitar, W. Liu, P. C. Yang, C. A. Wolden, R. Schlessler, and J. T. Prater, "Heteroepitaxial nucleation of diamond on nickel," *Diamond and Related Materials* **7**, 276-282, 1998.
- [53] W. Liu, P. C. Yang, C. A. Wolden, R. F. Davis, J. T. Prater, and Z. Sitar, "Transmission electron microscopy analysis of the oriented diamond growth on nickel substrates," *Journal of Applied Physics* **83**, 7658-7663, 1998.
- [54] T. Bauer, M. Schreck, S. Gsell, F. Hormann, and B. Stritzker, "Epitaxial rhenium buffer layers on Al₂O₃ (0001): a substrate for the deposition of (111)-oriented heteroepitaxial diamond films," *Physica Status Solidi* **199**, 19-26, 2003.
- [55] M. Hansen, *Constitution of Binary Alloys*, Second edition New York, Toronto, London: McGraw-Hill Book Co., 1958.

- [56] M. Schreck, H. Roll, and B. Stritzker, "Diamond/Ir/SrTiO₃: A material combination for improved heteroepitaxial diamond films," *Applied Physics Letters* **74**, 650, 1999.
- [57] T. Fujisaki, M. Tachiki, N. Taniyama, M. Kudo, and H. Kawarada, "Fabrication of heteroepitaxial diamond thin films on Ir(001)/MgO(001) substrates using antenna-edge-type microwave plasma-assisted chemical vapor deposition," *Diamond and Related Materials* **11**, 478-481, 2002.
- [58] C. Bednarski, Z. Dai, A.-P. Li, and B. Golding, "Studies of heteroepitaxial growth of diamond," *Diamond and Related Materials*, **12**, 241-245, 2003.
- [59] K. Ohtsuka, H. Fukuda, K. Suzuki, and A. Sawabe, "Fabrication of epitaxial diamond thin film on iridium," *Japanese Journal of Applied Physics Part 2*, **36**, L1214, 1997.
- [60] K. Suzuki, H. Fukuda, T. Yamada, and A. Sawabe, "Epitaxially grown free-standing diamond platelet," *Diamond and Related Materials*, **10**, 2153-2156, 2001.
- [61] Z. Dai, C. Bednarski, and B. Golding, "Heteroepitaxial diamond film growth: the a-plane sapphire-iridium system," *Diamond and Related Materials* **13**, 552-556, 2004.
- [62] C. H. Lee, J. Qi, L. S. T, and L. S. Hung, "Epitaxial diamond on a Si/CaF₂/Ir substrate," *Diamond and Related Materials* **12**, 1335-1339, 2003.
- [63] T. Bauer, S. Gsell, M. Schreck, J. Goldfub, L. J, D. G. Schlom, and B. Stritzker, "Growth of epitaxial diamond on silicon via iridium/SrTiO₃ buffer layers," *Diamond and Related Materials* **14**, 314-317, 2004.
- [64] S. Gsell, M. Fischer, T. Bauer, M. Schreck, and B. Stritzker, "Yttria-stabilized zirconia films of different composition as buffer layers for the deposition of epitaxial diamond/Ir layers on Si (001)," *Diamond and Related Materials* **15**, 479-485, 2006.
- [65] S. Yugo, T. Kanai, T. Kimura, and T. Muto, "Generation of diamond nuclei by electric field in plasma chemical vapor deposition," *Applied Physics Letters* **58**, 1036, 1991.
- [66] J. Robertson, "Mechanism of bias-enhanced nucleation and heteroepitaxy of diamond on Si," *Diamond and Related Materials* **4**, 549-552, 1995.
- [67] S. Yugo, N. Nobuyuki, and K. Tadamas, "Analysis of heteroepitaxial mechanism of diamond grown by chemical vapor deposition," *Diamond and Related Materials* **7**, 1017-1020, 1998.
- [68] Y. Lifshitz, S. R. Kasi, and J. W. Rabalais, "Subplantation model for film growth from hyperthermal species: Application to diamond," *Physical Review Letters* **62**, 1290-1293, 1989.
- [69] J. Robertson, J. Gerber, S. Sattel, M. Weiler, K. Jung, and H. Ehrhardt, "Mechanism of bias-enhanced nucleation of diamond on Si," *Applied Physics Letters* **66**, 3287-3289, 1995.

- [70] H. P. Kaukonen and R. M. Nieminen, "Molecular-dynamics simulation of the growth of diamond like films by energetic carbon atom beams," *Physical Review Letters* **68**, 620-623, 1992
- [71] S. Kátai, Z. Tass, G. Hars, and P. Deak, "Measurement of ion energy distributions in the bias enhanced nucleation of chemical vapor deposited diamond," *Journal of Applied Physics* **86**, 5549, 1999.
- [72] S. Kátai, A. Kovats, I. Maros, and P. Deak, "Ion energy distributions and their evolution during bias-enhanced nucleation of chemical vapor deposition of diamond," *Diamond and Related Materials* **9**, 317-321, 2000.
- [73] Y. Lifshitz, T. Kohler, T. Frauenheim, I. Guzman, A. Hoffman, R. Q. Zhang, X. T. Zhou, and S. T. Lee, "The mechanism of diamond nucleation from energetic species," *Science* **297**, 1531-1533, 2002.
- [74] B. Sheldon, R. Csencsits, J. Rankin, R. Boekenhauer, and Y. Shigesato, "Bias-enhanced nucleation of diamond during microwave-assisted chemical vapor deposition," *Journal of Applied Physics* **75**, 5001, 1994.
- [75] S. P. McGinnis, M. A. Kelly, S. B. Hagstrom, and R. L. Alvis, "Observation of diamond nanocrystals in carbon films deposited during ion-assisted microwave plasma nucleation pretreatments," *Journal of Applied Physics* **79**, 170-174, 1996.
- [76] S. McGinnis, M. Kelly, and S. Hagstrom, "Evidence of an energetic ion bombardment mechanism for bias enhanced nucleation of diamond," *Applied Physics Letters* **66**, 3117-3119, 1995.
- [77] Y. Shigesato, R. E. Boekenhauer, and B. W. Sheldon, "Emission-spectroscopy during direct-current-biased, microwave- plasma chemical-vapor-deposition of diamond," *Applied Physics Letters* **63**, 314-316, 1993.
- [78] E. Maillard-Schaller, O. M. Kuttel, P. Groning, O. Groning, R. G. Agostino, P. Aebi, L. Schlapbach, P. Wurzinger, and P. Pongratz, "Local heteroepitaxy of diamond on silicon (100): A study of the interface structure," *Physical Review B* **55**, 15895-15904, 1997.
- [79] M. Stammler, R. Stockel, L. Ley, M. Albrecht, and H. P. Strunk, "Diamond nucleation on silicon during bias treatment in chemical vapour deposition as analysed by electron microscopy," *Diamond and Related Materials*, **6**, 747-751, 1997.
- [80] R. Stockel, M. Stammler, K. Janischowsky, L. Ley, M. Albrecht, and H. P. Strunk, "Diamond nucleation under bias conditions," *Journal of Applied Physics* **83**, 531, 1998.
- [81] S. Pecoraro, J. C. Arnault, and J. Werkmann, "BEN-HFCVD diamond nucleation on Si (111) investigated by HRTEM and nanodiffraction.," *Diamond and Related Materials* **14**, 137-143, 2004.

- [82] B. R. Stoner, G. H. M. Ma, S. D. Wolter, and J. T. Glass, "Characterization of bias-enhanced nucleation of diamond on silicon by in-vacuo surface-analysis and transmission electron- microscopy," *Physical Review B* **45**, 11067-11084, 1992.
- [83] X. Jiang, "Effects of ion bombardment on the nucleation and growth of diamond films," *Physical Review B*, **58**, 7064-7075, 1998.
- [84] N. Jiang, B. W. Sun, Z. Zhang, and Z. Lin, "Nucleation and initial growth of diamond film on Si substrate," *Journal of Materials Research* **9**, 2695-2702, 1994.
- [85] B. R. Stoner, G. H. Ma, S. D. Wolter, W. Zhu, Y. C. Wang, R. F. Davis, and J. T. Glass, "Epitaxial nucleation of diamond on beta-SiC via bias-enhanced microwave plasma chemical-vapor-deposition," *Diamond and Related Materials* **2**, 142-146, 1993.
- [86] W. L. Wang, K. J. Liao, J. Wang, L. Fang, P. D. Ding, J. Esteve, M. C. Polo, and G. Sanchez, "Mechanism of diamond nucleation enhancement by electron emission via hot filament chemical vapor deposition," *Diamond and Related Materials* **8**, 123-126, 1999.
- [87] W. L. Wang, G. Sanchez, M. C. Polo, R. Q. Zhang, and J. Esteve, "Nucleation and initial growth of diamond by biased hot filament chemical vapour deposition," *Applied Physics a-Materials Science & Processing* **65**, 241-249, 1997.
- [88] M. Tachiki, T. Fujisaki, N. Taniyama, M. Kudo, and H. Kawarada, "Heteroepitaxial diamond thin film growth on Ir (001)/ MgO(001) substrate by antenna-edge plasma assisted chemical vapor deposition," *Journal of Crystal Growth* **237-239**, 1277-1280, 2002.
- [89] A. Sawabe, H. Fukuda, T. Suzuki, and Y. Ikuhara, "Interface between CVD diamond and iridium films," *Surface Science* **467**, L845-L849, 2000.
- [90] T. Fujisaki, M. Tachiki, N. Taniyama, M. Kudo, and H. Kawarada, "Initial growth of heteroepitaxial diamond on Ir(001)/MgO(001) substrates using antenna-edge-type microwave plasma assisted chemical vapor deposition," *Diamond and Related Materials* **12**, 246-250, 2003.
- [91] S. Kono, T. Takano, T. Goto, Y. Ikejima, M. Shiraishi, T. Abukawa, T. Yamada, and A. Sawabe, "Effect of bias treatment in the CVD diamond growth on Ir(001)," *Diamond and Related Materials* **13**, 2081-2087, 2004.
- [92] S. Kono, M. Shiraishi, N. I. Plusnin, T. Goto, Y. Ikejima, T. Abukawa, M. Shimomura, Z. Dai, C. Bednarski-Meinke, and B. Golding, "X-ray photoelectron study of the initial stages of CVD diamond heteroepitaxy on Ir(001)/SrTiO₃," *New Diamond and Frontiers Carbon Technology* **16**, (363-371), 2005.
- [93] F. Hormann, M. Schreck, and B. Stritzker, "First stages of diamond nucleation on iridium buffer layers," *Diamond and Related Materials* **10**, 1617-1621, 2001.

- [94] H. Hormann, T. Bauer, M. Schreck, S. Gsell, and B. Stritzker, "TEM analysis of nanometer-size surface structures formed by bias enhanced nucleation of diamond on iridium.," *Diamond and Related Materials* **12**, 350-355, 2003.
- [95] M. Schreck, H. Hormann, S. Gsell, T. Bauer, and B. Stritzker, "Transmission electron microscopy study of the diamond nucleation layer on iridium," *Diamond and Related Materials* **15**, 460-464, 2005.
- [96] T. Bauer, S. Gsell, F. Hormann, M. Schreck, and B. Stritzker, "surface modifications and first stages of heteroepitaxial diamond growth on iridium," *Diamond and Related Materials* **13**, 335-341, 2004.
- [97] H. Hormann, H. Y. Peng, T. Bauer, Q. Li, M. Schreck, Y. Lifshitz, S. T. Lee, and B. Stritzker, "Flat epitaxial diamond/ Ir (001) interface visualized by high resolution transmission electron microscopy," *Surface Science* **513**, 525-529, 2002.
- [98] M. Schreck, T. Bauer, G. S., H. Hormann, H. Bielefeldt, and B. Stritzker, "Domain formation in diamond nucleation on iridium," *Diamond and Related Materials* **12**, 262-267, 2003.
- [99] S. Gsell, M. Schreck, G. Benstetter, E. Lodermeier, and B. Stritzker, "Combined AFM-SEM study of the diamond nucleation layer on Ir(001)," *Diamond and Related Materials* **16**, 665-670, 2007.
- [100] K. Hayashi, S. Yamanaka, H. Okushi, and K. Kajimura, "Stepped growth and etching of (001)diamond," *Diamond and Related Materials*, **5**, 1002-1005, 1996.
- [101] K. Hayashi, S. Yamanaka, H. Okushi, and K. Kajimura, "Homoepitaxial diamond films with large terraces," *Applied Physics Letters* **68**, 1220-1222, 1996.
- [102] D. Takeuchi, S. Yamanaka, H. Watanabe, S. Sawada, H. Ichinose, H. Okushi, and K. Kajimura, "High quality homoepitaxial diamond thin film synthesis with high growth rate by a two-step growth method," *Diamond and Related Materials* **8**, 1046-1049, 1999.
- [103] H. Watanabe, D. Takeuchi, S. Yamanaka, H. Okushi, K. Kajimura, and T. Sekiguchi, "Homoepitaxial diamond film with an atomically flat surface over a large area," *Diamond and Related Materials* **8**, 1272-1276, 1999.
- [104] C. L. Wang, M. Irie, and T. Ito, "Growth and characterization of hillock-free high quality homoepitaxial diamond films," *Diamond and Related Materials* **9**, 1650-1654, 2000.
- [105] H. Okushi, "High quality homoepitaxial CVD diamond for electronic devices," *Diamond and Related Materials* **10**, 281-288, 2001.
- [106] H. Okushi, H. Watanabe, S. Ri, S. Yamanaka, and D. Takeuchi, "Device-grade homoepitaxial diamond film growth," *Journal of Crystal Growth* **237-239**, 1269-1276, 2002.

- [107] M. stammler, H. Eisenbei, J. Ristein, J. Neubauer, M. Gobbels, and L. Ley, "Growth of high quality homoepitaxial diamond films by HF-CVD," *Diamond and Related Materials* **11**, 504-508, 2002.
- [108] D. Takeuchi, H. Watanabe, S. Yamanaka, H. Okushi, and K. Kajimura, "Homoepitaxial diamond films grown by step-flow mode in various misorientation angles of diamond substrates," *Diamond and Related Materials* **9**, 231-235, 2000.
- [109] T. Teraji and T. Ito, "Homoepitaxial diamond growth by high power microwave-plasma chemical vapor deposition," *Journal of Crystal Growth* **271**, 409-419, 2004.
- [110] O. A. Williams and R. B. Jackman, "High growth rate MWPECVD of single crystal diamond," *Diamond and Related Materials* **13**, 557-560, 2004.
- [111] O. A. Williams and R. B. Jackman, "Homoepitaxial growth for surface conductive device applications," *Diamond and Related Materials* **13**, 325-328, 2004.
- [112] T. Teraji, "Chemical vapor deposition of homoepitaxial diamond films," *Physica Status Solidi* **203**, 3324-3357, 2006.
- [113] W. J. P. Van Enkevort, G. Janssen, W. Vollenberg, and L. J. Giling, "Anisotropy in monocrystalline CVD diamond growth. Surface morphology of hot filament grown films deposited on planar substrates," *Journal of Crystal Growth* **148**, 365-382, 1994.
- [114] C. Wang, M. Irie, and T. Ito, "Growth and characterization of hillock-free high quality homoepitaxial diamond films," *Diamond and Related Materials* **9**, 1650-1654, 2000.
- [115] T. Bauer, M. Schreck, H. Sternschulte, and B. Stritzker, "High growth rate homoepitaxial diamond deposition on off-axis substrates," *Diamond and Related Materials* **14**, 266-271, 2004.
- [116] N. Lee and A. Badzian, "A study on surface morphologies of (001) homoepitaxial diamond films," *Diamond and Related Materials* **6**, 130-145, 1996.
- [117] N. S. Lee and A. Badzian, "Effect of misorientation angles on the surface morphologies of (001) homoepitaxial diamond thin-films," *Applied Physics Letters* **66**, 2203-2205, 1995.
- [118] N. Lee and A. Badzian, "Effect of methane concentrations on surface morphologies and surface-structures of (001) homoepitaxial diamond thin-films," *Applied Physics Letters* **67**, 2011-2013, 1995.
- [119] K. Hayashi, H. Watanabe, S. Yamanaka, H. Okushi, K. Kajimura, and T. Sekiguchi, "Direct observation of hydrogen-related luminescent states in subsurface region of homoepitaxial diamond films," *Applied Physics Letters* **69**, 1122-1124, 1996.

- [120] K. Hayashi, S. Yamanaka, H. Watanabe, T. Sekiguchi, H. Okushi, and K. Kajimura, "Diamond films epitaxially grown by step-flow mode," *Journal of Crystal Growth* **183**, 338-346, 1998.
- [121] F. K. de Theije, J. J. Schermer, and W. J. P. Van Enckevort, "Effects of nitrogen impurities on the CVD growth of diamond: step bunching in theory and experiment," *Diamond and Related Materials* **9**, 1439-1449, 2000.
- [122] E. Van Veenendaal, F. K. de Theije, J. van Suchtelen, and W. J. P. van Enckevort, "simulation of step patterns on natural diamond (111) surfaces," *Diamond and Related Materials* **11**, 145-152, 2002.
- [123] A. Tallaire, A. T. Collins, D. Charles, J. Achard, R. S. Sussmann, A. Gicquel, M. E. Newton, A. M. Edmonds, and R. J. Cruddace, "Characterization of high-quality thick single-crystal diamond grown by CVD with a low nitrogen addition," *Diamond and Related Materials* **15**, 1700-1707, 2006.
- [124] T. Teraji, M. Hamada, H. Wada, M. Yamamoto, and T. Ito, "High-quality homoepitaxial diamond (100) films grown under high-rate growth condition," *Diamond and Related Materials* **14**, 1747-1752, 2005.
- [125] C. J. Chu, R. H. Hague, J. L. Margrave, and M. P. D'Evelyn, "Growth kinetics of (100) (110) and (111) homoepitaxial diamond films," *Applied Physics letters*, **61**, 1393-1395, 1992.
- [126] J. Achard, A. Tallaire, R. S. Sussmann, F. Silva, and A. Gicquel, "The control of growth parameters in the synthesis of high quality single crystalline diamond by CVD," *Journal of Crystal Growth* **284**, 396-405, 2005.
- [127] G. Bogdan, M. Nesladek, J. D. Haen, K. Haenen, and M. D'Olieslaeger, "Freestanding (100) homoepitaxial CVD diamond," *Diamond and Related Materials* **15**, 508-512, 2006.
- [128] Y. Mokuno, A. Chayahara, Y. Soda, H. Yamada, Y. Horino, and N. Fujimori, "High rate homoepitaxial growth of diamond by microwave plasma CVD with nitrogen addition," *Diamond and Related Materials* **15**, 455-459, 2006.
- [129] A. Tallaire, J. Achard, F. Silva, and A. Gicquel, "Effect of increasing the microwave density in both continuous and pulsed wave mode on the growth of monocrystalline diamond films," *Physica Status Solidi* **202**, 2059-2065, 2005.
- [130] S. Jin and T. D. Moustakas, "Effect of nitrogen on the growth of diamond films," *Applied Physics letters* **65**, 403-405, 1994.
- [131] A. Chayahara, Y. Mokuno, Y. Horino, Y. Takasu, H. Kato, H. Yoshikawa, and N. Fujimori, "The effect of nitrogen addition during high-rate homoepitaxial growth of diamond by microwave plasma CVD," *Diamond and Related Materials* **13**, 1954-1958, 2004.
- [132] R. Locher, C. Wild, N. Herres, D. Behr, and P. Koidl, "Nitrogen stabilized (100) texture in chemical-vapor-deposited diamond films," *Applied Physics Letters* **65**, 34-36, 1994.

- [133] Y. Bar-Yam and T. D. Moustakas, "Defect-induced stabilization of diamonds films," *Nature* **342**, 786-787, 1989.
- [134] S. Ferro, "Synthesis of diamond," *Journals of Materials Chemistry*, **12**, 2843-2855, 2002.
- [135] P. Smereka, X. Li, G. Russo, and D. J. Srolovitz, "Simulation of faceted film growth in three dimensions: microstructure, morphology and texture," *Acta Materialia* **53**, 1191-1204, 2004.
- [136] F. Silva, J. Achard, X. Bonnin, A. Michau, A. Tallaire, O. Brinza, and A. Gicquel, "3D crystal growth model for understanding the role of plasma pre-treatment on CVD diamond crystal shape," *physica status solidi* **203**, 3049-3055, 2006.
- [137] D. B. Murphy, E. D. Salmon, K. R. Spring, M. Abramowitz, and M. W. Davidson, "Differential interference Contrast Microscopy," Olympus microscopy resource center, 2007.
- [138] C. B. Prater, P. G. Maivald, K. J. Kjoller, and M. G. Heaton, "Tapping Mode Imaging: Applications and Technology," Digital Instruments, <http://www.di.com>, Application note AN04.
- [139] S. Flegler, J. Heckman, and K. Klomparens, *Scanning and Transmission Electron Microscopy: An Introduction*. New York: W.H. Freeman and Company, 1993.
- [140] C. R. Bednarski-Meinke, "Nucleation and growth of heteroepitaxial diamond," Ph.D. thesis, *Physics and Astronomy*, East Lansing, MI: Michigan State University, 2002.
- [141] M. P. Marder, *Condensed Matter Physics*. New York: Wiley-interscience Publication 2000.
- [142] D. S. Knight and W. B. White, "Characterization of diamond films by Raman-spectroscopy," *Journal of Materials Research*, **4**, 385-393, 1989.
- [143] S. A. Solin and A. K. Ramdas, "Raman spectrum of diamond," *Physical Review B* **1**, 1687-1698, 1970.
- [144] J. S. Blakemore, *Solid State Physics*, Second edition. New York: Cambridge University Press, 1985.
- [145] H. L. Shriver and N. M. Rosengaard, "Surface energy and work function of elemental metals," *Physical Review B*, **46**, 7157-7168, 1992.
- [146] R. Vargas, T. Goto, W. Zhang, and T. Hirai, "Epitaxial-Growth of iridium and platinum films on sapphire by metalorganic chemical-vapor-deposition," *Applied Physics Letters* **65**, 1094-1096, 1994.
- [147] Y. M. Sun, J. P. Endle, K. Smith, S. Whaley, R. Mahaffy, J. G. Ekerdt, J. M. White, and R. L. Hance, "Iridium film growth with iridium tris-acetylacetonate: oxygen and substrate effects," *Thin Solid Films* **346**, 100-107, 1999.

- [148] M. A. El Khakani, B. Le Drogoff, and M. Chaker, "Effect of the deposition temperature on the properties of iridium thin films grown by means of pulsed laser deposition," *Journal of Materials Research* **14**, 3241-3246, 1999.
- [149] B. Le Drogoff, M. A. El Khakani, P. R. M. Silva, M. Chaker, and G. G. Ross, "Surface properties of pulsed laser deposited Ir, Rh, and Ir (0.9) Rh (0.1) thin films for use as microelectrode arrays in electroanalytical heavy metal trace sensors," *Applied Surface Science* **152**, 77-84, 1999.
- [150] M. A. El Khakani, M. Chaker, and B. Le Drogoff, "Iridium thin films deposited by radio-frequency magnetron sputtering," *Journal of Vacuum Science & Technology a-Vacuum Surfaces and Films* **16**, 885-888, 1998.
- [151] S. Gsell, T. Bauer, J. Goldfuss, M. Schreck, and B. Stritzker, "A route to diamond wafers by epitaxial deposition on silicon via iridium/yttria-stabilized zirconia buffer layers," *Applied Physics Letters* **84**, 4541-4543, 2004.
- [152] G. Koster, B. L. Kropman, G. Rijnders, D. H. A. Blank, and H. Rogalla, "Quasi-ideal strontium titanate crystal surfaces through formation of strontium hydroxide," *Applied Physics Letters* **73**, 2920-2922, 1998.
- [153] M. Kawasaki, A. Ohtomo, T. Arakane, K. Takahashi, M. Yoshimoto, and H. Koinuma, "Atomic control of SrTiO₃ surface for perfect epitaxy of perovskite oxides," *Applied Surface Science* **107**, 102-106, 1996.
- [154] D. L. Medlin, (Private Communication)
- [155] W. Rasband, "Image/J," version 1.28, National Institutes of Health, 2006.
- [156] B. Golding, C. Bednarski-Meinke, and Z. Dai, "Diamond heteroepitaxy: Pattern formation and mechanisms," *Diamond and Related Materials* **13**, 545-551, 2004.
- [157] J. W. Matthews and A. E. Blakeslee, "Defects in epitaxial multilayers, misfit dislocations," *Journal of Crystal Growth* **27**, 118-125, 1974.
- [158] S. Barrat, S. Saada, I. Dieguez, and E. Bauer-Grosse, "Diamond deposition by chemical vapor deposition process: Study of the bias enhanced nucleation step," *Journal of Applied Physics* **84**, 1870, 1998.
- [159] K. K. Irikura and J. L. Beauchamp, "Electronic structure considerations for methane activation by third-row transition-metal ions," *Journal of Physical Chemistry* **95**, 8344-8351, 1991.
- [160] R. Perez-Casero, J. Perriere, A. Gutierrez-Llorente, and D. Defourneau, "Thin films of oxygen-deficient perovskite phases by pulsed-laser ablation of strontium titanate," *Physical Review B* **75**, 165317-1 to 165317-7, 2007.
- [161] N. V. Surovtsev, I. N. Kupriyanov, V. K. Malinovsky, V. A. Gusev, and Y. N. Pal'yanov, "Effect of nitrogen impurities on the Raman linewidth in diamonds," *Journal of Physics: Condensed Matter* **11**, 4767-4774, 1999.

- [162] F. Bogani, S. Miglio, S. Sciortino, A. Taschin, and A. Vinattieri, "Free-exciton photoluminescence as a probe of CVD diamond," *Physica status solidi* **181**, 23-28, 2000.
- [163] R. J. Anderson, (Private communication)
- [164] R. Samlenski, J. Schmalzin, R. Brenn, C. Wild, W. Muller-Sebert, and P. Koidl, "Characterization of homoepitaxial diamond films by nuclear methods," *Diamond and Related Materials* **4**, 503-507, 1995.
- [165] A. R. Lang, M. Moore, A. P. W. Makepeace, W. Wierzchowski, and C. M. Welbourn, "On the dilation of synthetic type Ib diamond by substitutional nitrogen," *Philosophical Transactions: Physical Sciences and Engineering*, **337**, 497-520, 1991.
- [166] C. Tavares, S. Koizumi, and H. Kanda, "Effects of RIE treatments for (111) diamond substrates on the growth of P-doped diamond thin films," *Physica status solidi* **202**, 2129-2133, 2005.
- [167] A. Tallaire, J. Achard, F. Silva, R. S. Sussmann, A. Gicquel, and E. Rzepka, "Oxygen plasma pre-treatments for high quality homoepitaxial CVD diamond deposition," *Physica Status Solidi* **201**, 2419-2424, 2004.
- [168] W. Muller-Sebert, E. Worner, F. Fuchs, C. Wild, and P. Koidl, "Nitrogen induced increase of growth rate in chemical vapor deposition," *Applied Physics Letters* **68**, 759-760, 1995.
- [169] T. Bauer, M. Schreck, J. Hartwig, X. H. Liu, S. P. Wong, and B. Stritzker, "Structural defects in homoepitaxial diamond layers grown on off-axis Ib HPHT substrates," *Physica Status Solidi* **203**, 3056-3062, 2006.
- [170] M. G. Donato, G. Faggio, G. Messina, R. Potenza, S. Santangelo, M. scoccia, C. Tuve, and V. R. G., "Characterisation of homoepitaxial CVD diamond grown at moderate microwave power," *Diamond and Related Materials* **15**, 517-521, 2006.
- [171] P. K. Bachmann and U. W. Detlef, "Optical characterization of diamond," *Diamond and Related Materials* **1**, 422-433, 1992.
- [172] I. Kiflawi, A. E. Mayer, P. M. Spear, J. A. Vanwyk, and G. S. Woods, "Infrared absorption by the single nitrogen defect center in diamond," *Philosophical Magazine B* **69**, 1141-1147, 1994.
- [173] J. Achard, F. Silva, O. Brinza, A. Tallaire, and A. Gicquel, "Coupled effect of nitrogen addition and surface temperature on the morphology and the kinetics of thick CVD diamond single crystals," *Diamond and Related Materials* **16**, 685-689, 2007.

MICHIGAN STATE UNIVERSITY LIBRARIES



3 1293 02956 0145